Space for Shore

ESA EOEP-5

Coastal Erosion

Technical Specification

Document history			
Version	Authors, Organization	Date	Note
1.0	Kerstin Stelzer, Brockmann Consult; Arthur Robinet, Virginie Lafon, Olivier Regniers, Benoit Beguet, Aurélie Dehouck, i-Sea; Paulo Baptista, Sandra Fernández, University of Aveiro; Georgia Kalousi, Terra Spatium; Ionut Serban, Terra Signa; Imanol Echave, Harris; Martin Gade, University of Hamburg; Konstantina Bantouvaki, Issaak Parcharidis, Harokopio University of Athens	12/07/2019	Version 1.0 Technical Specification
1.1	Arthur Robinet, i-Sea Georgia Kalousi, Terra Spatium	13/08/2019	Improvements following ESA feedback New section for Alignment with EUGENIUS platform

Table of content

1 SCOPE OF THE DOCUMENT

This document provides an overview of the algorithms proposed by the Space for Shore consortium to produce the main coastal erosion indicators requested by the interviewed end-users (refer to the Requirement Baseline and User Requirement Document Book), which usually address short-time scale monitoring. Some of these algorithms are also designed to produce the latter indicators over longer timescales with the perspective of demonstrating the potential of ESA Earth Observation data archives and other past/currently-growing freely available archives in the study of coastal erosion in the past 25 years at European scale.

The individual algorithms are provided and described by the partners and form the algorithm candidates for the different indicators. A maturity status of the algorithms is given. The document provides further a mapping of algorithms to end-user requirements. Along with these analyses, proposals of algorithms to be used for the different products and pilot sites are then made. It is expected that the document will be updated with results derived during the POC, in particular the sections describing the accuracy and maturity of the algorithm as well as the discussions on the relevance of the algorithms to the end-user requirements.

2 INTRODUCTION

Based on the end-user requirements, a grouping of coastal erosion indicators and their level of priority were provided in the Requirement Baseline document. Overall, 22 end-users had been interviewed within the public sector including national governmental agencies, regional authorities, intermunicipal cooperation and municipalities, as well as natural site managers, research centers and coastal observatories. From this panel of potential users of Space for Shore services, more than 40 products were requested to support current and future practices to manage issues related to coastal erosion. To help synthetize end-user requirements these products were grouped in 6 product families. This task enabled to fully characterize the end-user needs in terms of product accuracy as well as the update and delivery frequency. It also evidenced that some products were systematically requested by end-users of different regions of interest, while others were mentioned only by one or two end-users. In combination with the availability of validation data, a priority list was provided in the Requirement Baseline document for prototype services to be conducted in the Proof Of Concept (POC) phase (WP1.3). In the end, only 4 product families will be considered, which represents a total of 14 products. Table 2-1 repeats the compilation here for better reading.

The algorithms that are described in this Technical Specification document are organized in six algorithm groups. These groups were built to ease the presentation of the algorithms, as many of these aim at producing similar outputs and/or apply with similar environmental constrains. Each algorithm group is introduced by an introductory and a state-of-the-art section followed by the description of the main features of algorithms (input data, algorithm type / processing chain, output products and tools needed). In addition, information about validation and application range is given for each algorithm. This also includes the information on whether an algorithm is mature enough or shall be tested during POC exercises. All these descriptions are provided in Chapter 3.

In chapter 4 the end-user requirements are mapped against the algorithms and algorithm candidates are defined for every product and every POC site where the product was requested. Even if not requested by end-users, production of some coastal erosion indicators for long-term monitoring at some specific POC sites is envisaged. This will be done for sites where coastal erosion dynamics are large enough with respect to (i) the spatial resolution of the EO data from ESA and other open archives used in the algorithms and (ii) a targeted 25-yr period toward the past.

Chapter 5 introduces the on-line platform EUGENIUS that will be used for Space for Shore product dissemination and provide basic specifications to allow uploading the products on the platform.

Table 2-1. Summary of the main products requested (denoted by yellow colour cells) by interviewed end-users to monitor erosion along European coasts, which covers a wide range of geomorphological and environmental conditions. Extracted and adapted from the Requirement Baseline. Minor corrections were made following new analyses of end-user forms performed during implementation of Chapter 4.

Family name	Product name	Regions of interest								
		FR AQ	FR NOR	FR PACA	GER WS	GER BS	PT NWC	GR EMT	GR PEL	RO
Shoreline	Cliff foot									
	Cliff apex									
	Dune foot									
	Waterline (sea/land interface)									
	Middle of swash zone									
	Maximum swash (or run-up) excursion during major storms									
Coastal morphological patterns	Sandbar location									
	Beach width									
	Tidal creeks: number, length, form, form and number of tidal creek endings									
	Erosion at tidal creek edges									
Coastal DEM	Bathymetry									
Seabed, foreshore and land cover mapping	Underwater seabed type (sandy/rocky/vegetated)									
	Intertidal / foreshore type (sandy/rocky/shingle/…)									
	Coastal habitat and land cover mapping (several levels)									

Table 2-2: Overview of algorithm groups and algorithms, their maturity level and responsible partner. The last column indicates for which indicators the respective algorithm is relevant.

Algorithm Group	Algorithm	Maturity level[1]	Partner	Suitable for: Product Name
DEMs	**Algorithm 1a** DEM generation from optical data	3	i-Sea Terra Spatium	Cliff foot Cliff apex Dune foot Maximum swash (or run-up) excursion during major storms
	Algorithm 1b DEM generation from SAR data	3	Harris	Cliff foot Cliff apex Dune foot Maximum swash (or run-up) excursion during major storms
Water Line and Creek Edge Detection	**Algorithm 2a** Water line detection using band ratios	2	Brockmann Consult	Waterline (sea/land interface) Middle of swash zone Maximum swash (or run-up) excursion during major storms Beach width
	Algorithm 2b Water line detection using NDWI	3	i-Sea	Waterline (sea/land interface) Middle of swash zone Maximum swash (or run-up) excursion during major storms Beach width
	Algorithm 2c Water line detection using a supervised classification process	2	i-Sea	Waterline (sea/land interface) Middle of swash zone Maximum swash (or run-up) excursion during major storms Beach width
	Algorithm 2d Water line detection using binary products from SAR amplitude data	1	Harokopio University	Waterline (sea/land interface) Middle of swash zone Maximum swash (or run-up) excursion during major storms Beach width
	Algorithm 2e Edge detection tidal creeks using SAR	1-2	University of Hamburg	Tidal creeks: number, length, form, form and number of tidal creek endings Erosion at tidal creek edges
Extraction of subaerial morphological structures and changes	**Algorithm 3a** Dune foot extraction using the cross-shore variation of first-order texture metrics from VHR optical data	2	i-Sea	Dune foot Middle of swash zone Maximum swash (or run-up) excursion during major storms
	Algorithm 3b Dune foot extraction based on beach/dune slope from DEM	1	i-Sea	Dune foot
	Algorithm 3c	1	i-Sea	Cliff foot Cliff apex

	Cliff line extraction using the cross-shore variation of the beach/cliff slope from DEM			
	Algorithm 3d Manual linear feature extraction from DEMs (3D digitization)	3	Terra Spatium	Dune foot Cliff foot Cliff apex
	Algorithm 3e Beach width computation	2	i-Sea	Beach width (total, upper, mean)
	Algorithm 3f Top-of-the-cliff vertical movement monitoring using PSI	2	Harokopio University of Athens	Cliff movement[2]
	Algorithm 3g Intertidal creek morphological characteristics	1	Brockmann Consult	Tidal creeks: number, length, form, form and number of tidal creek endings Erosion at tidal creek edges
	Algorithm 3h Dune foot extraction using supervised classification	2	i-Sea	Dune foot
	Algorithm 3i Cliff line extraction using supervised classification	1	i-Sea	Cliff foot Cliff apex
Bathymetry	**Algorithm 4a** Empirical model to retrieve bathymetry from HR/VHR optical data	3	i-Sea	Bathymetry
	Algorithm 4b Quasi-analytical model to retrieve bathymetry from HR/VHR optical data	3	i-Sea	Bathymetry Underwater seabed type (sandy/rocky/vegetated)
	Algorithm 4c Bathymetry swell inversion	1-2	University of Aveiro	Bathymetry
Classification methods	**Algorithm 5a** Supervised classification approaches based on optical data	3	i-Sea	Underwater seabed type (sandy/rocky/vegetated) Waterline (sea/land interface) Maximum swash (or run-up) excursion during major storms Coastal and intertidal habitat and land cover mapping
	Algorithm 5b Classification based on texture information derived from SAR amplitude data	3	Harris	Coastal and intertidal habitat and land cover mapping
	Algorithm 5c Decision tree classification based on band ratios and LSU	3	Brockmann Consult	Tidal creeks: number, length, form, form and number of tidal creek endings Erosion at tidal creek edges

				Underwater seabed type (sandy/rocky/vegetated) Coastal and intertidal habitat and land cover mapping
Extraction of submerged morphological structures and changes	**Algorithm 6a** Submerged sand banks	3	Terra Signa	Sandbar location
	Algorithm 6b Mapping change of sandbars	2	Brockmann Consult	Sandbar location

[1] Maturity levels:

1 = innovative or experimental algorithm (not tested yet, want to test ideas in POC sties)

2 = Demonstration algorithm: tested on selected test sites in selected images

3 = mature algorithm – well tested, applied and published algorithm

[2] Cliff movement: This indicator has not originally been retained for POC activities since it has been mentioned only once (by a coastal observatory in SW France, OCA). However, many end-users may not be aware that existing SAR-based algorithms allow obtaining very accurate information about vertical deformation of the ground and could then bring crucial information about cliff dynamics and for early warning of landslides. Thus, with the support of Harokopio University of Athens, a product indicating vertical movement on the top of the cliff will be finally envisaged.

3 DETAILED ALGORITHM DESCRIPTION

3.1 Algorithm group 1: Generation of DEMs

3.1.1 Introduction

Digital Elevation Models (DEMs) are used as input for several coastal erosion products, either directly by exploiting the provided 3D information or indirectly though the production of other DEM-derived datasets, i.e. calculation of volumes and 3D lines extraction.

In particular, many different techniques have been developed the past decades for DEM generation, starting from conventional ground topographic surveys (e.g. GNSS techniques), to robust photogrammetric methods and sophisticated computer vision techniques (e.g. structure-from-motion, etc.); that exploit data acquired from several different instruments and sensors. This chapter is focusing on the description of present state-of-the-art DEM generation algorithms applied on satellite, optical and SAR, high (HR) and very high-resolution (VHR) imagery.

3.1.2 State-of-the-art

Optical Imagery

In the case of optical satellite data -both for HR and VHR-, the existing state-of-the-art algorithms are covering the hereunder processing steps:

1. Image Pre-processing: In order to improve the radiometric quality and optimize the images for subsequent processing steps, a series of filters are usually applied on the datasets. The most common pre-processing processes encompass noise reduction, contrast and edge enhancement. Noise reduction filters aim at reducing noise, while sharpening edges and preserving corners and one pixel-wide lines (Baltsavias et al., 2001).
2. Image Orientation: In order to achieve the image orientation, a bundle adjustment with the supplied Rational Polynomial Coefficients (RPCs) model is usually deployed. RPCs provide a compact representation of a ground-to-image geometry, allowing photogrammetric processing without requiring a physical camera model. A set of

images (with stereo or tri-stereo overlapping) is given to determine the set of polynomial coefficients in the RPCs model to minimise the error. Therefore, RPCs model is a generalized sensor model, which can achieve high approximation accuracy, while Least Square Method (LSM) is usually used to determine the optimal parameter solution of the rational function model. Indeed, the use of Ground Control Points (GCPs) during this computation is providing the best possible accuracy which according to literature review could be sub-pixel (Eisenbeiss et al., 2004).

3. DEM Generation Method: Several different matching algorithms are used for DEM generation, starting from the early ones like correlation-based methods (i.e. 2D correlation, 3D correlation) to most advanced ones', like i.e. 3D Least Square Matching, Global and Semi-Global Matching, to more sophisticated computer vision-based algorithms, like Feature Based Matching, Structure-from-motion. In most methods the pyramid image matching scheme is used. In general, a pyramid image matching method stores matching results in low resolution matching and uses these results as initial points for higher resolution matching.

As stated previously, it is both possible to use pairs of satellite images (i) acquired simultaneously along the satellite path ("mono-date" the satellite looking first frontward and then backward) or (ii) at several consecutive dates ("multi-date"). The later has been recently tested on Norman coastal cliffs using a dataset of Pleiades satellite images (Letortu et al., submitted). Several aspects of viewing geometry (incidence angle) in relation with coastal geomorphology (e.g. height and slope of coastal cliffs, shoreline orientation) have to be considered preliminarily. For instance, DEM generation using mono-date stereo images over very high and abrupt coastal cliffs (like in Normandy) appeared not to be appropriate, i.e. when the satellite is looking backward, only the top and plateau of the cliff being imaged, not the cliff face nor the cliff foot. In addition, sun position at the time of image acquisition associated with shoreline orientation may also be considered, due to shadow effects that may occur on cliff face and cliff foot. The same effect can be seen in sand beach areas (Almeida et al. 2019), where a DEM generated from a Pleiades stereo product can achieve very high vertical accuracy (under 0.5m) but this accuracy decreases in dune faces where shadows are produced.

SAR Imagery Algorithms

To generate DEM data from a couple of SAR images two choices are available: (i) interferometry and (ii) radargrammetry. Stereoscopy for SAR data is known as radargrammetry. This technique is similar to optical/photogrammetry, but it uses a couple of SAR amplitude images to match homologous points and produce height (Capaldo et al., 2014). Radargrammetry produces DEMs with a vertical accuracy of a few meters (worse than interferometry) but is very robust to atmospherical conditions.

Interferometry is a technique that benefits from SAR phase information. In a pair of SAR images, the same object generates a signal with a change in phase that is related to a shift in the distance viewer-object. With the appropriate processing this change can be mapped to a height (Small et al., 1996). This technique has been already used in coastal areas (Hong et al., 2006) (Choi et al., 2007), achieving a vertical accuracy close to 1 meter. Anyway, it is a very sensitive technique that could be affected by different factors as atmosphere conditions, loss of coherence (due to changes on surface conditions).
Interferometry is a technique that cannot be used always. Phase information is very sensitive to changes, and variations in a surface can completely destroy phase coherence making DEM extraction impossible. This is the case in vegetation areas, where coherence falls due to continuous "growing" of the observed object. In these cases, a combination of interferometry and radargrammetry can be used. This approach has been already tested on coastal areas (Yu, 2011) (Nikolakopoulos et al., 2015).

Simultaneous data acquisition using a pair of satellites flying closely in formation is the challenge unravelled by DLR with the twin SAR interferometry TerraSAR-X / TanDEM-X mission. The mission provides digital elevation data at 12-m full resolution and with an absolute vertical accuracy of 1 m. Airbus DS and CSTARS has recently launched the commercial "WorldDEM Ocean Shoreline" product based on TanDEM-X which is supposed to provide an up-to-date reference for coastal issues at global scale (applications in glaciology, see Milillo et al., 2019).

3.1.3 Algorithm 1a – DEM generation from optical data

3.1.3.1 Algorithm description

- *Input data*

According to the software used different sets of optical satellite images can be used for DEM production, including:

- VHR (or HR) optical imagery acquired in stereo or tri-stereo mod, e.g. Pleiades (or SPOT5)
- pair of non-georeferenced VHR (or HR) optical images acquired at subsequent dates with a temporal spacing relatively small with respect to the characteristic temporal scales of the coastal change studied.

Ground Control Points.

- *Algorithms*

We propose two algorithms for DEM extraction from optical data.

1. The first one is the algorithm proposed by Li and Gruen *(Li Z., Gruen A., 2004)*. This algorithm performs these steps:
   - Image pre-processing: edge-preserving filtering and Wallis filtering are applied to images in order to reduce radiometric artefacts (very dark and bright areas) and enhance texture patterns in regular areas.
   - A pyramid of images is generated reducing image scale at each level, then starting from lowest resolution we apply these steps at each level in a cascade:
     - Feature point matching: feature points generated using Foerstner interest operator and matching done by a geometrically constrained cross-correlation method *(Gruen, Zhang, 2003)*. Edge-matching: edges generated by the Canny operator are matched using a shape matching method.
     - Grid point matching: a regular grid of points is matched using a global image matching method with a relaxation technique *(Gruen, Zhang, 2003)*.
   - A final refined matching based on the modified MPGC *(Gruen, 1985)* is performed in order to achieve accuracy in the subpixel range.
2. The second algorithm, performs the following steps:
   - Image Orientation: A bundle adjustment with RPCs model and with the use of GCPs during this computation is be performed.
   - DEM generation method: It is based in the use of two families of matching methods:
     - Feature Based Matching (FMB): FBM is a matching strategy that is very robust. It only needs coarse approximations and is very fast. It has an accuracy of about 1/3 of a pixel. The matching process computes interest values in two images of a matching pair that describe the appearances of features. The matching process determines common features in the pair by means of the computed interest values.
     - Least Squares Matching (LSM): LSM is a matching strategy that is very accurate, but better approximations are required, and it is considered rather slow in comparison to FBM. It is mostly used to refine points obtained from FBM. The accuracy is about 1/10 pixel. The matching process uses a mask created from one image and a template from the second image at a previously matched point. The mask is shifted on the template until the sum of squares of the gradients is minimized.

- *Tools*

ENVI + OPTICALscape (implementing first algorithm)

ArcGIS-ESRI, QGIS, DTMaster stereo, INPHO Photogrammetric Suite by Trimble (implementing second algorithm)

- *Output product*
  - Raster file output: "*.geotiff"

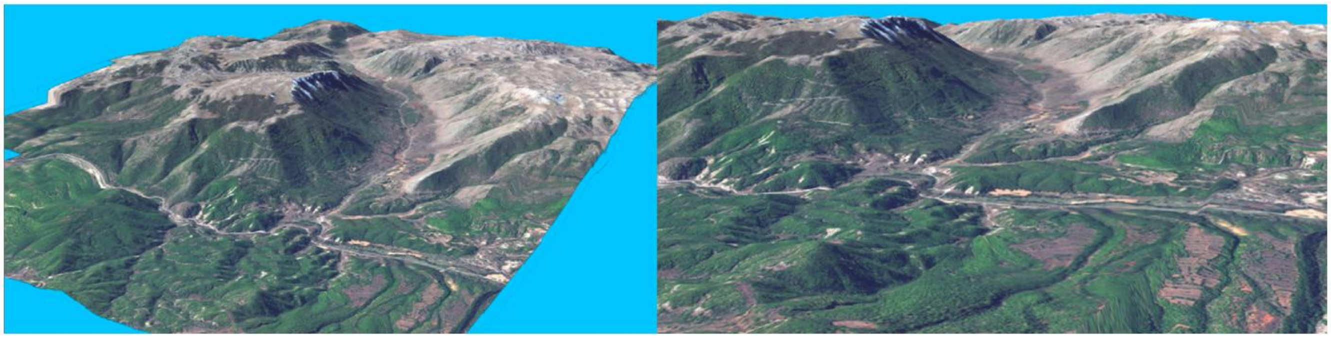

Figure 3-1 - DEM produced from Very High-Resolution optical stereo satellite imagery (Pleiades, Terra Spatium, ©2016)

- Vector file output: Point cloud file “*.las”

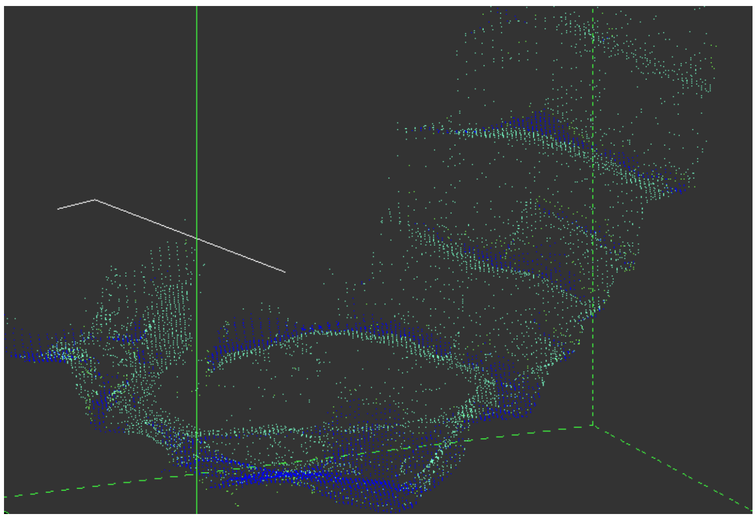

Figure 3-2 – DEM - Point cloud produced from Very High-Resolution optical stereo satellite imagery over cliff area (Pleiades, Terra Spatium, ©2016).

3.1.3.2 Validation

The deployed algorithms have several times been validated during commercial and research projects executed by Terra Spatium, for areas all over Greece. The algorithms have been tested both in coastal, as well as in-land and mountainous areas, covering all types of morphologies. In these projects, VHR optical satellite data were used to produce DEMs, in particular stereo Pleiades and Geoeye-1 imagery, while computations were performed with the use of Ground Control Points (GCPs). GCPs were collected during *in situ* GPS survey (Real Time Kinematic, L1/L2 frequencies) with a mean horizontal accuracy 2-3 cm. On the same time a set of independent points were collected the so-called Check Points (CPs) and used for validation of the produced DEMs. Usually a set of CPs, evenly distributed along the AOI were chosen, trying to cover the specificities of each region, for every stereo-pair at least 7-8 CPs were collected. At the end of the day, a relative horizontal accuracy of 1 meter and a relative vertical accuracy of 2-3 meters, was achieved in most cases.

In the framework of Space for Shore, a validation campaign will be carried out to assess DEMs production in Greece based on *in situ* GPS measurements. This field work will take place in late-September 2019, mid-October and could be combined along with the validation activities for 4.2.6.2 (Algorithm 2d – Water Line Detection using binary products from SAR amplitude data).

Reference projects:

1. BEACHTOUR National R&D project: A synergy for the sustainable development and safety of the Hellenic Tourist Beaches for the identification of 'best practices' in science-driven beach monitoring, management and decision-making. (2013-2016).
2. ACRITAS National R&D project, Space Technologies for Surveillance and Monitoring of Integrated Applications: research, design, develop and validate integrated space-based surveillance and monitoring applications through advanced multi-sensor data fusion technologies. (2013-2016)
3. Commercial project (National Cadastre & Mapping Agency) Production of VHR ortho-photomaps and DEM along the coastline of Greece. (2007-2009)

3.1.3.3 Application range and Maturity

The maturity of the deployed algorithms is considered high, while in order to achieve a high accuracy, Ground Control Points (GCPs) are needed for the computation of the aerial triangulation. The GCPs could be acquired, either directly, through *in situ* GPS measurements (L1/L2) or indirectly, extracted from pre-existing orthophoto maps of a similar accuracy. Of course, when direct GCPs measurements are being used a better accuracy is achieved at the end of the day, i.e. with measurements deriving from a robust computation with GPS equipment using L1/L2 frequencies. In cases that VHR satellite optical imagery (e.g. Pleiades) is used along with GCPs (measured on the ground) the relative vertical accuracy achieved is around 2-3 meters.

3.1.4 Algorithm 1b – DEM generation from SAR data

3.1.4.1 Algorithm description

In order to perform calculations between two SAR images, a previous co-registration must be done to have both images in the same geometry *(Meijering, Unser, 2004)*. Shift between images is first estimated using sensor position and orientation metadata, then a cross-correlation approach is used for fine-shifting. The complete schema can be found in the figure below.

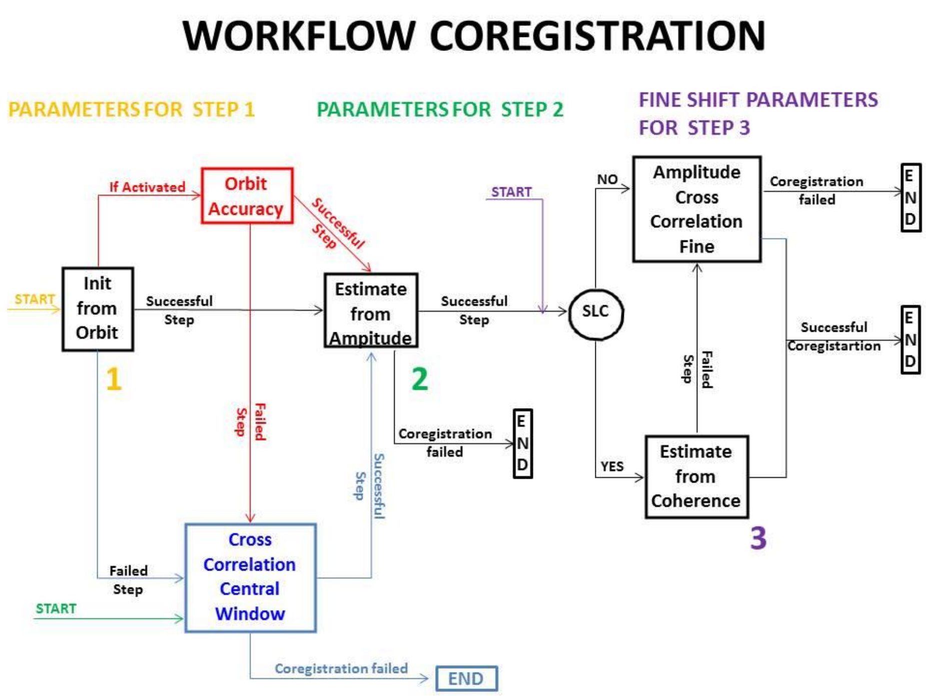

Figure 3-3: Workflow for the co-registration of a pair of SAR images for DEM pre-processing

Once The coregistered SLC (Single-Look Complex) data are used to compute an interferogram, which is obtained by multiplying the first complex image by the conjugate of the second one. The interferogram provides an image of phase changes that are due to different effects *(Monti Guarnieri, Guccione, Pasquali, Desnos, 2003)*.

Interferogram is “flattened” to remove the constant phase effect produced by acquisition geometry and the topographic phase effect produced by terrain slope. In order to flatten the interferogram, a low-resolution DEM (as SRTM) is used to estimate terrain slope.

Once flattened, an adaptive filtering is applied to reduce noise and coherence image is generated *(Baran, Stewart, Kampes, Perski, Lilly, 2003)*. Coherence is a parameter that measures correlation between master and slave acquisitions. Only areas with a high coherence value can be used in DEM computation.

At that point the phase information, which is cyclical, should be unwrapped to provide a linear change. This unwrapping is done using a minimum cost flow method *(Reigber, Moreira, 1997)*.

Before converting phase change to height, a reflattening step is performed using ground control points to remove phase offset and phase ramp. Once removed phase change is converted to height (Göblirsch, Pasquali, 1996).

- *Input data*
    - Pair of SAR SLC data captured on interferometric conditions using VHR (e.g. TerraSAR-X) or HR (Sentinel-1)
- *Algorithms*
    - Master SLC and Slave SLC coregistration
    - Interferogram generation
    - Filtering and coherence estimation
    - Phase unwrapping
    - Reflattening
    - Phase to height calculation
- *Tools*
    - SARscape
- *Output product*
    - DEM in raster (TIFF) format

3.1.4.2 Validation

The described algorithm has been implemented in SARscape software for several years, and it has been used in different commercial projects successfully. Multiple references about algorithm validity and accuracy can be found (Singh et al., 2005; Yamane et al., 2008; Deo et al., 2014; Pandit et al., 2014). From this last one, we extracted a plot to show the accuracy obtained by the algorithm in a mountainous area (Indian Himalayas) using TanDEM-X data, with an RMSE of 8.2 meters (Figure 3-4).

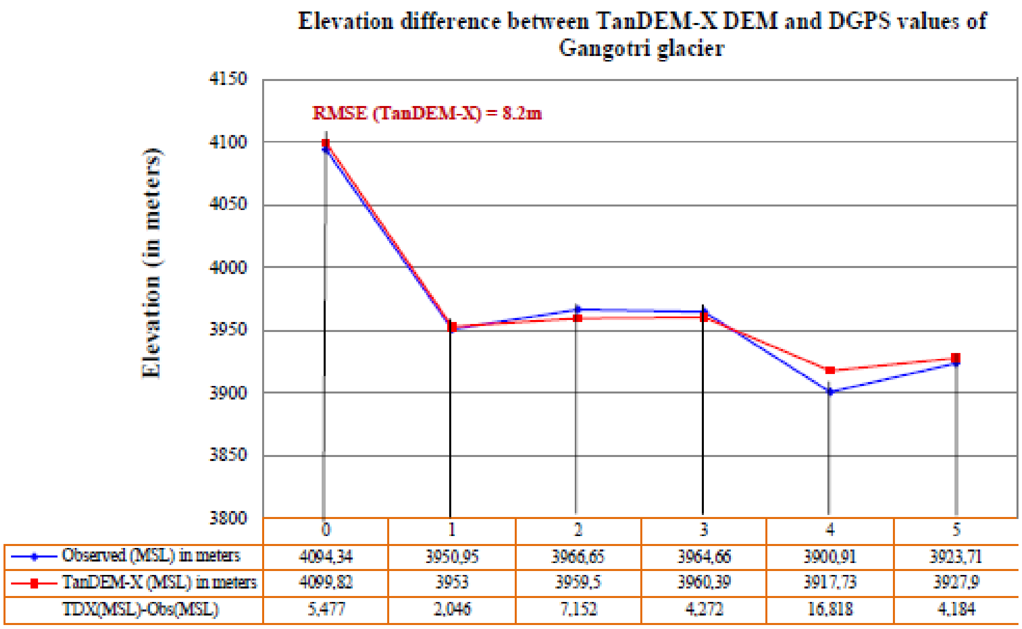

Figure 3-4: elevation values obtained through DGPS and TanDEM-X DEM for Gangori glacier (0 to 5 – Ground observation points)

3.1.4.3 Application range and Maturity

The algorithm is mature, as it has been used and tested for years. In general, it can be used to generate DEM in any kind of terrain, but high slope areas use to produce shadows and layover effects that reduce coherence and prevent interferometry. In these areas radargrammetry can be used to complete DEM.

3.1.5 References

A. Monti Guarnieri, C. Cafforio, P. Guccione, D. Nüesch, D. Small, E. Meier, P. Pasquali, M. Zink, Y. L. Desnos: "Multi-mode ENVISAT ASAR Interferometry: Techniques and Preliminary Results". Proceedings of EUSAR Conference 2002.

Aji Rahmayudi, Aldino Rizaldy, COMPARISON OF SEMI AUTOMATIC DTM FROM IMAGE MATCHING WITH DTM FROM LIDAR, The International Archives of the Photogrammetry, Remote Sensing and Spatial Information Sciences, Volume XLI-B3, 2016 XXIII ISPRS Congress, 12–19 July 2016, Prague, Czech Republic.

Almeida L.P., Almar R., Bergsma E., Berthier E. Baptista P., Garel E., Dada O., Alves B, 2019. Deriving High Spatial-Resolution Coastal Topography From Sub-meter Satellite Stereo Imagery, Remote Sensing, 11(5), 590, doi:10.3390/rs11050590.

Baran I., Stewart Mike P., Kampes Bert M., Perski Z., Lilly P.: "A Modification to the Goldstein Radar Interferogram Filter", IEEE Transactions on Geoscience and Remote Sensing, Vol. 41, No. 9, September 2003.

Baltsavias, E., Pateraki, M., Zhang, L., 2001. Radiometric and Geometric Evaluation of IKONOS Geo Images and their use for 3D building modelling. Proc. Joint ISPRS Workshop "High Resolution Mapping from Space 2001", Hannover, Germany, 19-21 September.

Capaldo P., Fratarcangeli F., Nascetti A., Pieralice F., Porfiri M., Crespi M., 2014 "Land applications of radar remote sensing. Chapter6. High resolution radargrammetry – 3D terrain modeling"

Choi J., Lee C., Won J., 2007 "DEM Generation over Coastal Area using ALOS PALSAR Data - Focus on Coherence and Height Ambiguity". Korean journal of remote sensing, Vol. 23, No. 6, pp.559-566

Costantini, M.: "A novel phase unwrapping method based on network programming". Geoscience and Remote Sensing, IEEE Transactions on, May 1998, 36(3), pp. 813 - 821.

Eisenbeiss, H & Baltsavias, E & Pateraki, Maria & Zhang, L. (2004). Potential of IKONOS and QuickBird imagery for accurate 3D point positioning, orthoimage and DSM generation. International Archives of the Photogrammetry, Remote Sensing and Spatial Information Sciences. 35.

D. Small, P. Pasquali, and S. Fuglistaler: "A Comparison of Phase to Height Conversion Methods for SAR Interferometry". Proceedings of IGARSS 1996 – Lincoln, Nebraska – USA – 27-31 May 1996.

Deo R., Rao "Vertical Accuracy Assessment of TanDEM-X DEM over Indian Test Areas" EUSAR 2014; 10th European Conference on Synthetic Aperture Radar

Fraser, C.S. and H.B. Hanley, 2002. Bias compensation in rational functions for Ikonos satellite imagery. *Photogrammetric Engineering & Remote Sensing,* 11.

Ghulam A., Amer R., Ripperdan R.: "A filtering approach to improve deformation accuracy using large baseline, low coherence DInSAR phase images", Paper presented at IGARSS 2010.

Göblirsch W. and Pasquali P.: "Algorithms for calculation of digital surface models from the unwrapped interferometric phase". Proceedings of IGARSS 1996, pp. 656–658.

Grodecki, Jacek and Gene Dial, 2003. Block Adjustment of High-Resolution Satellite Images Described by Rational Polynomials. *Photogrammetric Engineering & Remote Sensing*, 69(1): 59-68.

Gruen, A., 1985, Adaptive Least Squares Correlation: A powerful Image Matching Technique. South Africa Journal of Photogrammetry, Remote Sensing and Cartography, 14 (3), pp. 175-187.

Gruen, A., Zhang L., 2003. Automatic DTM Generation from TLS data. Optical 3-D Measurement Techniques VI, Vol. I, Zurich, pp. 93-105.

Gruen, A., Zhang L., 2004. Automatic DSM generation from linear array imagery data. Int. *Archives of the Photogrammetry, Remote Sensing and Spatial Information Sciences*, Istanbul, Turkey, Vol XXXV, Part B3, pp. 128-133.

Hanley, H.B., Yamakawa, T. and C.S. Fraser, 2002. Sensor Orientation for High-Resolution Satellite Imagery. *International Archives of Photogrammetry & Remote Sensing*, 34(1): 69-75.

Hong S., Won J., 2006 "ERS-ENVISAT cross-interferometry for coastal DEM construction"

InSAR Principles: Guidelines for SAR Interferometry Processing and Interpretation (ESA TM-19).

Lemaire, C. (2008). Aspects of the DSM production with high resolution images. International Archives of the Photogrammetry, Remote Sensing and Spatial Information Sciences, Vol.XXXVII, Part B4, pp.1143-1146.

Letortu P., Jaud M., Théry C., Nabucet J., Passot S., Augereau E. (2019). The potential of Pleiades images with high angle of incidence for reconstructing the Norman coastal cliff face, International Journal of Applied Earth Observations and Geoinformation, submitted.

Li, Z. and Gruen, A., 2004. Automatic DSM generation from linear array imagery data. Int. *Archives of the Photogrammetry, Remote Sensing and Spatial Information Sciences*, Istanbul, Turkey, Vol XXXV, Part B3, pp. 128-133.

Meijering E. and M. Unser, A Note on Cubic Convolution Interpolation, IEEE Transactions on Image Processing, Vol. 12, No. 4, April 2004.

Milillo P., Rignot E., Rizzoli P., Scheulch, Mouginot J., Bueso-Bello J., Prats-Iraolla (2019). Heterogeneous Retrear and ice melt of Thwaites Glacier, West Antarctica. Science Advances, 5(1), DOI: 10.1126/sciadv.aau3433

Monti Guarnieri A., P. Guccione, P. Pasquali, and Y.L. Desnos: "Multi-mode ENVISAT ASAR interferometry: Techniques and preliminary results, IEEE Proceedings on Radar, Sonar and Navigation, Vol. 150, No. 3, June, 2003

Nikolakopoulos K., Kyriou A., Charalampopoulo V., 2015 "DSM generation from Sentinel and COSMO-SkyMed data using interferometry and radargrammetry: A case study from Mykonos, Greece", Proceedings of SPIE - The International Society for Optical Engineering 9535, DOI: 10.1117/12.2193977

Pandit A., Ramsankaran R., Rao Y.S. "Generation and Validation of the Interferometric SAR DEMs from TanDEM-X data for Gangotri and Hamtah Glaciers of Indian Himalayas" Procedia Technology Volume 16, 2014, Pages 793-805

Reigber A. and J. Moreira: "Phase Unwrapping by Fusion of Local and Global Methods". Proceedings of IGARSS'97 Symposium, 1997.

Reinartz, Peter & D ' Angelo, Pablo & Krauß, Thomas & Chaabouni-Chouayakh, Houda. (2010). DSM Generation and Filtering from High Resolution Optical Stereo Satellite Data, Remote Sensing for Science, Education, Natural and Cultural Heritage, EARSeL, 2010.

Richard M. Goldstein, Charles L. Werner: "Radar Interferogram Filtering for Geophysical Applications". Geophys. Res. Lett., 25(21), 4035–4038.

Santel, F & Linder, W & Heipke, C. (2004). Stereoscopic 3D-image sequence analysis of sea surfaces. In ISPRS Commission V Symposium, Vol. 35, pp. 708–712.

Singh L., Westen C.J., Champati Ray P.K., Pasquali P. "Accuracy assessment of InSAR derived input maps for landslide susceptibility analysis: a case study from the Swiss Alps" Landslides (2005) 2: 221. https://doi.org/10.1007/s10346-005-0059-z

Taejung Kim, Sooahm Rhee, International Archives of the Photogrammetry, Remote Sensing and Spatial Information Sciences, Volume XXXVIII-4/W19, 2011 ISPRS Hannover 2011 Workshop, 14-17 June 2011, Hannover, Germany

Yamane N., Fujita K., Nonaka T., Shibayama T., Takagishi S. "Accuracy evaluation of DEMderived by TerraSAR-X data in the Himalayan region" The International Archives of the Photogrammetry, Remote Sensing and Spatial Information Sciences. Vol. XXXVII. Part B7. Beijing 2008

Yu J.H., 2011 "Interferometric Synthetic Aperture Radar and Radargrammetry for Accurate Digital Elevation Model Generation in New South Wales, Australia" Thesis at the University of New Wales".

3.2 Algorithms group 2: Water line and creek edge detection

3.2.1 Introduction

Water lines are a key indicator for almost all coastal types. It is relevant for beaches as well as for the morphological assessment of intertidal flat dynamics. Therefore, we present here a number of different approaches and may select different ones for the different coastal types. The water line indicator is easily retrievable from both optical and SAR data, since the water surfaces exhibit radiometric signatures typical and different from other components of the coastal environment.

Although simple to extract, the water line is dependent on the tidal stage and swell conditions. Therefore, to infer relevant shoreline positions from the water line, it is necessary to define a cautious strategy for image acquisition. It is recommended to use high-tide or low-tide images only during calm weather conditions. Composite images based on time-series can also be used to minimize the impact of waves and tide. Indeed, in microtidal regions, the impact of tide level has a fairly low incidence on the water line location. If the water line is extracted from Sentinel-2 imagery the impact is probably marginal. However, it should be considered when using very high-resolution data.

These strategies must be considered whatever the extraction methods detailed hereafter.

Indeed, the waterline is a good proxy to identify the middle of the swash zone. In the Requirement Baseline, the middle of the swash zone is only required in microtidal regions, where this indicator is expected to be efficiently retrieved from an image time-series or from image composites as described below (algorithm 2b).

3.2.2 State-of-the-art

There are several techniques for delineating shorelines for change assessment, however, most studies use photogrammetry/satellite data and spatial analysis techniques (Evadzi et al., 2017; Appeaning Addo, Walkden, and Mills, 2008; Jayson-Quashigah, Appeaning Addo, and Kufogbe, 2013; Vos et al., 2019). Other techniques and data types utilized for quantifying beach erosion/shoreline changes includes storm-induced beach change model (Wise, Smith, and Larson, 1996), Bruun Rule (Bruun, 1962), Hallermeier equation (Hallermeier, 1981), shoreline evolution model (Patterson, 2009; Robinet et al., 2018), and shoreline response model (Huxley, 2009). Although these alternative methodologies to satellite/photogrammetry also make use of observations, apart from the reliability of each of the method itself, the suitability of the method also depends on the availability, spatial extent, and timescale of data.

Except for photogrammetry, which records historical coastal changes, the other methods are based on a combination of models and data, which are more useful when trying to estimate hazard extent where there is limited historical information.

Although shoreline/coastline definition over the years been debated because of the dynamic nature of coasts (Alves, 2007; Bird, 1985; Boak and Turner, 2005), the shoreline definition referred to as the ‘‘wet–dry’’ line, also referred to as the high water line, along the coast has been the most widely used definition for shoreline mapping because it can be identified both on images and physically in the field (Crowell, Leatherman, and Buckley, 1991; Dellepiane, De Laurentiis, and Giordano, 2004).

Several remote sensing researchers have worked on the topic of coastline extraction, firstly using SAR amplitude (Lee, 1990; Descombes et al., 1996; Niedermeier et al., 2000; Baghdadi et al., 2004) and then exploring capabilities of InSAR coherence analysis techniques (e.g. Schwabisch et al., 2006; Dellepiane et al. 2004; Wendleder et al. , 2013). Albeit of the theoretically large backscattering difference in between land (bright) and water (dark), they collectively found noise effects (the water surface being frequently wind-affected, and effect of shallow waters) to be quite disturbing for automatic waterline extraction, thus exploring several approaches and filtering techniques to improve their differentiation. Another option to improve the discrimination water-land would be the use of polarimetric SAR (Wu et al. 2018). SAR images with HH polarization seem to be the most appropriate to discriminate coastline. Full polarized data can also be used to perform a polarimetric decomposition that will provide information about the degree of volume scattering, surface scattering and double bounce found on the terrain allowing a land-water classification (Gurreonero Robinson et al., 2013). Other discrimination measures derived from full polarimetric data have been proposed, as correlation between cross-polarization and co-polarization images, to improve separability land-water (Nunziata et al., 2016). The recently published paper by Schmitt et al (2019) addresses the SAR state-of-the-art. Recently, the authors experimented an original TanDEM-X InSAR mono-static data mode “in pursuit” (both satellites flying with a larger spatial baseline and temporal baseline of 10 s) for land-water segmentation with the objective of obtaining denoised information and a better discrimination of both amplitude and coherence images. One dedicated case for water line detection is the application in intertidal flats to identify the dry-fallen flat surfaces and separate them from tidal creeks. Investigations in intertidal flat areas are based on both – optical and SAR data. Differentiation between water areas and dry-fallen intertidal flats is done by band ratios and linear spectral unmixing for the German Wadden Sea (Brockmann & Stelzer, 2006). The application of SAR data for the same question has been conducted by Gade & Melchiona and also the combination of both techniques, e.g. by Jung & Ehlers 2014, van der Val 2005.

3.2.3 Algorithm 2a – Water line detection using band ratios

3.2.3.1 Algorithm description

Evadzi et al. 2017, Appeaning Addo, Walkden, and Mills, 2008 and several coastal researchers argue that not only does band combination of satellite images provides the best atmospheric penetration and helps visualize Coastlines and shores but also by the application of band ratios helps to delineate shorelines along with the Wet-Dry line definition. Evadzi et al., 2017 extracted historical shorelines for change assessment in Ghana, by performing Landsat data resolution standardization, histogram threshold and automatic shoreline extraction using ENVI classic software to separate the land and water based on band ratios (b2/b5 for Landsat 5 data).

The proposed algorithm is focused on band ratio and histogram threshold. This is applied to Sentinel-2 and Landsat-8 data; the later used for validation of the algorithm. The Sentinel-2 data is resampled to 10m whereas the Landsat-8 data is resampled to 15 m after conversion of the data’s at-sensor radiance to at-sensor reflectance values.

Shorelines generated from Landsat data will not be at the exact location compared to those generated from sentinel-2 products mainly because of spatial resolution differences. However, the shorelines generated from both sources (based on the same expression) must represent the exact wet-dry lines that can be observed on the respective images as well as on the field.

Because of this capability, long term change detection can be computed using several data sources if the uncertainties such as positional/tidal changes accuracy, digitization uncertainty (e.g. if derived from orthophotos), as well as image resolution uncertainties, can be measured and applied as weights to the shorelines before the computation of change rates (Evadzi et al., 2017).

- *Input data*

Sentinel-2 and Landsat-8 products were used for the delineation of the shoreline based on the water-line definition and band ratio approach explained above.

- *Algorithms*
  - Conversion of Landsat-8 product’s at-sensor radiance values to at-sensor reflectance values.

- Resample Sentinel-2 product to 10m and Landsat-8 to 15 m.
- Compute the Wet-Dry Line from Sentinel-2 using the bands math (b8/b2), and the corresponding bands (band5/band2) to compute the shoreline for the Landsat-8 product.
- Threshold for shoreline (1 >= Wet-Dry Line >= 0.9). This threshold is identified to be a good threshold for delineation of the shoreline as it does not only delineate the wet-dry line (Figure 3-5) but also minimizes the selection of mixed pixels that do not reflect the wet-dry shoreline (Figure 3-6; '0.5 <= shoreline (more mixed pixels) <= 0.9').
- Preform Arithmetic Mean 3x3' to smoothing the shoreline.
- Polygonization of the mask to generate vector data.

* *Tools*

SN SNAP, QGIS, ArcGIS, DSAS

* *Output product*

Figure 3-6 shows shoreline extracted from sentinel-2 images after the water-line definition and band ratio approach explained above.

Figure 3-5 - Automatic shoreline delineation from Sentinel-2 Image (data ref. date: 08-04-2019).

Figure 3-6 - The impact of thresholds on shoreline delineation from Sentinel-2 Image (data ref. date: 25-04-2019).

3.2.3.2 Validation

The application of the algorithm (with the same threshold) works well for the generation of the wet-dry shoreline on both Sentinel-2 and Landsat-8 products. This is also expected to work for other satellite products that have similar corresponding bands. Figure 3-7 shows the delineated shoreline from Landsat-8 plotted on Sentinel-2 RGB image and shoreline for the same period. Although the Landsat-8 shoreline aligns with the Sentinel-2 shoreline at some places, there are slight shifts at some areas. This is expected mainly as a result of product resolution differences. If different products are to be used for historical rate of change computation, it is therefore important that the uncertainties must be accounted for and applied as weights to the respective shorelines.

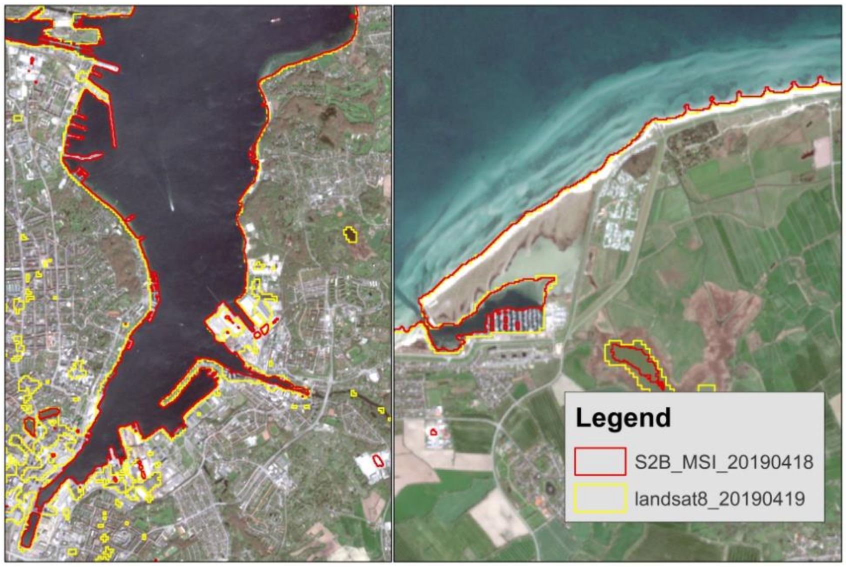

Figure 3-7 - Different shorelines extracted from 2 sentinel and Landsat8 products (18/19-04-2019).

3.2.3.3 Application range and Maturity

Coastal areas are very dynamic and are affected by climatic, geological, changes in the supply of sand to the coast, and anthropogenic factors. Extreme events to seasonal changes including cloud and foreign objects over the shoreline can significantly influence the delineated shoreline. Figure 3-8 shows the likely impact of the aforementioned factors on the shoreline delineation at the shores of Kiel. Several publications reported a similar challenge for the delineation of the wet-dry line for deltaic regions because of how dynamic these regions are. Care must be taken when selecting a shoreline to generalize for a month.

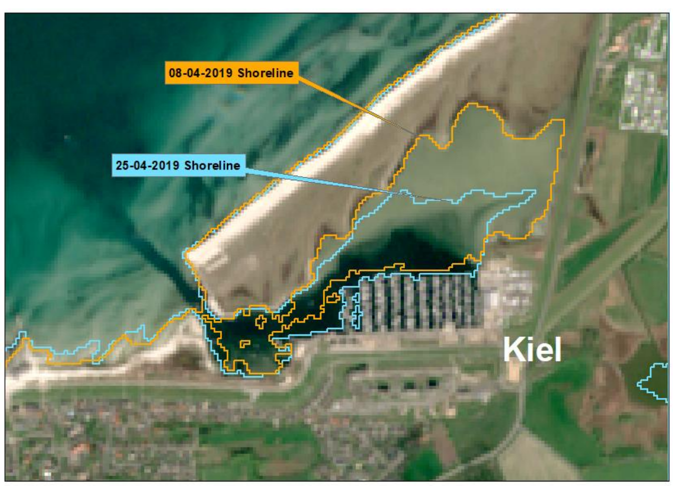

Figure 3-8 - Different shorelines extracted from 2 sentinel images for 04-2019.

3.2.4 Algorithm 2b – Water line detection using NDWI

The NDWI is the indicator chosen to localize the shoreline on a worldwide scale. The method is described by Luijendijk et al. (2018), it has been implemented, tested and validated by DeltaRes researchers in order to describe the state of the world's beaches, in particular to estimate shoreline change rates for the 33-year period 1984–2016.

3.2.4.1 Algorithm description

- *Input data*

The approach has been tested and validated for Landsat-8 and Sentinel-2 data.

- *Algorithms*

For dynamic shoreline detections, the authors recommend building yearly composites images generated by the 15% reflectance percentiles per pixel (Hansen et al., 2013). Optimal averaging period is of 192 days. Analysis of the composite images significantly decreases the influence of the tidal stage on the detected shoreline positions and averages out seasonal variability in wave and beach characteristics. However, it does not remove the effect of tide and wave, so change analysis has to be performed cautiously or, at least, on long term trend.

The resulting composite images are used to estimate the Normalized Difference Water Index (NDWI)

The Canny edge detection filter (Canny, 1986) is used to roughly estimate the position of the water-land transition on the NDWI image. Then, the Otsu thresholding method (Otso, 1979) is used on a buffer polygon around the water-land transition to identify the most probable threshold to classify water and land on the image.

The detected water lines at the edge of the water mask are smoothed using a 1D Gaussian smoothing operation to obtain a gradual shoreline avoiding the pixel-induced staircase effect. A value of three gives the best results based on the four validation cases; meaning that it takes three cells on both sides during the 1D smoothing.

This latter approach can be used to improve the vectors extracted from classified images, DEM etc … .

- *Tools*

The tools will be implemented by consortium members.

Image processing tools used are either implemented on most image processing software. Alternatively, they can also be found in OpenSource libraries.

- *Output product*

Results carried out for shoreline extraction and shoreline change with time is shown in Figure 3-9.

Vectors in shape format (or kml/kmz) are delivered.

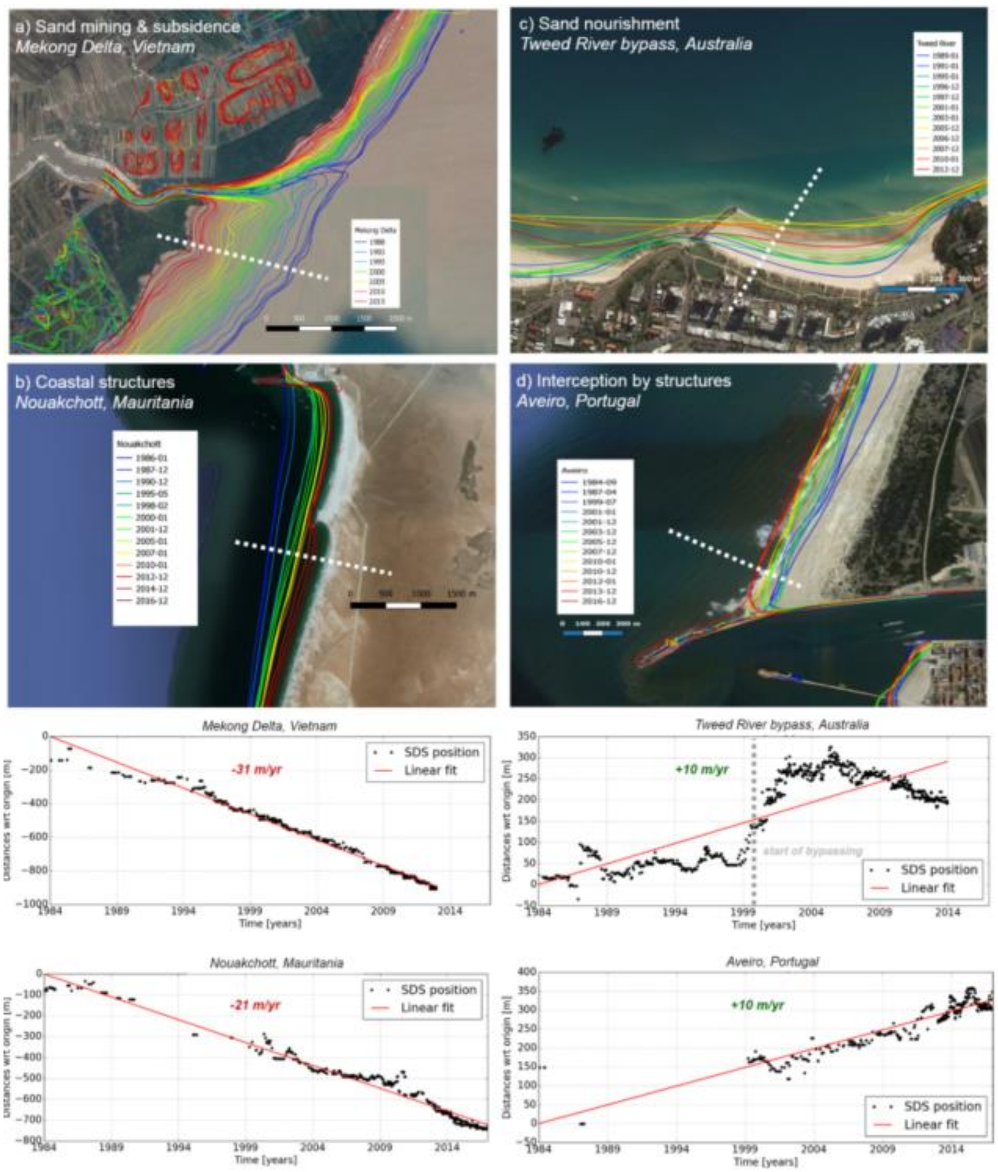

Figure 3-9 - Examples of the satellite derived shorelines for four selected cases of beach erosion and accretion due to human interventions (from Luijendijk et al., 2018)

3.2.4.2 Validation

Soundful validation conducted along 63 km of coastline and spanning over 13 years of Landsat images is given by (Luijendijk et al., 2018). The mean offset for all transects between observations and SDS is 2.0 m with a RMSE of 17 m.

3.2.4.3 Application range and Maturity

This approach with regards to water line extraction and borders between classes is considered as mature, as it has been applied on a worldwide basis. It applied to all sandy shorelines, whatever tidal range and wave exposure.

3.2.5 Algorithm 2c – Water line detection using a supervised classification process

3.2.5.1 Algorithm description

- *Input data*

The algorithm needs an HR or VHR optical image as input data. Application of atmospheric correction to the image in a pre-processing step is recommended but not mandatory.

- *Algorithms*

The detection of the waterline is made using an algorithm based on supervised classification (all details are provided in Section 4.5.3) that differentiates water pixels from others located in the subaerial domain. The implementation of the classification process chain is relatively simple and requires only a single HR or VHR optical image. First, polygons representative for the two typologies addressed must be digitalized to build the reference database. Then, the RandomForest classifier is applied to the spectral bands of the image but also on band ratios (e.g. NDWI) to enhance the water/land discrimination. This step is followed by a spatial regularization of the class contour to remove some noise and isolated pixels. The final step consists in extracting the interface between the two typologies from the raster-formatted classification output.

- *Tools*

The algorithm uses python programming languages with support of Orfeo ToolBox and GDAL libraries.

2. *Output product*

The output from this algorithm is a vector of waterline positions.

3.2.5.2 Validation

No soundful validation with ground-truth data has been performed yet. The detection accuracy is expected to be of the order of the pixel resolution of the input image.

3.2.5.3 Application range and maturity

Any environmental conditions affecting the spectral signature at pixels along the waterline such as clouds, shadows and breaking waves may lead to significant spatial error in the waterline location. The algorithm can be applied for any water level (tide + storm surge + wave setup) and any types of geomorphology. However, larger errors in the waterline detection may occur for gently sloping foreshore (intertidal areas) experiencing large tidal range, as the buffer area between the water and the subaerial domains may exceed the image pixel resolution. It must be reminded that intercomparison between subsequent image-derived waterlines is often tricky as the actual water level at the date/time of image acquisitions may have varied. Although not fully automated, the maturity of this algorithm is high.

3.2.6 Algorithm 2d – Water line detection using binary products from SAR amplitude data

3.2.6.1 Algorithm description

SAR data are known to extract water detection regardless of weather conditions because they transmit microwaves (Pradhan et al, 2018). Land and especially man-made objects have a strong back-scattering. In addition, due to the instability of the water surface, SAR images have low amplitude and low coherence. Finding the perfect threshold will result a map which shows waterline detection. Using both geometries we can extract stronger results.

- *Input data*
  - Pairs of SAR GRD Sentinel 1A & 1B scenes or from ERS1/2 SAR or ENVISAT ASAR acquisitions.
- *Algorithms*
  - Subset
  - Apply orbit file
  - Calibration
  - Speckle filtering tool

- Math band
- Geometric Correction: Range Doppler terrain correction
- *Tools*
  - Snap by ESA
  - ArcGIS
- *Output product*
  - Map of waterline detection

3.2.6.2 Validation

This algorithm will be validated with field work in collaboration with a coastal erosion expert from Harokopio University of Athens as well as with civil protection authorities. Focusing on coastal erosion, field work will take place in order to validate the results obtained by SAR data processing. In addition, the team will be equipped with GNSS instruments. We will use high resolution optical data to validate the results obtained by SAR data. This field work will take place in late-September, mid-October. The horizontal accuracy is expected to be in the order of the resolution of the input image.

3.2.6.3 Application range and Maturity

Using SAR data, we will be able to use indices for land/water detection, and thus monitor coastal changes due to erosion. The data that will be used are independent from weather and atmospheric contribution. The indices that will be chosen are widely used, thanks to the rich archive from SAR applications on coastline detection. Only minor is the spatial resolution, which is not very high, but validation data will help us evaluate our results.

3.2.7 Algorithm 2e – Edge detection tidal creeks using SAR

3.2.7.1 Algorithm description

This algorithm is based on dual-co-polarization TerraSAR-X imagery. It uses the 'Polarization Coefficient', or Normalized Difference Polarization Ratio, that highlights differences in the radar backscattering from exposed intertidal flats and open water bodies at both radar co-polarizations. Primarily, this algorithm was developed to generate indicators for bivalve beds on intertidal flats, and it turned out that the results can also be used to infer the borders between tidal creeks (or channels) and open water. After the Polarization Coefficient was calculated on a pixel-by-pixel basis, basic statistical operators are applied in a moving window (of typical size 11 pixels by 11 pixels, while the exact dimension depends on the spatial resolution of the SAR data). Typical results for a test site on the German North Sea coast are shown in Figure 3-10. This algorithm will be improved and further developed to enable for a high-resolution detection of the rims of tidal creeks.

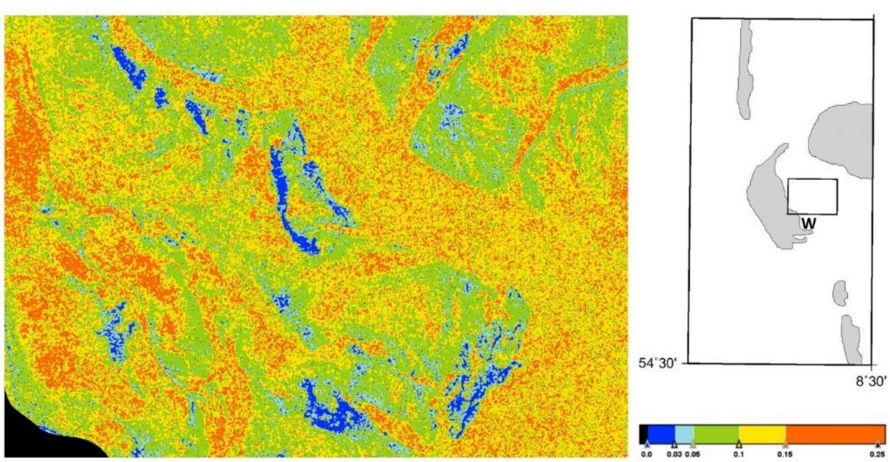

Figure 3-10 - Spatial statistics of the Polarization Coefficient derived from TerraSAR-X SAR data of exposed intertidal flats behind Amrum island on the German North Sea coast acquired in 2013. Green colours indicated exposed flats, yellow and *orange colours indicate tidal creeks and channels and flat areas covered by remnant water. Blue colours indicate bivalve beds. From Gade & Melchionna (2016).*

Higher precision of the results obtained will be gained through a combination of multi-acquisition SAR imagery. Areas of high spatial morphodynamics will be identified through the application of new operators on multiple maps of Polarization Coefficient statistics.

This algorithm will also be tested with images from ENVISAT SAR acquired at both co-polarizations, pending the availability of such data at targeted POC sites.

- *Input data*

Dual-co-polarization SAR imagery

- *Algorithms*

The algorithm's basic steps include:

3. Georeferencing
4. Calibration
5. Calculation of the Polarization Coefficient
6. Spatial statistical operations
7. Threshold optimization for the indication of tidal creeks

- *Tools*

The algorithm uses ESA's SNAP Toolbox. Basic algebraic operations can be included using Python.

3.2.7.2 Validation

The validation of the results will be based on either data from aerial surveillance and *in situ* campaigns, or a combination of both. A validation will be performed during the POC and also the applicability for coastal erosion will be conducted. The accuracy is expected in the order of the resolution of the input image.

3.2.7.3 Application range and Maturity

The algorithm can be applied to SAR imagery of any exposed intertidal flats, independent of their location. Its application to SAR data of cliffs and sand beaches needs to be examined. Maturity is Level 1.

3.2.8 References

Appeaning Addo, K.; Walkden, M., and Mills, J.P., 2008. Detection, measurement and prediction of shoreline recession in Accra, Ghana. ISPRS Journal of Photogrammetry and Remote Sensing, 63(5), 543–558. doi:10.1016/j.isprsjprs.2008.04.001

Alves, M.V.M., 2007. Detection of Physical Shoreline Indicators in an Object-Based Classification Approach: Study Case: Island of Schiermonnkoog. Enschede, The Netherlands: The International Institute for Geo-Information Science and Earth Observation, Master's thesis, 53p.

Baghdadi N., Gratiot N., Lefebvre J.P., Oliveros C., Bourguignon A. "Coastline and mudbank monitoring in French Guiana: contributions of radar and optical satellite imagery" Can. J. Remote sensing, Vol. 30, No. 2, pp. 109-122, 2004

Baselice F., Ferraioli G. (2013) Unsupervised coastal line extraction from SAR Images, IEEE Geoscience and Remote Sensing Letters, 10, 1350-1354

Bird, E.C.F., 1985. Coastline Changes: A Global Review. Chichester, U.K.: Wiley, 219p.

Boak, E.H. and Turner, I.L., 2005. Shoreline definition and detection: A review. Journal of Coastal Research, 21(4), 688–703. doi:10.2112/ 03-0071.1

Bruun, P., 1962. Sea-level rise as a cause of shore erosion. Journal of the Waterways and Harbors Division, 88(1), 117–132.

Canny, J., 1986. A computational approach to edge detection", IEEE Transactions on Pattern Analysis and Machine Intelligence, vol 8, pages 679–714.

Crowell, M.; Leatherman, S.P., and Buckley, M.K., 1991. Historical shoreline change: Error analysis and mapping accuracy. Journal of Coastal Research, 7(3), 839–852.

Dellepiane, S.; de Laurentiis, R., and Giordano, F., 2004. Coastline extraction from SAR images and a method for the evaluation of the coastline precision. Pattern Recognition Letters, 25(13), 1461–1470. doi:10.1016/j.patrec.2004.05.022

Descombes et al., 1996 Descombes X., Moctezuma M, Maitre H., Rudant JP (1996) Coastline detection by a markovian segmentation on SAR images, Signal Processing, 55, 123-132

Evadzi, P.I., Zorita, E. and Hünicke, B., 2017. Quantifying and predicting the contribution of sea-level rise to shoreline change in Ghana: information for coastal adaptation strategies. Journal of Coastal Research, 33(6), pp.1283-1291.

Gade, M., and Melchionna, S., 2016: Jint Use of Multiple Synthetic Aperture Radar Imagery for the Detection of Bivalve Beds and Morphological Changes on Intertidal Flats, Estuar. Coast. Shelf Sci., 171, 1-10, doi:10.1016/j.ecss.2016.01.025.

Gurreonero Robinson, D. A., Bijker, W., Tolpekin, V. A., 2013. Shoreline Detection Using TerraSAR-X Quad Polarization Mode. The International Hydrographic Review, 10.

Hagenaars, G., de Vries, S., Luijendijk, A., de Boer, W., Reniers, A., 2018. On the accuracy of automated shoreline detection derived from satellite imagery: A case study of the sand motor mega-scale nourishment, Coastal Engineering, 133, pp. 113-125, doi:10.1016/j.coastaleng.2017.12.011.

Hallermeier, R.J., 1981. A profile zonation for seasonal sand beaches from wave climate. Coastal Engineering, 4, 253–277.

Hansen, M. C. et al. High-Resolution Global Maps of 21st-Century Forest Cover Change. Science 342, 850–853 (2013) Huxley, C., 2009. Shoreline Response Modelling Assessing the Impacts of Climate Change. http://www.coastalconference.com/ 2009/papers2009/Chris%20Huxley%20Full%20paper.pdf

Jayson-Quashigah, P.-N.; Appeaning Addo, K., and Kufogbe, S.K., 2013. Medium-resolution satellite imagery as a tool for monitoring shoreline change. Case study of the eastern coast of Ghana. In: Conley, D.; Masselink, G.; Russell, P., and O'Hare, T. (eds.), Proceedings from the International Coastal Symposium (ICS) 2013 (Plymouth, United Kingdom). Journal of Coastal Research, Special Issue No. 65, pp. 511–516. doi:10.2112/SI65-087.1

Lee J.S., (1990) Coastline detection and tracing in SAR images, IEEE Transactions on Geoscience and Remote Sensing, 28, 662-668.

Luijendijk, A., Hagenaars, G., Ranasinghe, R., Baart, F., Donchyts, G and Aarninkhof, S. 2018. The State of the World's Beaches. SCIENTIFIC REPORTS | (2018) 8:6641| DOI:10.1038/s41598-018-24630-6.

Mentaschi, L., Vousdoukas, M.I., Pekel, J.F., Voukouvalas, E., Feyen, L., 2018. Global long-term observations of coastal erosion and accretion, Scientific Report, 8(12876), doi: 10.1038/s41598-018-30904-w.

Niedermeier et al., 2000, Niedermeier A., Romaneessen E., Lehner S. (2000) Detection of coastlines in SAR images using wavelet methods, IEEE Transactions on Geoscience and Remote Sensing, 38, 605-616

Nunziata F., Buono A., Migliaccio M., Benassai G. "Dual-Polarimetric C- and X-Band SAR Data for Coastline Extraction" IEEE Journal of Selected Topics in Applied Earth Observations and Remote Sensing · May 2016

Otsu, N. A Treshold Selection Method from Gray-Level Histograms. IEEE Transactions on Systems, Man, and Cybernetics Vol. SMC-9, No. 1, https://doi.org/10.1109/TSMC.1979.4310076 (1979).

Patterson, D., 2009. Modelling the Shoreline Impacts of Richmond River Training Walls. http://www.coastalconference.com/2009/ papers2009/Dean%20Patterson%20Full%20paper.pdf.

Pekel, J.F., Cottam, A., Gorelick, N., Belward, A.S., 2016. High-resolution mapping of global surface water and its long-term changes, Nature, 540(418), doi: 10.1038/nature20584.

Pradhan B., Rizeei H.M. & Abdulle A., (2018), Quantitative Assessment for Detection and Monitoring of Coastline Dynamics with Temporal RADARSAT Images. Remote Sens. 2018, 10, 1705.

Robinet, A., Idier, D., Castelle, B., Marieu, V., 2018. A reduced-complexity shoreline change model combining longshore and cross-shore processes: The LX-Shore model. Environmental Modelling & Software, 109, 1-16, doi:10.1016/j.envsoft.2018.08.010.

Schmitt M., Baier G., Zhu X.X. (2019) Potential of nonlocally filtered pursuit monostatic TanDEM-X data for coastline detection, ISPRS Journal of Photogrammetry and Remote Sensing, 8.

Schwabisch M., Lehner S., Winkel N., (2006) Coastline extraction using ERS SAR interferometry, in Proceeding of 3rd ERS Symposium, 1049-1053.

van der Wal, D., P.M.J. Herman, A. Wielemaker-van den Dool (2005), Characterisation of surface roughness and sediment texture of intertidal flats using ERS SAR imagery. Remote Sens. Environ. 98 (1): 96-109.

Vos, K., Harley, M.D., Splinter, K.D., Simmons, J.A., Turner, I.L., 2019. Sub-annual to multi-decadal shoreline variability from publicly available satellite imagery. Coastal Engineering, 150, 160-174, doi:10.1016/j.coastaleng.2019.04.004.

Wendleder A., Wessel A., Roth A., Breunig M., Martin K., Wagenbrener . (2013) TanDEM- water indication mask : generation and first evaluation results, IEEE Journal of Selected Topics in Applied Earth Observations and Remote Sensing, 6, 171-179

Wise, R.A.; Smith, S.J., and Larson, M., 1996. SBEACH: Numerical Model for Simulating Storm-Induced Beach Change. Report 4. Cross-Shore Transport under Random Waves and Model Validation with SUPERTANK and Field Data. Vicksburg, Mississippi: U.S. Army Engineer Waterways Experiment Station, Technical Report CECR-89-9, 140p.

Wu L., Tajima Y., Yamanaka Y., Shimozono T., Sato S. "Study on characteristics of SAR imagery around the coast for shoreline detection" Coastal Engineering Journal Volume 61, 2019 - Issue 2

3.3 Algorithms group 3: Extraction of subaerial morphological structures and changes

3.3.1 Introduction

This section presents algorithms that are used to compute key indicators useful to assess the morphodynamics of different subaerial areas along the sandy and rocky coasts and to mitigate risks related to erosion processes. Attractive coastal areas are usually well urbanized with the building of expensive seafront, facilities and houses on top of coastal dunes and cliffs. Monitoring the dunes foot and the main cliff lines (foot and apex) is crucial for coastal stakeholders to anticipate the impact of erosion that can damage seriously these infrastructures and threaten the safety of coastal users. The knowledge of the beach width is also essential for coastal municipalities as it provides an indication on the recreational potential and attractiveness of their coastlines. This indicator is therefore often included in beach nourishment strategy. Although less widespread in end-user practices, the tracking of unusual and sudden low-amplitude vertical movements on top of cliff can also indicate a ground instability and warn of a likely and future landslide usually associated with dramatic impacts if not anticipated. The study of ground vertical movements on longer timescales (> annual timescale) can also reveal the existence of trends of gradual downward settling of the ground surface, called subsidence. Within deltaic environments this ground process, which can reach several centimetres per year in some places, leads to a continuous coastline retreat and higher exposure to marine flooding.

3.3.2 State-of-the-art

Linear features (dunes foot, cliff lines) extraction in coastal areas can be made following different approach. The simpler strategy relies on manually digitizing polylines (Hapke and Reid, 2007) from raw images, processed image where features are enhanced, DEMs or even combination of DEMs and images. The main advantages of this method are that: (i) it can be performed using only basic tools from GIS software; and (ii) the operator digitizing the linear features can identify possible source of error and take a decision based on ground-truth knowledge that is sometimes nearly impossible to automate; (iii) the outputs of the digitizing procedure are directly polylines and no post-processing is required before delivery to end-users. However, this approach includes some limitation. First, the operator requires an accurate knowledge of the study site to avoid subjective decision in digitizing (e.g. when the dune foot line starts be blurred due to accretion processes that sometimes occur). Second, this approach is really time consuming. While manually digitizing lines for few images is rather acceptable with production times expected to be of some hours to days, applying this procedure to a high number of dates and sites becomes totally inefficient.

To overcome these limitations, scientists and companies tend to develop automated tools (e.g. Hoeke et al., 2001; Brzank et al., 2005; Zarillo et al., 2008; Liu et al., 2009; Lafon et al. 2010, 2014). However, some manual and site-specific operations are always necessary because of the high variability in shape and characteristics of coastlines worldwide. These manual operations included in these so-called semi-automated algorithms allow calibrating some coefficients used at different steps of the algorithm (e.g. kernel size for computing textural parameters, characteristic length scale of the dunes and cliffs present in the image or DEM, thresholds on metrics of ground slope or on texture or on reflectance).

To the author knowledge, there is no published references specifically dealing with coastal dune foot line extraction from satellite imagery, apart from the work of Lafon et al. (2014) based on texture metrics, and also method based on multispectral image classification (Lafon et al., 2010; Roche et al., 2014). The dune foot is usually defined as the abrupt increase of slope observed at the transition between the upper beach (landward the berm) and the dune front (Boak and Turner et al., 2005; Toure et al., 2019). This cannot be detected directly from a satellite image. However, the transition between the beach and dune area is also marked by changes in surface reflectance and texture. Over the beach, the image reflectance is usually high and homogeneous while landward the dune face the reflectance can be lower and more heterogenous due to presence of vegetation and local shadows that typically appear in dune fields. The foredune face can also present a different spectral signature and typology compared to the upper beach. While extraction of a dune foot proxy from texture metrics requires VHR optical image, extraction from results of classifications applied to image reflectance signature and band ratios can also rely on HR image.

Studies focusing on coastal variability and in particular on the dunes system usually uses DEM (generated from DGPS or LIDAR topographic surveys or from photogrammetry that uses images taken from UAV, plane or satellite) to compute date-to-date changes in dune volume (e.g. Castelle et al., 2015; O'Dea et al., 2019; Laporte-Fauret et al., 2019). The DEM can also be used to extract the dune foot by using a slope threshold calibrated with ground observation (e.g. Nahon et al., 2019) or by using image processing methods for edge detection within raster of elevation (e.g. Richter et al., 2013). Analysing the slope variability in the cross-shore direction, with the search of the location of the first maximal slope increase from the upper beach, can also allows us detecting the dune foot (e.g. Le Mauff et al., 2018). However, except for coastal dunes suffering regular erosion events leading to a clear and sharp slope break, the transition between the upper beach and the dune face is sometimes blurred by sand sliding over the dune face to the dune base (Battiau-Queney et al., 2003). In that case the dune foot can no longer be represented by a line but more by a 2-3-m wide buffer area (Guillén et al., 1999). In case of coastal system undergoing accretion, the dune foot can even not be tracked rigorously, even by field works, as several embryo dunes form on the upper beach with vegetation usually developing on the top. These two morphodynamic processes represent potential source of errors in the detection of the dune foot from DEM, as only regular field works can check their occurrence in time and space. No any reference describing and validating methods for coastal dune foot extraction from satellite-image-derived DEM is found in the literature. Nevertheless, as production of coastal dune DEMs from optical spatial imagery using photogrammetry shows promising results (Almeida et al., 2019), the detection of the dune foot from space based on elevation and slope data appears feasible.

Detection of cliff lines in coastal areas can be done in similar ways as for the dune foot detection. Seaward the cliff foot is usually found find a gently sloping rocky platforms intermittently covered by sand or shingle deposits. Landward the cliff foot starts the cliff face, which is essentially characterised large elevation gradients at least an order of magnitude higher than those found elsewhere in the coastal area. A large variety of morphologies along the cliff face are observed worldwide due to different lithologies and processes involved in the cliff dynamic. The upper boundary of the cliff face, called top, is delimited the strong reduction of the ground slope and the start of more morphologically stable areas where vegetation and urbanisation can develop. For cliffs relatively steep shadows are usually projected on the cliff face seaward the cliff top due to obstruction of sunlight. This occurs when the earth-projected sun location is located landward the cliff top and when the sun elevation is lower than the cliff slope. Similar to the dune foot extraction, supervised classifications can be applied to extract the cliff lines based on these specificities. However, the success of the classification and the further extraction of cliff lines is essentially site specific and requires to identify consistent proxy of these line. Both VHR and HR optical images can be used, although extraction based on HR data will allow to detect significant changes within the cliff only if large temporal period are considered (e.g. 10-20 years) or if the cliff change rate are high (1-10 m/year), which is rarely the case.

Several methodologies for cliff line extraction were developed in the last decades relying on LIDAR-derived DEM but using different approaches. For instance, Gomes-Pereira and Wicherson (1999) applied image processing tools (mathematical operator) on rasterized DEM (elevation grid) to classify image pixels into 'slope pixel' or 'flat pixel'. Then, the cliff lines were assumed to be found at the boundary between the two classes of pixels and were identified by checking the 8-point neighbourhood of each pixels. Sui et al. (2002) also used image processing method (edge detection with the Canny operator) to a LIDAR-derived DEM transformed into a greyscale image. A more geometrically based approach exploiting the entire 3D information provided by the LIDAR measurements was addressed by Briese (2004). It consists in fitting planes to the 3D point cloud and identifying intersections between two adjacent planes, which locate either the cliff foot line or the cliff top line. With the same idea, Brzank et al. (2005) extended this approach by locally fitting a surface described by the hyperbolic tangent function to the cliff DEM. Then, geometrical analyses are made on the modelled surface to locate the two maxima in surface curvature (one convex and one concave) in cross-shore direction, which corresponds to the cliff foot and top, respectively. These methods however may fail with increasing coastal complexity and presence of vertical perturbation in the DEM unrelated to the ground elevation such as vegetation and buildings. A different approach was proposed by Liu et al. (2009) who exploited directly the elevation data provided by the DEM along a series of adjacent and regularly spaced transects oriented perpendicular to the cliff face. They based their approach on the conceptual representation of the cliff mentioned above, which is that the variation of the slope along the elevation profile is commonly greater at the top and the base of the cliff than anywhere else along the profile. Still using a transect-based approach Palaseanu-Lovejoy et al. (2016) introduced a new methodology that resolves easily the detection of the cliff foot and top along elevation profiles extracted from LIDAR-derived DEM. It even captures the presence of major irregularities along the cliff faces such as terrace that could represent a large source of error using previous methodologies.

For coastal managers, the beach width (Robertson et al., 2007) usually refers to the cross-shore distance over which the beach is most of the time dry and then fully available to welcome recreational activities. For beaches experiencing a micro tidal range, the beach width can reasonably be approximated by the cross-shore distance between the upper limit of the beach – marked by the dune or cliff foot or the base of defence structures – and the instantaneous waterline or the line passing through the middle of the swash zone. For beaches experiencing a larger (macro/mega) tidal range, the use of the mean high-water line as the proxy of the seaward boundary of the beach width is more appropriate (Burroughs and Tebbens, 2008; Richter et al., 2013, as it would limit the large horizontal fluctuations of this boundary that are associated with the daily water level fluctuations.

Differential SAR interferometry (Massonnet and Rabaute, 1993), allows measurements of land deformation very precisely with millimetre resolution. It has various applications in the fields of volcanology, cartography, crustal dynamics and land subsidence. By using large stacks of SAR images acquired over the same area, long deformation time series can be analysed using multitemporal differential SAR interferometry techniques. These coherent methods exploit either permanently coherent Persistent Scatterers (PSs) or temporally coherent Distributed Scatterers (DSs). PSs are typically artificial objects that reflect radar energy well such as metal structures and buildings. The PS methods that have been developed include the Permanent or Persistent Scatterer Interferometry (PSI). PSI provides a parametric estimation of the 3D location and velocity of each PS along the line of sight (LOS) connecting it to the satellite (Ferretti et al., 2000; Ferretti et al., 2001). Many such measurements are combined using PSI to produce highly accurate terrain motion maps. In urban areas where there is a prevalence of PSs, PSI allows analysis of even individual structures on the ground. The DS methods include algorithms such as SBAS. A DS object reflects lower radar energy compared to PSs and it usually covers several pixels in high resolution SAR images. These pixels exhibit similar scattering properties and can be used together for deformation estimation. SBAS estimates the deformation time series even in rural areas where the density of PSs is low (Berardino et al., 2002), such as in low urbanized deltaic environments.

3.3.3 Algorithm 3a – Dune foot extraction using the cross-shore variation of first-order texture metrics from VHR optical data

3.3.3.1 Algorithm description

- *Input data*

Texture analysis apply on very high-resolution optical data where shapes or regular patterns are recognisable. In coastal zone, this method has been developed and tested on Pléiades data. The method uses multispectral and panchromatic channels. This method is also adapted to WorldView image processing.

The algorithm needs a VHR optical image acquired over the beach and dune areas. The image of dimensions i lines and j columns must be rotated so as to have the coastline nearly aligned with the i-direction and to have the water and supratidal domain located in the left and right part of the image, respectively.

In addition, the algorithm requires two parameters defining the row-wise and column-wise length of the kernel in which the texture metrics are computed.

- *Algorithms*

The method is illustrated in Figure 3-11.

First, the multispectral image is classified to filter out woods and water surfaces. A supervised classification algorithm, trained by polygons chosen by the operator, is applied. Classification Trees and Maximum Likelihood classifiers have been applied successfully. Polygons are selected on water, foam, woods and sand (bare and covered by vegetation).

Sand pixels are distributed on the beach and dune. Sand pixels are used to create a mask. Simultaneously, a simple texture analysis is applied to the panchromatic channel. First order (occurrence) metrics are calculated (Anys, 1994). The Data Range metric is selected. Pixels of the data range image superposed to sand pixels are used for feature extraction.

Two discontinuities are looked for in the masked data range image. They are iteratively searched for in a 6x3 moving window. The window moves from water to woods. The first discontinuity is defined by a threshold characterised on the standard deviation value of the data range in the window. This first discontinuity has been defined as the upper limit of the landward excursion of tide. Once the threshold is reached the interface location (point) is stored vector file. Then, the window continues moving landward and mean and standard deviation of the data range in the window are calculated. Two thresholds are defined to determine the location of a second discontinuity characterising the foot dune. The location of the second discontinuity is stored.

Interface locations are further analysed to realign doubtful detection (dots located far away from direct neighbours).

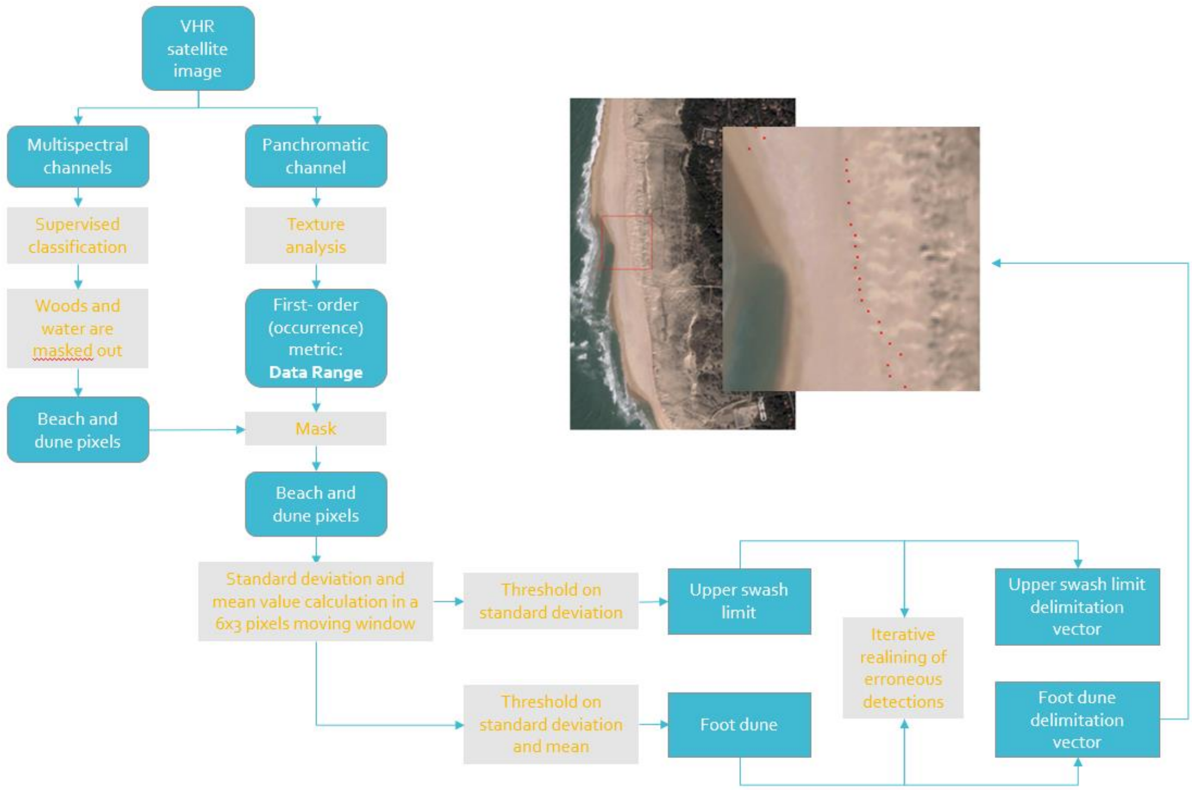

Figure 3-11 – Flow chart for due foot extraction algorithm

- *Tools*

Computations can be made using ENVI software and IDL programming language. Supervised classification and threshold definitions need operator intervention.

- *Output product*

Two vectors consisting of point are obtained as a result.

3.3.3.2 Validation

This detection strategy has been applied along various sandy coasts in France. Foot dune detection has been validated by GPS surveys. Validation consists of 6057 individual measurements realized on the dune foot only. The error bar of field surveys is of 5 m on average (operator effect). It has been established that almost 70% of the Pleiades-based foot dune detection is better that 5 m (Lafon et al., 2014). Remaining errors should be corrected manually, based on image photo-interpretation.

3.3.3.3 Application range and Maturity

No cloud nor shadow must be present within the domain on which the algorithm is applied. In the current state of the algorithm, the coastline must be relatively rectilinear, and the image must contain water, beach and dune areas.

The method has been applied to detect the dune foot over four regions of the French Atlantic coast, one of them being located a few kilometers to the north of Biscarrosse POC site (France, Nouvelle Aquitaine region). Also, it has been tested along the Mediterranean coast (a 40 km-long coastline to the east of Palavas-les-Flots) to retrieve the middle of the swash zone.

Although these experimentations have shown good a potential, the method must be strengthened and generalized. For more complex environment further developments may be required (e.g. removal of rocky patches within the beach area, compatibility with highly-curved coasts). However, with regards to POC, it is considered as mature, but it necessitates the calibration of the detection thresholds for each considered image.

3.3.4 Algorithm 3b – Dune foot extraction based on beach/dune slope from DEM

3.3.4.1 Algorithm description

- *Input data*

This algorithm relies on the availability of a digital elevation model (DEM) that includes the dune and the upper part of the beach so as to have the dune foot within the DEM. The DEM can be computed from photogrammetry using VHR optical images or from interferometry or stereo-radargrammetry using VHR SAR images (see algorithm group 1 Section 3.1). The proposed algorithm for dune foot extraction relies on a DEMs provided over a regular mesh.

The proposed algorithm is expected to require some tuning coefficient that surely will depend on the characteristic dimensions of the beach/dune system, such as the average dune height, dune slope and beach slope.

The proposed algorithm is expected to be able to detect automatically a reference line within the dune system (located in between the dune foot and dune apex) used to define perpendicular transects along which the dune foot detection will be performed. However, if this part of the algorithm lacks robustness, it may be necessary to provide the reference line or the transects for each POC site.

- *Algorithms*

The algorithm has not been implemented and tested yet and the proposed structure may require further improvement. It is largely inspired from the transect-based approach of Le Mauff et al. (2018). The main steps of the algorithm are presented in Figure 3-12, grey and yellow boxes indicating the main inputs, the sub-algorithms to be developed and the algorithm and sub-algorithm outputs, respectively. The overall idea is to detect the location of particular changes in beach/dune slope along regularly-spaced transects locally perpendicular to the dune front. Indeed, in presence of high coastal dunes a significant increase of the slope is observed at the transition between the upper beach and the dune face. For instance, a slope increases from 10 to 47 ° is observed at Cap Ferret beaches (SW France) by Nahon et al. (2019). The first main steps of the algorithm is to identify a line approximating the dune face location from which perpendicular, regularly-spaced detection transects will be defined. Then, along each of these transect the cross-shore variability of the ground slope is analysed. In particular, inflexion points in the slope, which are characterized by the second derivative of the elevation equal to zero, are tracked as they might be the best proxy for transitions between gentle beach slope and steeper dune face. Here, only tests one real DEMs will allow robust implementation of this critical part of the algorithm. Existing methodologies for cliff lines detection will also be used as support for this implementaiton (e.g. Liu et al., 2009; Palaseanu-Lovejoy et al, 2016).).

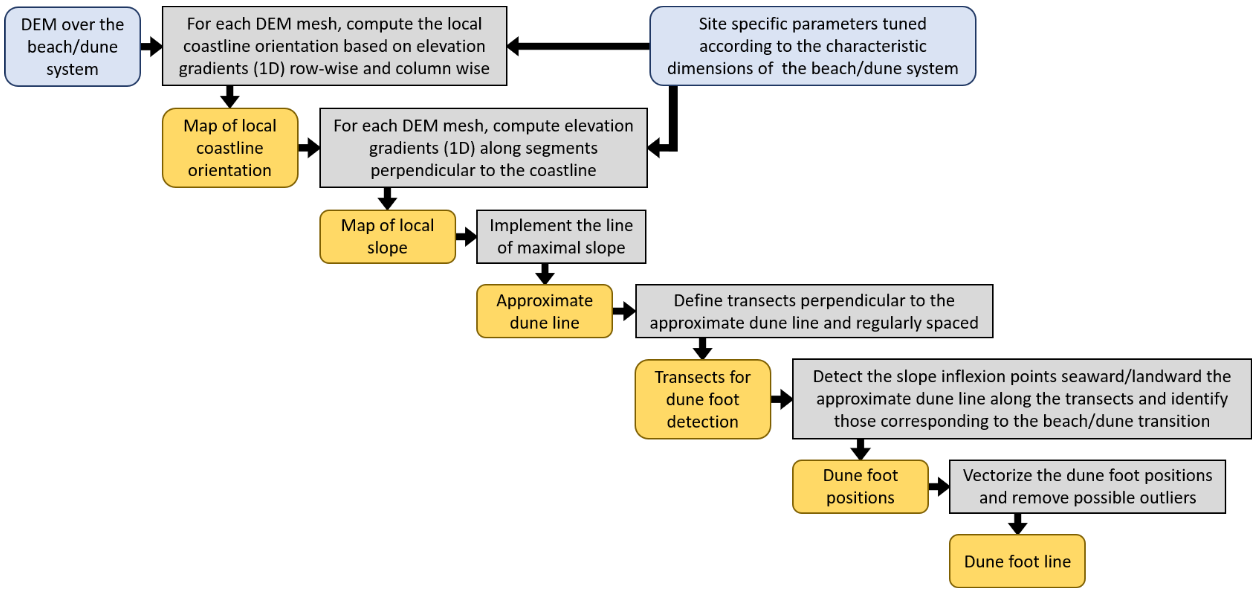

Figure 3-12 – Methodology proposed to extract the dune foot line from DEMs

- *Tools*

Python programming language.

- *Output product*

The output of this algorithm is a vector of dune foot positions such as shown in Figure 3-13.

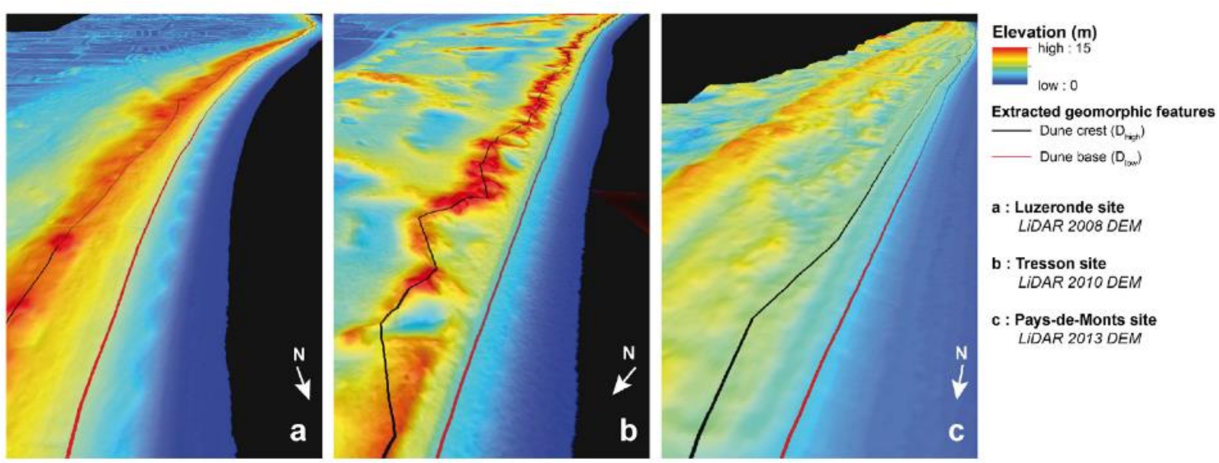

Figure 3-13 – Example of dune base/foot (red line) and crest (black line) extracted from LIDAR-derived DEM using transect-based approach and analyses of the slope variability. Extracted from Le Mauff et al. (2018).

3.3.4.2 Validation

Not performed yet. The algorithm will be further tested in the POC. The maximal horizontal accuracy is expected to be of the order of the DEM resolution, with DEM horizontal resolution usually set to the double of the resolution of the original images. Thus, for a DEM perfectly well computed using Pleiades images of 0.5-m resolution the horizontal accuracy in dune foot detection would be of the order of 1 m. A lower accuracy is however likely as the image georeferencing of the images may not be totally perfect and mainly because slope break extraction from discrete elevation data can introduce errors. Thus, the overall accuracy of the proposed algorithm is more expected to be of 2-5 m if used with VHR data.

3.3.4.3 Application range and Maturity

For relatively stable or accreting dunes, the break in the slope at the transition between the beach and the dune becomes no longer detectable and vegetation may be even present at the base of the dune foot. In that case, the proposed algorithm may fail. An alternative to go on the monitoring of the coastline over the long-term is to take seaward extent of vegetation present on the beach, if exists. This is no integrated in the present algorithm. To our knowledge there is no published algorithm for automated dune foot detection based on DEM derived from satellite imageries, making difficult to assess the feasibility of our algorithm. This method is not compatible with the use of HR images, as the planimetric resolution of such EO data are not enough to compute a DEM describing well the beach and dune morphology. The maturity of the proposed algorithm is considered as low, though a first implementation within some weeks is likely reachable.

3.3.5 Algorithm 3c – Cliff line extraction using the cross-shore variation of the beach/cliff slope

3.3.5.1 Algorithm description

- *Input data*

This algorithm relies on the availability of a digital elevation model (DEM) that includes the cliff face and part of the subaerial domains seaward and landward the cliff face so as to have the cliff foot and apex within the DEM. The DEM can be computed from photogrammetry or stereo-radargrammetry using VHR optical images or from interferometry using VHR SAR images (see algorithm group 1 Section 3.1). The proposed algorithm for cliff foot extraction relies on a DEMs provided over a regular mesh.

The proposed algorithm is expected to require some tuning coefficient that surely will depend on the characteristic dimensions of the cliff system, such as the average cliff height and slope.

The proposed algorithm is expected to be able to detect automatically a reference line following locally the overall cliff face orientation that is used to define perpendicular transects along which the cliff foot and apex detection will be performed. However, if this part of the algorithm lacks robustness, it may be necessary to provide the reference line or the transects for each POC site.

- *Algorithms*

The algorithm has not been implemented and tested yet and the proposed structure may require further improvement. The main steps of the algorithm are presented in Figure 3-14 with blue, grey and yellow boxes indicating the main inputs, the sub-algorithms to be developed and the algorithm and sub-algorithm outputs, respectively. The overall idea is to detect the location of particular changes in slope along regularly-spaced transects locally perpendicular to the cliff face. Indeed, landward the sea the beginning of the cliff face is usually characterized by a strong increase of the slope at the cliff foot and a strong decrease at the cliff apex. Seaward the cliff foot and landward the cliff apex the slope is weak while in between the slope is high while. The first main step of the algorithm is to identify a line approximating the cliff face location from which perpendicular, regularly-spaced detection transects will be defined. Then, along each of these transect the cross-shore variability of the ground slope is analysed. In particular, inflexion points in the slope, which are characterized by the second derivative of the elevation equal to zero, are tracked as they might be the best proxy for transitions between the different coastal compartments. Here, only tests one real DEMs will allow robust implementation of this critical part of the algorithm. Existing methodologies (e.g. Liu et al., 2009; Brzank et al., 2005) for cliff lines detection will be investigated to support the algorithm implementation.

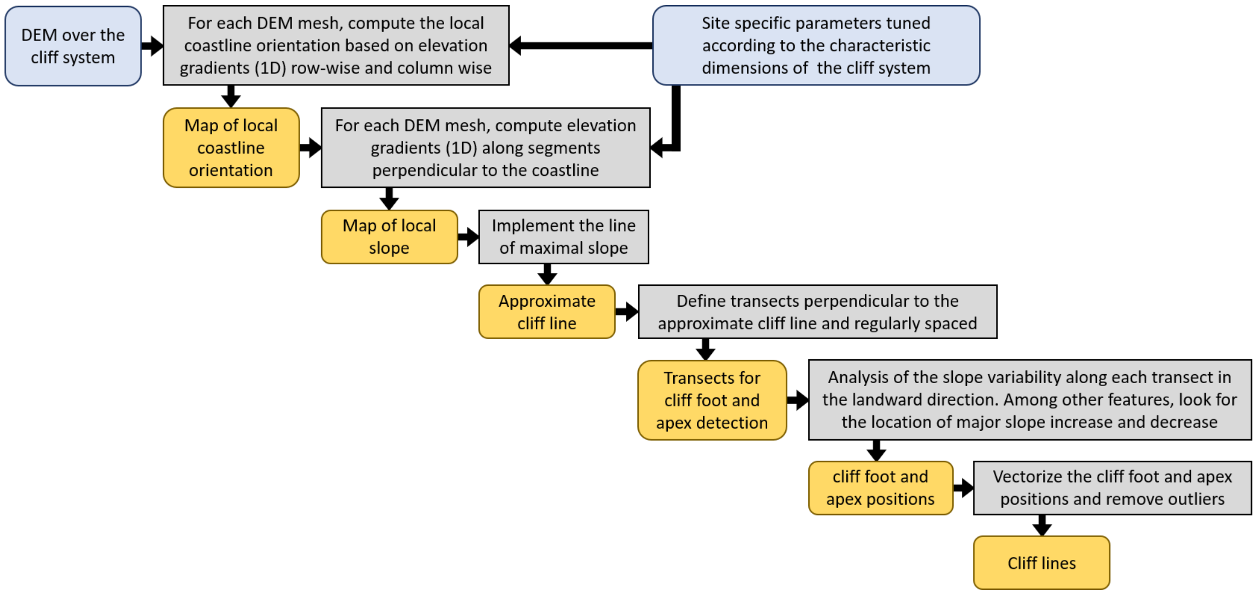

Figure 3-14 – Methodology proposed to extract the cliff lines from DEMs

- *Tools*

Python programming language.

- *Output product*

The outputs from this algorithm are vectors of cliff foot and cliff apex positions.

3.3.5.2 Validation

Not performed yet. The algorithm will be further tested in the POC. As for the dune foot line extraction algorithm the maximal horizontal accuracy is expected to be of the order of the DEM resolution, with DEM horizontal resolution usually set to the double of the resolution of the original images. Thus, for a DEM perfectly well computed using Pleiades images of 0.5-m resolution the horizontal accuracy in dune foot detection would be of the order of 1 m. A lower accuracy is however likely as the image georeferencing of the images may not be totally perfect and mainly because slope break extraction from discrete elevation data can introduce errors.

3.3.5.3 Application range and Maturity

Coastal cliffs within Europe present a great variety of shapes in both the horizontal and vertical directions making nearly impossible to have a single automated algorithm applicable to all cliff geometries. Here, the proposed algorithm will be developed essentially for cliffs of simple geometry (e.g. relatively straight in top view, low ground slope seaward the cliff foot and landward the cliff top, no multiple detachments of the cliff in the cross-shore direction). The proposed algorithm also assumes that the cliff foot is always located seaward the cliff apex, which is not always true as for cliffs made of hard materials and suffering rapid wave-induced erosion at their base. In case the sea is directly in contact with cliff face within the EO data used to compute the DEMs, the cliff foot line detection with the proposed algorithm is no longer possible. Instead the line of contact between the sea and the cliff face may be a relevant proxy of the cliff foot line. The detection of the cliff apex is still possible as long as the cliff face (in contact with the sea) covers several meshes within the DEM. The maturity of the proposed algorithm is considered as low, though a first implementation within some weeks is likely reachable.

3.3.6 Algorithm 3d – Manual linear feature extraction from DEMs (3D digitization)

3.3.6.1 Algorithm description

Photogrammetric techniques have been used in the past for accurate 3D reconstructions/reconstitutions and specifically for extracting 3D point coordinates (X, Y, Z) as well as 3D lines. For this purpose, the appropriate stereo pair must be available, while the extraction is a point-by-point process which in the past used to be manual.

Following the development of analytical stereo-plotters this process became semiautomatic, while nowadays, with the availability of digital images and digital photogrammetric solutions, cost-effective almost-automated methods are widely offered for any visual-based measuring purpose. Even though, the automation of the photogrammetric production chain is almost automated, still human operators are required and they play a major role in the whole process.

The first step if this is algorithm the restitution of relative orientation of the stereo-model, which is performed with the computation of the aerial triangulation/bundle adjustment. In the case of VHR optical satellite imagery it is done by deploying the RPC coefficients model approach (refer to paragraph 4.1.1).

- *Input data*

Vector file output: Point cloud file "*.las".

- *Tools*

DTMaster stereo, INPHO Photogrammetric Suite by Trimble.

ArcGIS-ESRI, QGIS.

- *Output product*

Vector file output: "*.shp", "*.dxf".

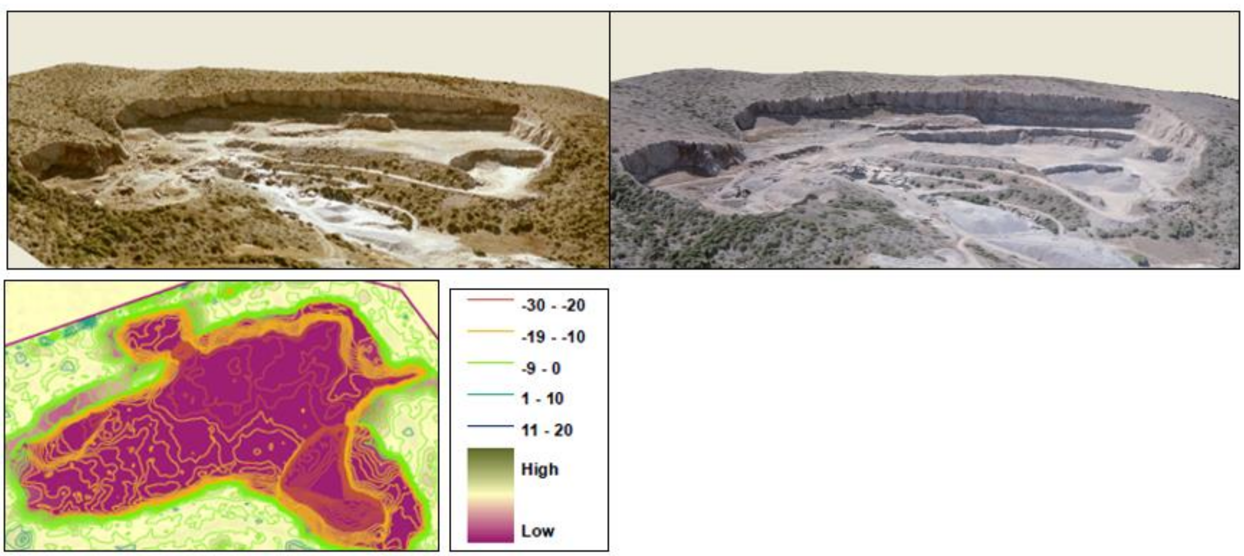

Figure 3-15: DEMs generated by VHR optical data, time series 2007-2009 over cliff areas. Manual Linear Feature Extraction (breaklines) from DEMs along with difference model 2007-2009 (low: erosion, high: accretion) (Terra Spatium, ©2016).

3.3.6.2 Validation

The results of algorithms are being validated through *in situ* GPS measurements, for this reason points lying on cliff foot and apex are being collected through an on-the-field survey, with an accuracy of 2-3cm. These collected points are being compared with their homologous points identified on the 3D extracted lines. Of course, this set of points is being identified in order to anticipate project and area specificities. According to past commercial projects executed by Terra Spatium, that exploit VHR optical data, an accuracy of 3-4 times the pixel size is being reported.

In the framework of Space for Shore, the cliff lines produced within the Greek test sites, will be validated with *in situ* GPS measurements during a land survey. This field work will take place in late-September 2019, mid-October and could be combined along with the validation activities for 4.2.6.2 (Algorithm 2d – Water Line Detection using binary products from SAR amplitude data).

3.3.6.3 Application range and Maturity

The maturity of the deployed algorithms is considered high, while in order to achieve a high accuracy, Ground Control Points (GCPs) are needed for the computation of the aerial triangulation. In cases that VHR satellite optical imagery (e.g. Pleiades) is used along with GCPs (measured on the ground) the relative vertical accuracy achieved is around 2meters.

3.3.7 Algorithm 3e – Beach width computation

3.3.7.1 Algorithm description

- *Input data*

This algorithm requires several inputs:

- A reference line that is used to compute the beach width. This reference line can be the foot of the dune, cliff or coastal defence or any other line meaningful to end-users.
- A water line that is used to compute the beach width. This waterline can be extracted from optical or SAR HR/VHR images.
- The tide level at which the end-user wants the beach width to be computed. For instance, some end-users will prefer to know the beach width at high tide to assess the recreative potential of their beach.

- *Algorithms*

Roughly, the beach width is computed as the distance between a reference line denoting the foot of either the dune, or the cliff, or a defence structure and the waterline computed at low tide (total beach width), high tide (upper beach width) or using a time-averaged waterline (mean beach width in microtidal environment). Waterline is detected using algorithm of group 2 (refer section 3.2). For instance, along sandy coast experiencing large tidal variation the beach width will correspond to the distance between the dune foot and the waterline at high tide such as shown in Figure 3-16. This distance will be computed along transects perpendicular to the reference line and regularly spaced (10 – 100 m). An alongshore interpolation of the beach width may be required to produce a more continuous data. In area with microtidal environment the middle of swash zone appears as the best proxy of the waterline to compute the mean beach width.

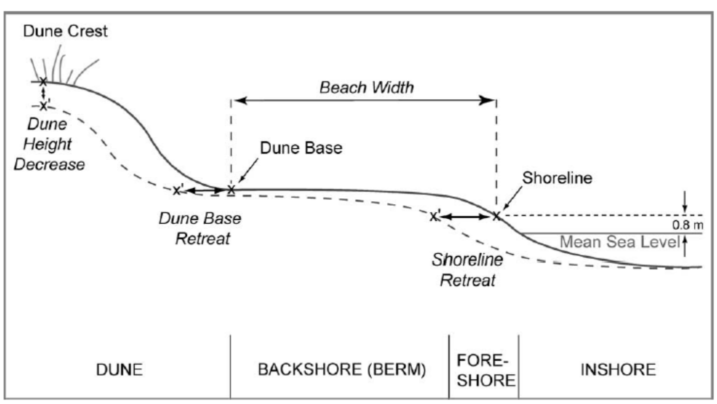

Figure 3-16 – Schematic view of a typical beach elevation profile (cross-shore view) along sandy coasts where the beach width definition is indicated. The 0.8-m water level use to define the shoreline position correspond to the highest water level resulting from tide effect. Extracted from Burroughs and Trebbens (2008).

- *Tools*

Python, QGIS, DSAS (?)

- *Output product*

Shapefile containing the reference line and the corresponding beach width along that line.

3.3.7.2 Validation

This algorithm has not been tested and validated yet. The horizontal accuracy of this algorithm is conditioned by both the accuracy of the waterline and the reference line. In case the reference line is provided by the end-user (no spatial error) and not derived from satellite imagery, the accuracy reduces to the accuracy of the water line extraction algorithm, which usually is of the order of the image pixel resolution (sub-metric to pluri-metric).

3.3.7.3 Application range and Maturity

The algorithm has not been implemented and tested yet. The maturity is then very low. However, the implementation of the algorithm will be quite straightforward without many specific cases. This algorithm will apply to any beaches (e.g. sandy, shingle) as long as the waterline can be extracted from optical of SAR images.

3.3.8 Algorithm 3f – Top-of-the-cliff vertical movement monitoring using PSI

3.3.8.1 Algorithm description

- *Input data*

The algorithm uses essentially SAR SLC Sentinel 1A and 1B scenes.

- *Algorithms*

Persistent scatterer interferometry (PSI) is a widely used method to monitor slow movements due to tectonics, subsidence, landslides etc. This method detects deformation rates, in linear and non-linear scale. The Interferometric Point Target Analysis (IPTA) will be applied using a dataset of more than a hundred SLC S1A and S1B scenes, using a single reference point. Persistent scatterers are detected on man-made structures mostly, which is most valuable in order to monitor possible subsidence in coastal inhabited areas. This algorithm will be mainly applied to coastal areas presenting coastal cliffs. The main steps of the algorithm are:

- Subset
- Amplitude
- Reference point selection
- Atmospheric phase removal
- Persistent scatterer selection

- *Tools*

GAMMA-IPTA, Sarproz

- *Output product*

Deformation maps on top of cliffs showing line-of-sight movement.

3.3.8.2 Validation

The algorithm has not been properly validated yet on coastal cliff.

3.3.8.3 Application range and Maturity

Maturity of the algorithm is intermediate, as preliminary tests are currently performed along with ongoing improvements of the whole processing chain.

3.3.9 Algorithm 3g – Intertidal creek morphological characteristics

3.3.9.1 Introduction

The characterisation of the intertidal flat morphology is one aspect to investigate the changes and erosion patterns in this very dynamic ecosystem. The creek heads and edges react very fast on changing sediment types and can show first tendencies of erosion processes. Within this project it is envisaged to combine existing classification methods (Müller et al. 2016) with new ideas for the retrieval of an indicator for the tidal creek morphology.

3.3.9.2 State-of-the-art

A classification scheme for intertidal flat monitoring is currently implemented (see chapter 3.5.5) for the general overview on inertial flat habitats. Some of the optical indicators that are used for this classification shall be investigated for their ability to characterise the intertidal creek headings. Beside this optical approach, also SAR data have been analysed for spatiotemporal trends in intertidal bedforms, e.g. by Adolph et al. 2017 or Gade & Melchionna et al. 2016.

3.3.9.3 Algorithm description

This experimental algorithm shall provide information about the structure of tidal creek heads. It will use spectral indicators that used to characterise the sediment of intertidal flat areas and that is derived from linear spectral unmixing. The higher the spatial resolution the better as the structures can be very small scale. After identification of the creek endings, a transect will be used for detecting the deeps and heights of the creeks, which are mainly characterised by differences in brightness. Directional filters are applied in order to highlight the linear structures of creeks (Figure 3-17).

Figure 3-17: Band combination from S-2 bands for enlighten tidal creek heads (left) and directional filter (right)

- *Input data*

Sentinel-2 and VHR acquired during low tide.

- *Algorithms*

Linear Spectral Unmixing for retrieving water covered and dray fallen tidal flats and sediment differences.

Transects perpendicular to the tidal creek heads will provide profile information about sediment changes.

- *Tools*

SNAP, tabulated data analyses such as Excel

- *Output product*

Transect plots

3.3.9.4 Validation

The algorithm is experimental and will need testing during POC.

3.3.9.5 Application range and Maturity

It is envisaged to test it on different small regions in order to find out if the information is sufficient for the user requirements. In this stage of the development, many manual steps will be needed, and the algorithm is not mature, yet.

3.3.10 Algorithm 3h – Dune foot extraction using supervised classification

3.3.10.1 Algorithm description

- *Input data*

This algorithm is designed to work with HR multispectral images, although its relevance depends on (i) the average change rate and (ii) the duration of the temporal window addressed.

The slower the dune transition move and the shorter the temporal window is, the higher the resolution must be. For instance, image resolution of the order of 10 m, such as provided by Sentinel-2 and SPOT4-5, is enough to assess the coastal dune foot retreat during the past 25 year in SW France where the average retreat rates are larger than 0.5-1/yr.

- *Algorithms*

Supervised classification method (algorithm 5a) is applied to distinguish the beach area made of sand from the dune area which is usually covered by vegetation or if not by sand ridge casting shadows around. The most seaward contour of the vegetated dune class is taken as the proxy of the dune. Visual inspection of automatically extracted dune foot lines is necessary to allow manual correction/digitization in case the classifier fails in some regions of the study domain.

- *Tools*

The algorithm uses bash and python programming languages with support of sci-kit learn, Orfeo ToolBox and GDAL libraries. QGIS will be used for visual inspection and digitalization.

- *Output product*

The output of this algorithm is a vector of dune foot positions.

3.3.10.2 Validation

The algorithm is experimental and will need testing during POC. However, according to Vos et al. (2019) subpixel accuracy can be reached for waterline extraction along sandy beaches based on supervised classification. Here, an accuracy of the order of the pixel size is expected as the transition between the dune system and the beach is less clear than for the transition between the water and the beach.

3.3.10.3 Application range and Maturity

This algorithm should provide accurate results only for coastal areas with well-developed dunes covered by vegetation and showing relatively narrow dune face with respect to the image resolution. In case the transitional area between the beach and dune system is wide the extracted interface will correspond more to the dune scarp top line. Also, the comparison of subsequent dune foot lines will only be relevant if addressing temporal period large enough so that the observed changes are larger than the image resolution. While the classification method and diverse regularization methods are used routinely, the reference database for this kind of application need to be built by manually digitizing reference polygons over a subset of images. The algorithm can be considered as almost mature.

3.3.11 Algorithm 3i – Cliff line extraction using supervised classification

3.3.11.1 Algorithm description

- *Input data*

This algorithm is designed to work with HR multispectral images, although its relevance depends on (i) the average change rate and (ii) the duration of the temporal window addressed. HR SAR data can also be used, specifically for the dune foot detection.

The slower the cliff lines move and the shorter the temporal window is, the higher the resolution must be. For instance, image resolution of the order of 10 m, such as provided by Sentinel-2 and SPOT4-5, is may be enough to detect small cliff retreat during the past 25 year at Erretegia cliffs (SW France) where large landslides have occurred or along some cliffs in Normandy (N France) which are particularly dynamic.

According to the geometry and surface typology of the cliff studied and according to which lines (cliff top and/or cliff foot), the images used in the supervised classification must: (i) contain particular spectral features; and/or (ii) be acquired at particular tide level; (iii) and/or be acquired with particular viewing angle and sun elevation.

For instance, the presence of shadows seaward the cliff top will help detecting the cliff top, while it may prevent form detecting the cliff foot. The presence of a ground cover landward the cliff top with spectral signature very different from what can be observed on the cliff face and seaward is also crucial. Also, the use of images only acquired at high tide may allow detecting the cliff base at some sites where the cliff face is steep and when the satellite field of view is not obstructed by the cliff top.

- *Algorithms*

Regardless of the type of cliff line to be detected, a supervised classification method (algorithm 5a) is applied to discriminate the different classes of ground cover, the main ones being: water; wet/dry sand/shingle beach; rock; terrestrial vegetation; urbanization; mix of vegetation and urbanization; shadow. Then, distinct strategies are used for the extraction of cliff foot and cliff top. These extraction strategies are site-specific and can be fully described/implemented only once a minimal knowledge about the site is reached and following an analysis of the image dataset to identify what are the features consistently present in the images.

Cliff top: Usually the cliff top line will be located by the boundary between the classes: terrestrial vegetation; urbanization; mix of vegetation, and the other classes located seaward the cliff top such as the classes of: water, wet/dry sand/shingle, rock. The combination of steep cliff faces oriented in a direction opposite to the sun position, low sun elevation will cause shadows to appear. In that case, the cliff top line is easily located by the boundary between the classes: terrestrial vegetation; urbanization; mix of vegetation, and the class: shadow.

Cliff foot: For cliff suffering erosion mainly from wave attacks, it can be reasonably assumed that during highest tide level the water domain will be in direct contact with cliff, without presence of beach or low-slopping rocky platforms in between. In case the geometrical conditions of the cliff regarding the sun exposition ensure that no any shadow is projected down the cliff, a relevant proxy for the cliff foot is the waterline at high tide. However, the tide level at high tide varies from one date to another due to varying tide cycle and the presence of wave set-up and storm surge. Unless the cliff is a vertical wall, these variations lead to meter-scale horizontal shifts of the waterline along the cliff face. The use of the latter proxy is then relevant only for steep cliffs and for addressing long-term changes, which both make the errors introduced by the latter reasoning negligible.

A necessary condition for cliff line extraction is the use of images acquired with a low viewing angle. The closer to the nadir the image is acquired the more accurate will be the positioning of the cliff lines. Basically, even after image georeferencing, a sensor located over the water domain imaging the cliff face will tend to put the pixels of cliff top too much landward. The opposite phenomenon occurs for a sensor located over the land domain with a tendency to shift seaward the top of the cliff. For this latter mode of acquisition, the cliff foot may also not be seen by the sensor when the cliff face is steep enough.

A narrow buffer area along the cliff (indicating where the cliff lines are expected to be found) has to delimited to drive the identification of the inter-class boundaries corresponding to the cliff lines. Finally, a visual inspection of automatically extracted cliff lines is necessary to allow manual correction/digitization in case the classifier fails in some regions of the study domain.

- *Tools*

The algorithm uses bash and python programming languages with support of sci-kit learn, Orfeo ToolBox and GDAL libraries. QGIS will be used for visual inspection and digitalization.

- *Output product*

The output of this algorithm is a vector of cliff foot and/or cliff top positions.

3.3.11.2 Validation

The algorithm is experimental and will need testing during POC. Considering the numerous potential sources of errors and misinterpretations a maximal accuracy of the order of the pixel size is expected.

3.3.11.3 Application range and Maturity

As discussed previously in this section, this algorithm may not be applicable to all cliffs and designed of the algorithm is mostly site-specific. Also, the comparison of subsequent cliff lines will only be relevant if addressing temporal period large enough so that the observed changes are larger than the image resolution. While the classification method and diverse regularization methods are used routinely, the reference database for this kind of application need to be built by manually digitizing reference polygons over a subset of images. Additionally, the automated extraction of the boundaries between several type of class will require significant developments. The maturity of this algorithm can then be considered as low.

3.3.12 References

Adolph, W., Schückel, U., Soo Son, C., Jung, R., Bartholomä, A., Ehlers, M., Kröncke, I., Lehner, S., Farke, H. (2017): Monitoring spatiotemporal trends in intertidal bedforms of the German Wadden Sea in 2009–2015 with TerraSAR-X, including links with sediments and benthic macrofauna.- Geo-Marine Letters, April 2017, Volume 37, Issue 2, pp 79–91

Almeida L.P., Almar R., Bergsma E., Berthier E. Baptista P., Garel E., Dada O., Alves B, 2019. Deriving High Spatial-Resolution Coastal Topography From Sub-meter Satellite Stereo Imagery, Remote Sensing, 11(5), 590, doi:10.3390/rs11050590.

Anys, H., A. Bannari, D. C. He, and D. Morin. "Texture analysis for the mapping of urban areas using airborne MEIS-II images." Proceedings of the First International Airborne Remote Sensing Conference and Exhibition 3 (1994): 231-245.

Battiau-Queney, Y., Billet, J.F., Chaverot, S., Lanoy-Ratel, P., 2003. Recent shoreline mobility and geomorphologic evolution of macrotidal sandy beaches in the north of France, Marine Geology, 194, pp. 31-45,doi: S0025-3227(02)00697-7.

Boak, E.H. and Turner, I.L., 2005. Shoreline definition and detection: A review. Journal of Coastal Research, 21(4), 688–703. doi:10.2112/ 03-0071.1

Brzank, A., Lohmann, P., Heipke, C., 2005. Automated extraction of pairwise structure lines using airborne laser scanner data in coastal areas, International Archives of Photogrammetry and Remote Sensing, ISPRS Workshop Laser Scanning 2005, Enschede, Netherlands, 36, Part 3/W19, pp. 36–41.

Burroughs, S.M., Tebbens, S.F., 2008. Dune Retreat and Shoreline Change on the Outer Banks of North Carolina, Journal of Coastal Research, 24(2b), 104–111, doi:10.2112/05-0583.1.

Castelle, B., Marieu, V., Bujan, S., Splinter, K.D., Robinet, A., Sénéchal, N., Ferreira, S., 2015. Impact of the winter 2013–2014 series of severeWestern Europe storms on a double-barred sandy coast: Beach and dune erosion and megacusp embayments, Geomorphology, 238, p. 135-148, doi:10.1016/j.geomorph.2015.03.006.

Ferretti, A., Prati, C., Rocca, F., 2000. Nonlinear subsidence rate estimation using permanent scatterers in differential SAR interferometry. IEEE Transactions on Geoscience and Remote Sensing, 38 (5), 2202–2212.

Ferretti, A., Prati, C., Rocca, F., 2001. Permanent scatterers in SAR interferometry. IEEE Transactions on Geoscience and Remote Sensing, 39 (1), 8-20.

Berardino, P., Fornaro, G., Lanari, R., Sansosti, E., 2002. A new algorithm for surface deformation monitoring based on small baseline differential SAR interferograms. IEEE Transactions on Geoscience and Remote Sensing, 40 (11), 2375-2383.

Gade, M., and Melchionna, S., 2016: Jint Use of Multiple Synthetic Aperture Radar Imagery for the Detection of Bivalve Beds and Morphological Changes on Intertidal Flats, Estuar. Coast. Shelf Sci., 171, 1-10, doi:10.1016/j.ecss.2016.01.025.

Guillén, J., Stive, M.J.F., Capobianco, M., 1999. Shoreline evolution of the Holland coast on a decadal scale. Earth Surf. Process. Landforms, 24, p. 517-536.

Hapke, C.J. and Reid, D., 2007. National Assessment of shoreline change, Part 4: Historical coastal cliff retreat along the California coast. USGS Open-File Report 2007–1133, 51p.

Hoeke, R.K., G.A. Zarillo, and M. Synder, 2001. A GIS based tool for extracting shoreline positions from aerial imagery (Beach-Tools), Proceedings of ERDC/CHL CHETN-IV-37.

Lafon V., Hoareau A., Mallet C., Desprats J.-F, 2010. Suivi du trait de côte en Aquitaine par imagerie Formosat-2. Actes des 10ièmes JNGCGC, Sables D'Olonne, vol. 2, p. 497-504.

Lafon, V., Dehouck, A., Robinet, A., Marieu, V., Curti, C., Durou N., 2014. Détection d'indicateurs géomorphologiques littoraux par télédétection à très haute résolution spatiale (pp. 601-610), doi:10.5150/jngcgc.2014.066.

Laporte-Fauret, Q., Marieu, V., Castelle, B., Michalet, R., Bujan, S., Rosebery, D., 2019. Low-Cost UAV for High-Resolution and Large-Scale Coastal Dune Change Monitoring Using Photogrammetry, Journal of Marine Science and Engineering, 7(3), 63, doi: 10.3390/jmse7030063

Le Mauff, B., Juigner, M., Ba, A., Robina, M., Launeaub, P., Fattal, P., 2018. Coastal monitoring solutions of the geomorphological response of beach-dune systems using multi-temporal LiDAR datasets (Vendée coast, France), Geomorphology 304, P., 121–140, doi: 10.1016/j.geomorph.2017.12.037.

Liu, J.K., Li, R., Deshpande, S., Niu, X., Shih, T.Y., 2009. Estimation of Blufflines Using Topographic Lidar Data and Orthoimages, Photogrammetric Engineering & Remote Sensing, 75, pp. 69–79.

Nahon, A., Molina, P., Blázquez, M., Simeon, J., Capo, S., Ferrero, C., 2019. Corridor Mapping of Sandy Coastal Foredunes with UAS Photogrammetry and Mobile Laser Scanning, Remote Sensing, 11(1352), doi:10.3390/rs11111352.

O'Dea, A., Brodie, K. L., Hartzell, P., 2019. Continuous Coastal Monitoring with an Automated Terrestrial Lidar Scanner, Journal of Marine Science and Engineering, 7, 37, doi:10.3390/jmse7020037.

Toure, S., Diop, O., Kpalma, K., Maiga, A.S., 2019. Shoreline Detection using Optical Remote Sensing: A Review, International Journal of Geo-Information, 8, 75, doi:10.3390/ijgi8020075.

Richter, A., Faust, D., Maas, H.G., 2013. Dune cliff erosion and beach width change at the northern and southern spits of Sylt detected with multi-temporal Lidar, Catena, 103, p. 103-111, doi:10.1016/j.catena.2011.02.007.

Robertson, W., Zhang, K., Whitman, D., 2007. Hurricane-induced beach change derived from airborne laser measurements near Panama City, Florida. Marine Geology, 237, p. 191–205, doi:10.1016/j.margeo.2006.11.003.

Roche, A., Bosc, C., Chandelier, L., Lagnous, R., 2014. Apport de l'imagerie satellitaire pour le suivi du trait de côte. XIIIèmes Journées Nationales Génie Côtier – Génie Civil Dunkerque, 2-4 juillet 2014, doi:10.5150/jngcgc.2014.068.

Zarillo, G.A., J. Kelley, V. Larson, 2008. A GIS Based Tool for Extracting Shoreline Positions from Aerial Imagery (BeachTools) Revised, Proceedings of ERDC/CHL CHETN-IV-73.

3.4 Algorithm group 4: Bathymetry

3.4.1 Introduction

The knowledge about nearshore bathymetry is of paramount importance to oceanography research, management and economic activities. Nevertheless, bathymetric data acquisition in shallow waters (0 to 50 m) with traditional methods (e.g., single and multi-beam echo sounder) have disadvantages such as safety and cost. For these reasons, satellite remote sensing has become increasingly important in the bathymetry estimation. Some works have delved into swell properties in the nearshore area due to the interaction with the sea-bottom to infer the bathymetry (e.g., Brusch et al.,2011; Mishra et al., 2014; Pereira et al., 2019) (Figure 3-18). Other works focused on the use optical satellite sensors to retrieve bathymetry either by (1) calibrating an empirical model with *in situ* survey data (e.g. Lyzenga et al., 2006) or (2) calibrating a radiative transfer model which decomposes the radiometric intensity recorded at the water surface into contributions from the water column and the water bottom (Lee et al., 2002; Capo et al., 2014, Dekker et al., 2011).

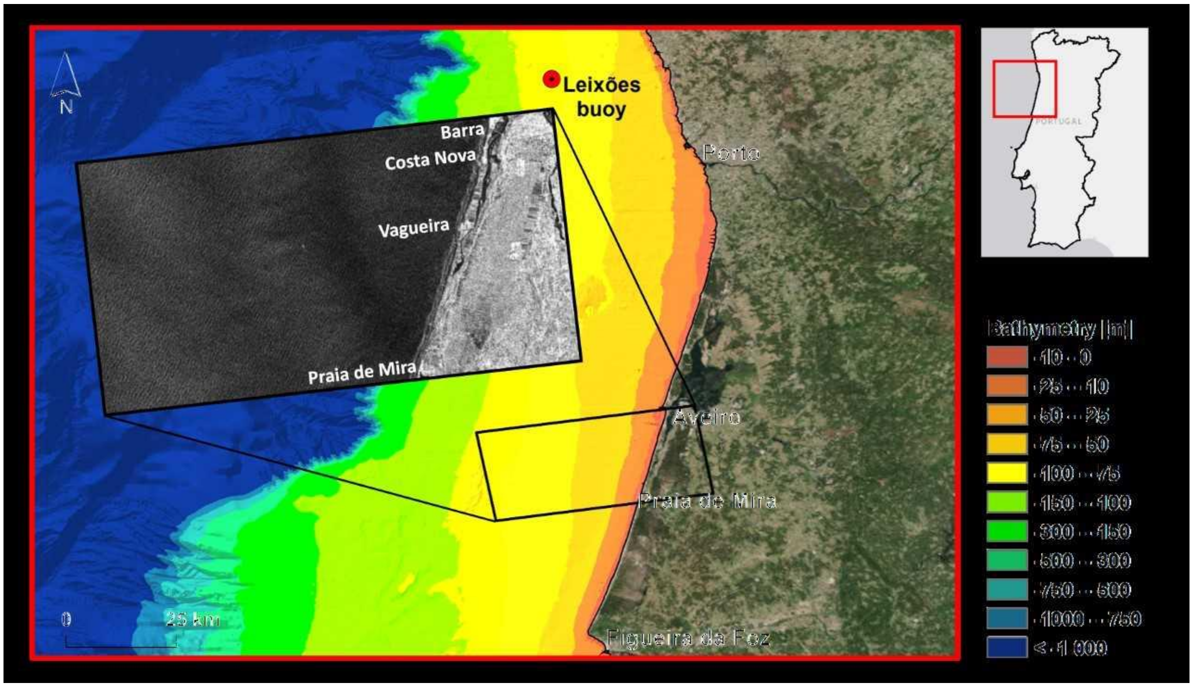

Figure 3-18 - Bathymetry map with the location of the Leixões buoy and the Sentinel-1A sub-image (black rectangle) between Barra and Praia de Mira (W Portugal) (modified from Pereira et al., 2019).

3.4.2 State-of-the-art

Several remote sensing techniques have been proposed to estimate the water depth in the last decades. In the case of optical sensors, there are two main approaches. In the first, available *in situ* data is used to calibrate parameters of an empirical model (Lyzenga et al., 2006; Stumpf et al., 2003) in which each water penetrating spectral band of the optical sensor is used in a linear combination. In the second type of approaches, a radiative transfer model is calibrated by estimating inherent and apparent optical properties of the water column by jointly exploiting water penetrating spectral bands of the sensor. Classical high resolution optical sensors (SPOT-5-6-7, Pleiades, Sentinel-2, Landsat-8, etc.) only offer a few water colour sensitive spectral bands and the radiative transfer model is simplified by considering some water optical properties as constant in the image (for instance bottom albedo and attenuation coefficients) and by empirically calibrating other parameters (for instance water absorption and backscattering). This has led to the development of a Quasi Analytical Algorithm (QAA) to resolve this calibration using water surface reflectance as inputs and water depth as an output (Lee et al., 2002; Capo et al., 2014). For hyperspectral sensors alternative approach to resolve radiative transfer model equations exists (e.g. Dekker et al., 2011), which are more adapted to very heterogeneous bottom conditions. Nevertheless, the utilization of such approach is limited by the water transparency and the variability in the optical properties of the water column and the reflecting bottom material (Adler-Golden et al., 2005). Therefore, its application in high energetic coasts with suspended sediments is restricted to water depths from 0 to 6 m. This limitation motivated the development of alternative methods which are focused on the change of wave properties due to the interaction with sea bottom topography (Brusch et al., 2011). When the waves propagate from deeper to shallower water their wavelength decreases and their direction changes, and as a result these properties allow to infer sea bottom features. Brusch et al. (2011) proposed for the first time, the application of the Fast Fourier Transform (FFT) over Synthetic-Aperture Radar (SAR) image to obtain a directional spectrum and then, to calculate the wavelength and wave direction and to estimate the water depth. These authors worked with SAR data obtained from the commercially available TerraSAR-X (TSX) data. After that, other authors have applied this methodology to SAR data obtained from the RISAT-1 commercial products (Mishra et al., 2014) and Sentinel-1 missions (Wiehle and Pleskachecsky, 2018; Pereira et al., 2019). Pereira et al. (2019) compared the computed with the measured bathymetry to Aveiro coast (W Portugal) and they found the relative error of the water depth varies from 6% to 10%. Alternatively, to the Fast Fourier Transform (FFT), the Wavelet transform (Chui, 1992) is more adequate to represent non-linear wave processes more common in shallow waters and can be used instead to the FFT in this nearshore domain (Abreu et al., submitted).

3.4.3 Algorithm 4a – Empirical model to retrieve bathymetry from HR/VHR optical data

As described above, this approach is based on the combined use of available *in situ* data and water surface reflectance from HR/VHR optical data to calibrate an empirical model for water depth retrieval. The workflow of this approach is described in Figure 3-19 and relies on the so-called Lyzenga algorithm.

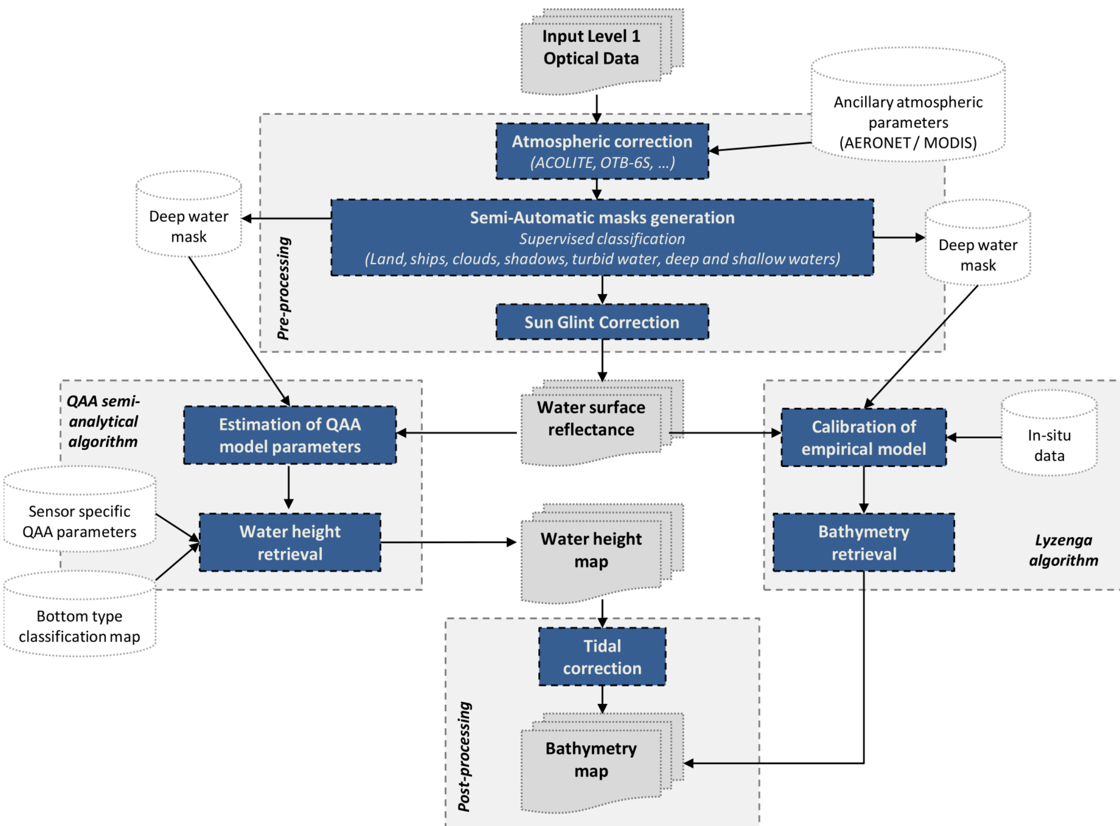

Figure 3-19 - Workflow of the bathymetry retrieval algorithms from HR/VHR optical data.

3.4.3.1 Algorithm description

- *Input data*

Three main input data are needed to perform this approach:

  - Water surface reflectance image obtained after performing three preprocessing steps consisting in (1) atmospheric correction, (2) mask of non-water pixels, (3) sun glint correction,
  - Deep water mask used to calibrate deep water parameters of the empirical model,
  - *In situ* data covering all the depth range and bottom types observed in the area of interest.

- *Algorithms*

Using all the N spectral bands of the water surface reflectance image and *in situ* data as input, the empirical model is calibrated using the following linear combination equation:

- $h = h_0 + \sum_{j=1}^{N} \mathrm{h_j} \ln(R_j - R_{js})$
- where h is the *in situ* depth, R_j and R_{js} are the water surface reflectance and the mean deep water reflectance for the spectral band j and h_0 and h_j are calibration parameters derived from a multilinear regression.

- The bathymetry is retrieved by applying this calibrated equation to the entire water surface reflectance image. Because regression is performed directly on water depth expressed in accordance to a local hydrographic reference level, no tide correction is required.

- *Tools*

Two main software and toolboxes are needed essentially for the pre-processing steps:

  - ACOLITE software for atmospheric correction of Sentinel-2, Landsat-8 and recently Pleiades data
  - OTB toolbox for atmospheric correction of other optical sensor and to perform the supervised classification and mask generation

- *Output product*

The output product is directly a raster file containing bathymetry estimation for each valid water pixels. It can be converted to a xyz file or to iso-contours if requested.

3.4.3.2 Validation

The overall accuracy can reach 0.3 m in shallow waters (Lafon et al. 2014) but it generally increases with depth (Mishra et al., 2004; Hedley et al., 2016) and the mean relative error is usually around 10-20 % of the depth. In the full range of application (0-10m), the overall accuracy is closer to 1 m.

3.4.3.3 Application range and Maturity

This empirical approach has been widely used in past and recent publications (e.g. Mishra et al. 2004; Zoffoli et al. 2014). It is known to retrieve reliable depth range up to 20 m but is more often limited to 10 m (Hedley et al., 2016). This approach suffers also from a few drawbacks. First, it assumes constant water conditions across the area which is of course never a realistic hypothesis even though clear waters can come close to such conditions. Second, it is sensitive to bottom heterogeneity. The more bottom types coexist in the area, the less accurate the results will be. This can be partially improved by calibrating the model for each bottom type assuming that a bottom type map is available. Third, application of this method is restricted to areas where clouds and corresponding shadows do not impact the water surface reflectance. Presence of waves can also be a limiting factor since they can change the water surface reflectance in several ways: (i) the wave-scale water level deformation, (ii) the glint-related wave crest pattern, (iii) wave breaking that cause both sediment resuspension and white foam persistence. While perturbations induced by low-energy waves are usually negligible, this is not the case for intermediate to high-energy waves. Last but not least, it requires *in situ* data.

Nevertheless, this approach is well known and can be easily deployed on many types of optical data. Its maturity can be considered as high.

3.4.4 Algorithm 4b – Quasi-analytical model to retrieve bathymetry from HR/VHR optical data

Contrary to the previous algorithm described in 3.4.3, this approach does not require *in situ* data and is fully based on the description of the physical disturbances endured by the light while it penetrates the water column and is reflected by the bottom. A quasi analytical calibration of the radiative transfer model describing these phenomena is used to retrieve the bathymetry. The workflow of this approach is also described in Figure 3-19 and relies on the so-called QAA semi-analytical algorithm.

3.4.4.1 Algorithm description

- *Input data*

Five main input data are needed to perform this approach:

- Water surface reflectance image (mainly the green band) obtained after performing three pre-processing steps consisting in (1) atmospheric correction, (2) mask of non-water pixels, (3) sun glint correction,
- Deep water mask used to calibrate deep water parameters of the model,

- Pre-calibrated parameters of the QAA algorithm empirically estimated using IOP / AOP databases[1] and spectral sensitivity of the targeted optical sensor,
- Bottom types map and bottom albedo if the targeted sites display heterogeneities,
- Tide level at time of image acquisition to transform water depth into water level in accordance to the hydrographic reference level.

- *Algorithms*

The application of the QAA algorithm follows a four-steps strategy as described in Capo et al. (2014):

- The deep water mask defined during the pre-processing steps is used to estimate the mean deep water subsurface remote sensing reflectance (rrs_{deep}) for the targeted spectral band. The bottom albedo (Rrs_B) is considered as known but if the bottom type is homogeneous (sandy shore for instance), automatic strategies exist to directly infer the albedo from the image.
- From rrs_{deep}, the total absorption and backscattering are estimated followed by the attenuation coefficient Kd in accordance with the equations of the QAA (Lee et al., 2002).
- Then, the water depth h is estimated using the following equation:

$$h = \frac{1}{2K_d}\left[ln\left(\frac{1}{\pi}R_{rs}^{B} - r_{rs}^{deep}\right) - ln\left(r_{rs} - r_{rs}^{deep}\right)\right]$$

- Finally, water depths are converted into bathymetric values using the tide level at the time of image acquisition.

- *Tools*

As previously, two main software and toolboxes are needed essentially for the pre-processing steps:

- ACOLITE software for atmospheric correction of Sentinel-2, Landsat-8 and recently Pleiades data
- OTB toolbox for atmospheric correction of other optical sensor and to perform the supervised classification and mask generation

- *Output product*

The output product is directly a raster file containing bathymetry estimation for each valid water pixels. It can be converted to a xyz file or to iso-contours if requested.

3.4.4.2 Validation

The accuracy is generally poorer than with the empirical approach and RMSE reaches 1.3 m in the study of Capo et al. (2014). Figure 3-20 shows a satellite derived bathymetry produced by i-Sea with image acquired in 2015 on the French Mediterranean coastline using a Pleiades data along with comparison with observations from a LIDAR survey. Results revealed a RMSE of 0,6 m on the entire area and an overall accurate detection of the nearshore sandbar location.

[1] *http://www.ioccg.org/groups/OCAG_data.html*

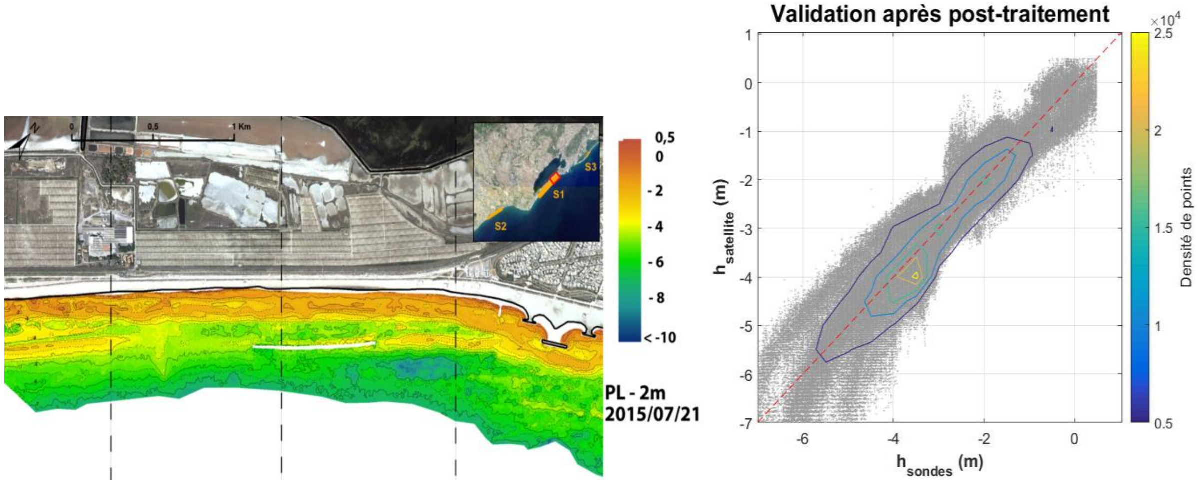

Figure 3-20 - Example of optical satellite derived bathymetry at the Lido de Sète (S France) with a Pléiades image acquired in 2015 and validation results.

3.4.4.3 Application range and Maturity

This QAA approach can retrieve reliable depth up to 10 to 15 m in clear waters with bright sandy substrate. For example, in Capo et al. (2014) study on the French Atlantic sandy coastline, depths of up to 7 m have been retrieved successfully. Similar to the above-mentioned empirical approach, a few drawbacks have to be noted. It also assumes constant water conditions across the area and it is sensitive to bottom heterogeneity. The presence of clouds, shadows and waves can also restrict the method application. Also, because water depths need to be corrected from the tide level, data from tide modes or tide gauges.

Nevertheless, this approach is cost effective and does not require *in situ* data, which are often missing or outdated in many places worldwide. Its maturity can be considered as high.

3.4.5 Algorithm 4c – Bathymetry swell inversion

3.4.5.1 Algorithm description

- *Input data*

HR or VHR Optical or SAR georeferenced images in which swell condition are present (the wave period of the images must be higher than 15 seconds. Eventually if a set of images with a visible swell and good temporal resolution is available, they can be used to produce a merge result. In this case the elapsed time between successive acquisitions must also be considered. In this case the elapsed time between successive acquisitions must also be considered.

Although the offshore wavelength can be computed from the image it is recommended to have access to wave data from a directional wave buoy, for the day of image acquisition, due two main reasons: (1) the image wavelength represent the instant of image acquisition while a time series of a wave buoy represents the mean wave conditions; (2) the image only allow estimate the wavelength while the wave buoy represents the observed offshore wavelength.

The astronomical tidal level for the dates of the image acquisition is also required.

- *Algorithms*

The application of the algorithm follows a four-steps strategy as described in Pereira et al. (2019) and Abreu et al. (submitted):

The first step is the definition of a grid of centre points over the image. These points define the locations in the image where the local (i.e., in the vicinity of each point) estimation of the wave direction and wavelength is carried out. Next, a squared region (image cell) centred in each point of the grid is defined, whose width is specified independently of the grid spacing (in this way, partial superposition between adjacent cells is allowed).

The second step is the spectral analysis, i.e., calculation of the two-dimensional FFT for each defined squared cell, resulting in a two-dimensional frequency-domain representation of the information content of each cell in the image. The FFT represents the energy that a signal shows distributed with respect to the frequency of each of its components, when considering a decomposition of such signal in sinusoidal components. If a signal displays a sinusoidal-like dominant component, this Fourier representation will reveal a high peak of energy at the frequency of such component. Thus, it will be a suitable tool for estimating the characteristics of the dominant sea waves (i.e. wavelength and wave direction) in a specific region. Instead to the FFT the wavelet transform (WT) can be used when the signal displays a non-sinusoidal-like dominant component (more adequate to shallow waters).

The wavelength (λ) (in number of pixels) of the dominant surface wave of that cell can be estimated through (Eq.1):

$$\lambda = 1/ (dx/2M)2 + (dy/2N)2 \quad (1)$$

where *M* is the number of columns of pixels, *N* is the number of rows of pixels, *dx* is the number of columns between two identified peaks in the frequency-domain representation of the cell image and *dy* the respective difference in number of rows.

The value of the wavelength in meters is then obtained from the former by considering the image spatial resolution. The wave direction is the orientation of the segment connecting the two identified sharp peaks.

The wavelengths and wave directions are associated to the coordinates of the centre point of the corresponding cell, in the georeferenced coordinate system provided by the coordinated control points which are attached to the satellite image.
The third step is the bathymetric estimation from linear wave theory. This is an analytical solution of the momentum and mass conservation equations that describe the velocity field and pressure along the water column and establishes a relation between the wave celerity, the frequency and the water depth (linear dispersion relation).

The approach considered for determining the sea-bottom depth (h) satisfies the set of values of the wavelength (λ) and the wavelength at deep water (λ0) given in the linear dispersion relation:

$$\lambda = \lambda 0 \tanh(kh) \qquad (2)$$

where λ0=gT2/2π, T is the wave period, g is the gravity acceleration, k is the wave number and h is the sea-bottom depth. The effect of a mean current was neglected in Eq. (2).

The bathymetry is computed from:

$$h = 2 \operatorname{atanh}(\lambda / \lambda 0) \qquad (3)$$

The last step is the application of low-pass filter to remove the noise in the computed values. This filter has two input parameters: the filter width is the scalar indicative of the width of the filter and the filter sharpness is the scalar indicating how sharp the transition between the pass- and reject-bands is.

- *Tools*

A set of Matlab routines were implemented to address the four-steps strategy as described in Pereira et al., 2019 and Abreu et al., submitted.

- *Output product*

The output product is directly a file containing bathymetry estimation for the domain covered by the linear dispersion relation. The output can be presented in a xyz file or to iso-contours if requested.

3.4.5.2 Validation

The bathymetry computed by means of FFT from satellite SAR images (Sentinel-1) for Aveiro coast were compared with the bathymetry provided by the Oceanographic Observatory of the Iberian Margin (RAIA Observatory). The results disclosed that 20 m estimated isobaths provided the best performance whereas the 30 m estimated isobaths provided the lowest performance. The relative error of the water depth varies between 6% and 10% (Pereira et al., 2019).

The WT was not yet validated.

Figure 3-21 presents the comparison between the ensemble calculated bathymetry with Pereira et al. 2019 method with *in situ* measures. The computed values averages for each cell the results obtained with the four SAR images. Figure 3-22 shows the computed vs. measured dispersion for water depths between 10 and 35 m showing large errors for the higher water depths.

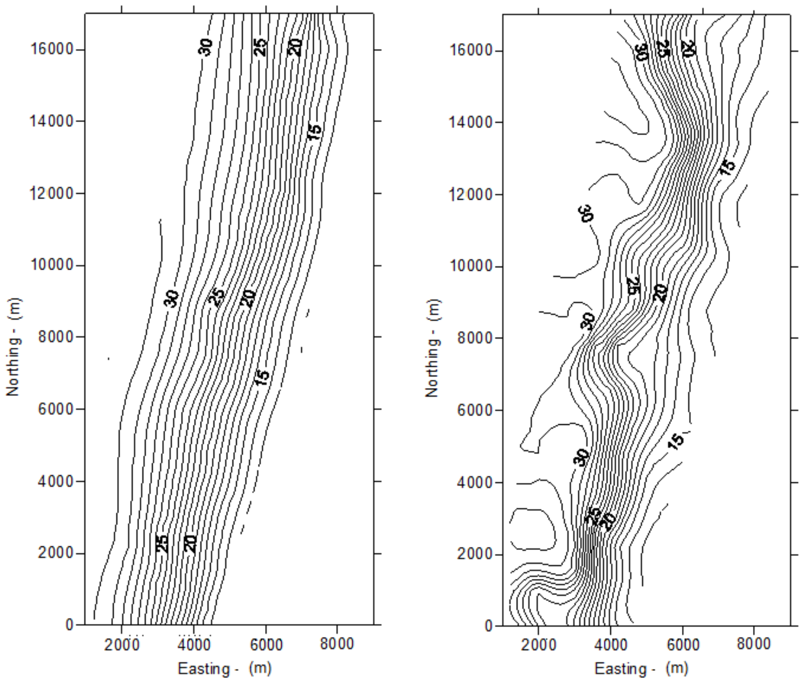

Figure 3-21 - a) Measured bathymetry and b) Ensemble calculated bathymetry near the coast at Aveiro, Portugal. Adapted from Pereira et al. 2019.

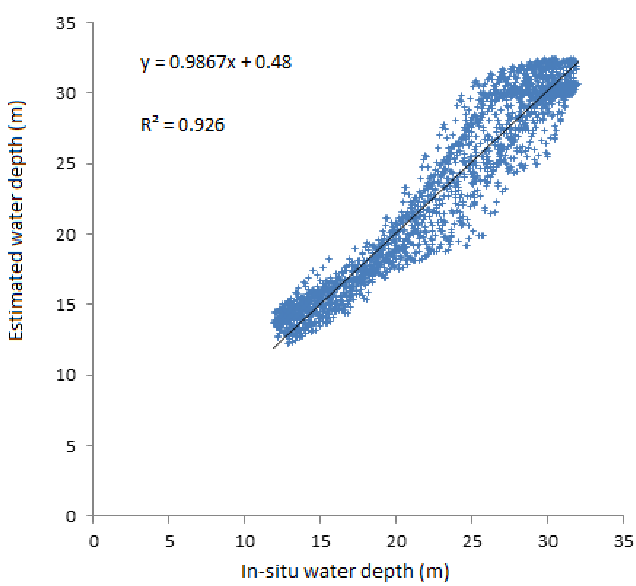

Figure 3-22 - Water depth estimated by FFT methodology vs in situ *bathymetry measurements considering all the points of the interpolated grid. Adapted from Pereira et al. 2019.*

3.4.5.3 Application range and Maturity

The algorithm with FFT that is adequate for water depths between -30 m and -15 m has been tested at Aveiro coast in the images of year 2015 (Pereira et al., 2019). It can be considered as a demonstration algorithm only tested in one test site with a set of four images. The results obtained show that a combined solution that merges the results of all the image set slight improves the results. The relative error of the water depth ranges between 6% and 10% for water depths between 15 and 30 m.

The algorithm with WT that is for water depths between -15 m and -1 m is an experimental only tested over one image in the Aveiro coast. The obtained results allow only infer that it is adequate to estimate the sea-bottom morphology but the accuracy assessment was not performed. It can be considered as an innovative or experimental algorithm.

Both of the algorithms are not suitable for detection of coastal erosion.

3.4.6 References

Abreu, T., Fernández-Fernández, S., Baptista, P., Silva, P.A. *submitted.* Utilização de wavelets para inferir a batimetria a partir de imagens de satélite SAR. In: VIII Tomo da Rede BRASPOR: Saindo da Zona de Conforto: a Interdisciplinaridade das Zonas Costeiras.

Adler-Golden, S.M., Acharya, P.K., Berk, A., Matthew, M.W., Gorodetzky, D., 2005. Remote bathymetry of the littoral zone from AVIRIS, LASH, and QuickBird imagery. IEEE Trans. Geosci. Remote Sens. 43 (2), 337–347.

Brusch, S., Held, P., Lehner, S., Rosenthal, W., Pleskachevsky, A., 2011. Underwater bottom topography in coastal areas from TerraSAR-X data. Int. J. Remote Sens. 32 (16), 4527–4543.

Capo, S., Lubac, B., Marieu, V., Robinet, A., Bru, D., & Bonneton, P. (2014). Assessment of the decadal morphodynamic evolution of a mixed energy inlet using ocean color remote sensing. Ocean Dynamics, 64(10), 1517-1530.

Chui, C.K. 1992. An Introduction to Wavelets, 266p. Academic Press. (ISBN:0-12-174584-8)

Dekker, A. G., Phinn, S. R., Anstee, J., Bissett, P., Brando, V. E., Casey, B., ... & Lynch, M. (2011). Intercomparison of shallow water bathymetry, hydro-optics, and benthos mapping techniques in Australian and Caribbean coastal environments. *Limnology and Oceanography: Methods*, *9*(9), 396-425.

Hedley, J., Roelfsema, C., Chollett, I., Harborne, A., Heron, S., Weeks, S., ... & Ticzon, V. (2016). Remote sensing of coral reefs for monitoring and management: a review. *Remote Sensing*, *8*(2), 118.

Lafon, V., Dehouck, A., Robinet, A., Marieu, V., Curti, C., Durou N., 2014. Détection d'indicateurs géomorphologiques littoraux par télédétection à très haute résolution spatiale (pp. 601-610) - DOI:10.5150/jngcgc.2014.066.

Lee, Z., Carder, K. L., & Arnone, R. A. (2002). Deriving inherent optical properties from water color: a multiband quasi-analytical algorithm for optically deep waters. Applied optics, 41(27), 5755-5772.

Mishra, D., Narumalani, S., Lawson, M., & Rundquist, D. (2004). Bathymetric mapping using IKONOS multispectral data. *GIScience & Remote Sensing*, *41*(4), 301-321.

Mishra, M.K., Ganguly, D., Chauhan, P., Ajai, 2014. Estimation of coastal bathymetry using RISAT-1 C-band microwave SAR data. IEEE Geosci. Remote Sens. Lett. 11 (3), 671–675.

Pereira, P., Baptista, P., Cunha, T., Silva, P.A., Romão, S., Lafon, V., 2019. Estimation of the nearshore bathymetry from high temporal resolution Sentinel-1A C-band SAR data – A case study. Remote Sensing of Environment 223, 199-178.

Stumpf, R. P., Holderied, K., & Sinclair, M. (2003). Determination of water depth with high-resolution satellite imagery over variable bottom types. *Limnology and Oceanography*, *48*(1part2), 547-556

Wiehle, S., Pleskachevsky, A., 2018. Bathymetry derived from Sentinel-1 Synthetic Aperture Radar data. In: 12th European Conference on Synthetic Aperture Radar Electronic Proceedings. Verband der Elektrotechnik Elektronik Informationstechnik e.V. Kartonhulle, Aachen, Germany, 978-3-8007-4636-1, pp. 1489.

Zoffoli, M., Frouin, R., & Kampel, M. (2014). Water column correction for coral reef studies by remote sensing. *Sensors*, *14*(9), 16881-16931.

3.5 Algorithm group 5: Classification methods

3.5.1 Introduction

Classification methods are used to retrieve information about land cover and land use. In order to address Coastal Erosion end-users' requirements, increasing knowledge about land cover and land cover change with time is useful to assess coastal vulnerability and erosion rates. The categorization of the coastal zone according to sediment type and overlaying vegetation, roads and buildings can be done by different classification schemes. The output of the classifications in terms of number of classes and the class types depend on the questions on the one hand and on the spectral and spatial characteristics of the input images on the other hand. Only spectrally distinguishable surface types can be separated in different classes and surface types need to be large enough to be resolvable by the respective pixel size. Land cover classes cover natural and human made surface types. In coastal regions the surface types are very manifold and comprise among others urban areas, rocks, beaches, dunes or wetlands. With respect to coastline indicators, the classifications can be used to identify the edge between two neighboring types of surfaces and can be extracted from the predicted maps.

Classifications are based on various descriptors such as pixel multispectral reflectance and spectral band indices or ratios, but also on textural descriptors. They are chosen, adapted and trained in order to adapt to coastal area diversity and complexity and to the expected number of classes that must be retrieved. One of the Mediterranean POC site shown in Figure 3-23 displays industrialized, urban areas natural areas located along a very narrow sea front suffering from erosion and protected by groins and breakwaters. If needed, some of the classification techniques described hereafter would be relevant to differentiate all land uses and land covers and obtain a continuous and exhaustive shoreline vector for instance.

Different classification methods are introduced: supervised classification scheme and decision trees. Applications to optical and SAR imagery are proposed.

Figure 3-23 - Industrialised and urbanised area experiencing important erosion rates (French Mediterranean coast).

3.5.2 State-of-the-art

Natural ecosystems, beaches, dune systems, intertidal flats together with urban and industrial areas are susceptible to be mapped using high resolution remote sensing imagery. With this respect, multiple approaches are found in the literature (see review by Baghdadi and Zribi, 2016).

For instance, works based on optical and/or SAR satellite remote sensing for the mapping of coastal ecosystems are numerous over temperate and tropical coastal areas, in relation with tidal flats and sediment type mapping (Van der Wal et al. 2007, Gade et al 2008, Brockmann et al 2008), the detection and mapping of intertidal macrofauna e.g. oyster and mussel seabeds (Gade et al., 2014), of intertidal and/or subtidal seagrass habitats (Dekker et al., 2005; Phinn et al., 2008; Barillé et al., 2010, Müller et al. 2016), of coral reefs (Andrefouët et al 2001, Palandro et al, 2008).

Coastal terrestrial landscapes, e.g. coastal dunes, salt marsh habitats and mangroves, have also been addressed over years both by satellite optical-based images or in some cases coupled with SAR images (for salt marshes, refer to Slatton et al. 2008, Dehouck et al., 2012; Van Beijma et al 2014; for mangroves consider Baghdadi & Zribi, 2016; Proisy et al., 2019; for coastal dunes refer to Lafon et al., 2010, 2014 ; for coastal dunes and shingle bars see Roche et al., 2014).

Several remote sensing strategies are possible to perform coastal habitat mapping: mono-date or multi-temporal classification using satellite time series, single source or multi-source optical/ radar data combined in either supervised or non-supervised classification algorithms. Among the most recent and currently used algorithms, we must mention the Support Vector Machines (SVM, Boser et al., 1992), the Multi Layer Perceptron (MLP) and the Random Forest (Pal, 2005; Beguet et al., 2014).

For marine ecosystems mapping (coral reefs, seagrass, sediment), physics-based algorithms based on radiative transfer models like those detailed in Algorithm 4 section are frequently used in shallow and clear waters (e.g. Hedley et al. 2012; Gapper et al., 2018).

Dune foot (limit between dune and beach) can be extracted from a mono-date supervised image classification scheme (Roche et al., 2014), this shows also the good potential of image classification for subaerial feature extraction (section 4.3).

3.5.3 Algorithm 5a – Supervised classification approaches based on optical data

3.5.3.1 Algorithm description

- *Input data*

Single or multiple (in case image timeseries is used) high resolution (HR) or very high resolution (VHR) optical images must be provided to the algorithm. Field observations are usually mandatory to define the typologies present in the image(s) and to create the polygons associated with these typologies. A very good knowledge of the study areas can be sometimes enough.

- *Algorithms*

For many thematic applications, a land use map with a pertinent typology is needed. We developed a full mapping process based on the exploitation of HR and VHR satellite images (such as Pléiades, Sentinel-2, etc.) and latest machine learning approaches such as Deep Learning in order to produce different levels of land use mapping. Our process, described in Figure 3-24, is neither sensor/source dependent neither thematic dependant, it could be applied for many mapping tasks, integrating temporal analysis or multi-source abilities.

The core of our mapping process is the articulation of two main pillars

- First, an iterative discussion with end-users and thematic specialists allows us to define and fine tune the targeted typology according to the potential of available data and image constraints. Field campaign measurement is also discussed, designed and adapted to site specifications or thematic considerations with respect to image sampling constraints. This leads to the elaboration of a pertinent and accurate database.
- Second, we adapt our image analysis and machine learning strategies to the problem, from a pixel wise classification of time series image features with RandomForest when mapping of various vegetation classes is required to convolutional neural network architectures for very high precision mapping of specific objects. Depending of the problematic, we focus more on temporal analysis (vegetation phenology) or on spatial analysis (such as shapes and textures), which allows investigating and optimizing the exploitation of the image potential.

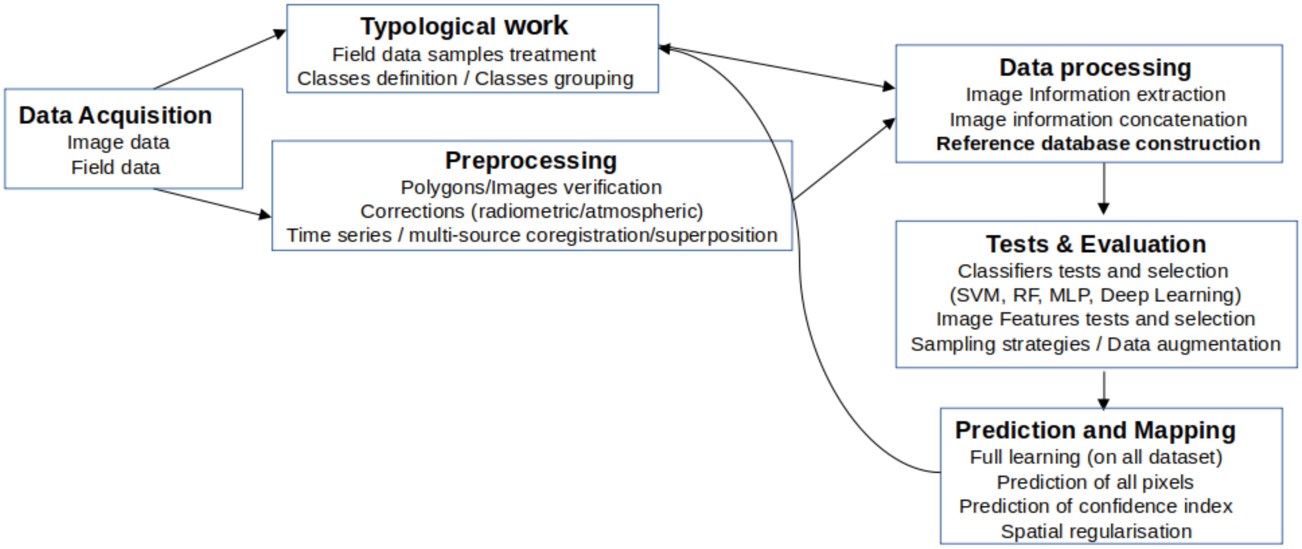

Figure 3-24 - Overview of ISEA's supervised mapping approach

The automatic processing chain is presented Figure 3-24, starting from image and field data acquisition, a workaround typology is needed, based on a cognitive process between thematic experts and image analysis and machine learning experts. This part is very important as it designs the problem and its limits according to the objectives to reach. Images are pre-processed and field data polygons are carefully checked. Images (or image time series) are then used to compute new information such as radiometric or textural indexes (depending on the nature of the problem and the image spectral and spatial resolution) and a reference database is built. The next step consists in testing and optimizing the machine learning process, looking for the best configuration of images features, sampling strategies and classifiers. RandomForest classifier is usually used as a reference, but we also work continuously on DeepLearning architectures and compare performances. We select the best configuration and then apply our modelling to the whole image. A confidence index of the classifier is produced, and a spatial regularization is applied to the classification output (in order to reduce some noise and isolated pixels).

The map produced could be used to extract the borders of classes of interest (e.g. waterline, dune foot, interface between sandy and rocky bottom) or to estimate the distribution area of classes of interest.

- *Tools*

The algorithm uses bash and python programming languages with support of sci-kit learn, Orfeo ToolBox and GDAL libraries.

3.5.3.2 Validation

Our mapping process has been developed and improved during the Biocoast project which aimed to map vegetation types with very precise typologies. Vegetation maps of five different sites in France have been produced with very satisfying results, both in term of spatial precision and typology recognition (an average of 87% of overall accuracy is obtained on the five sites, with an average number of twenty vegetation classes). Figure 3-25 shows a Biocoast map. Since all sites are varying in term of size, needs and problematic, vegetation complexity, the robustness and the reproducibility of our approach has been well proven, with Pléiades and Sentinel-2 like images. On another side, very high precision mapping based on convolutional neural network was applied to seagrass mapping and oyster land mapping with impressive results (compares to manual digitization). To resume, we have a wide range of tools based on the latest advances in remote sensing and machine learning combined with a great experience in terms of use and adaptation of these methods to a specific problem.

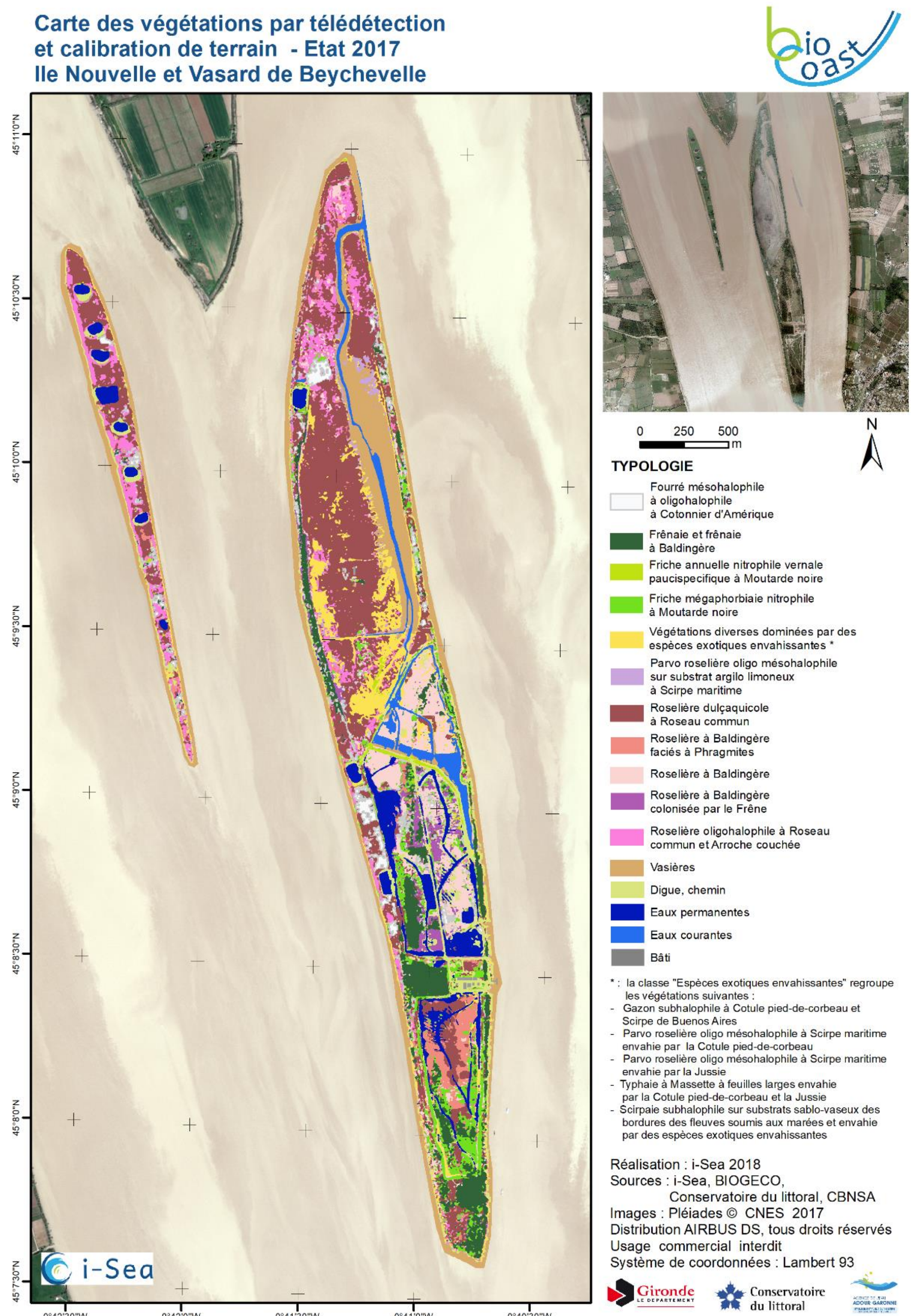

Figure 3-25 - Vegetation map of Ile Nouvelle and Vasard de Beychevelle site produced by BIOCOAST mapping process on a Pléiades time series (2-m spatial resolution).

3.5.3.3 Application range and Maturity

Our mapping process is very mature and has been applied in many circumstances for different applications of land use thematic. Obviously, as any other optical based remote sensing, clouds are a strong limit. But in a context of temporal series, temporal gap filling techniques can be applied to avoid this issue. Working with VHR and HR is almost the same, the main difference could be the use of textural information when the spatial resolution is significantly smaller than the size of the objects of interest. Also, the precision level of the targeted typology with VHR data cannot be the same as the one used for HR. With less spatial precision, the typology needs to be simplified. Classes such as dry and wet sand, mud, sea-grass and rocks are able to be mapped from HR and VHR optical remote sensing.

For the classification of underwater habitats, we have less maturity about the precision and performance we could reach. The quality of the images (and atmospheric conditions), the state of the water surface (glint presence) and its depth, the presence of turbidity are the most influent factors on underwater visibility. We succeed to produce some very accurate map on well controlled cases, like sea-grass mapping from Sentinel-2 data. But we miss the experiences of a range of possible cases of application. We assume that in most cases, we should be able to distinguish sand, rocks and vegetated habitats underwater. The accuracy is still undetermined, we will need reference data on different sites to estimate it rigorously case by case.

3.5.4 Algorithm 5b – Classification based on texture information derived from SAR amplitude data

The lack of spectral information in SAR imagery makes necessary the use of texture information. Classical texture statistics are used as pixel features to discriminate changes on materials on scene.

3.5.4.1 Algorithm description

As texture metrics, occurrence metrics (range, mean, variance, entropy and skewness) (Anys et al., 1994) and co-occurrence metrics (mean, variance, homogeneity, contrast, dissimilarity, entropy, second moment and correlation) (Haralick et al., 1973) are proposed.

Once texture metrics are obtained, different standard classification methods are proposed (maximum likelihood (Richards, 1999), neural network (Richards, 1999; Rumelhart and McClelland, 1987) and support vector machine (Chang and Lin, 2011; Hsu et al., 2010; Wu et al., 2004) to classify texture information.

- *Input data*
    - *SAR amplitude image*
- *Algorithms*
    - *Maximum likelihood*
    - *Support vector machine*
    - *Neural network*
- *Tools*
    - *ENVI*
- *Output product*
    - *Classification raster in TIFF format*

3.5.4.2 Validation

The texture metrics and classification algorithms have been used by the scientific community for years inside ENVI software. Some cases of use in the context of SAR data from a coastal area can be found in (Fonteh et al., 2016) (Zakeri et al., 2017) (Abdikan et al., 2016).

3.5.4.3 Application range and Maturity

These texture metrics and classification algorithms have been implemented in COTS ENVI for several years and are considered mature. They can be applied to any kind of land use problem, not only to coastal areas as it can be seen in (Heumann, 2011) where these classification algorithms are used for mangrove classification, and (Luo, et al., 2019) where it is used to classify mine landslide.

Classification result will depend on training data. A good selection of training data will allow to create a good model for the classes. This means to avoid selecting, as training data, pixels where a mixture of different classes may be contained.

3.5.5 Algorithm 5c – Decision tree classification based on band ratios and LSU (BC)

3.5.5.1 Algorithm description

The classification of optical data for intertidal habitats and sediment distribution is based on a number of different decision trees. Dedicated decision trees are in place that focus on specific aspects of the intertidal flat areas, such as seagrass meadows and mussle beds, sediment distribution or the distribution of sediment and water areas, including remaining water ponds on the sediment surfaces. These decision trees, which use well defined features derived from optical data, will be used to characterize the intertidal habitats and their changes, in particular the morphological changes of intertidal creeks.

- *Input data*

Each classification is based on a single acquisition of optical high resolution data from sensors onboard of Landsat-5, Landsat-8, Sentinel-2, SPOT-5,-6,-7, RapidEye. In order to detect the morphological characteristics and changes a long time series of classifications is required. The longest time series is available for Landsat series, starting with Landsat-5 MS, Landsat-8 ETM (1999-2003), Landsat-8 since 2013. Data availability is limited due to low tide constraints, but it has improved since the launch of Sentinel-2; having both – Landsat-8 OLI and Sentinel-2 MSI in parallel since 2015 and even with MSI-B since 2017. Until now, the intertidal flat classifications have been mainly applied to freely available data.

- *Algorithms*

A classification framework has been developed together with national park authorities to classify the intertidal flat areas of the Wadden Sea. The classification is based on a knowledge-based decision trees using different band combinations and linear spectral unmixing abundances (Müller et al., 2016). Examples of different decision trees are given in Figure 3-26. For this specific product, the discrimination between sediment areas and tidal creeks (water) is needed. It also provides shallow water areas on the tidal flats (remaining water in depressions). Especially the shift of the tidal creeks and sediment flats is needed for assessing erosion processes in the Wadden Sea. Finally, the classification results are overlaid in order to visualise the shift of tidal creeks (Figure 3-28).

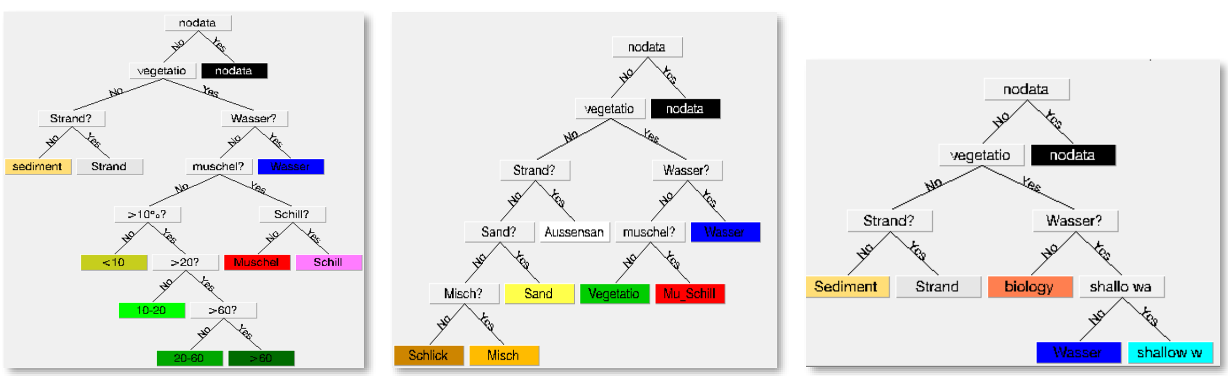

Figure 3-26 -Examples of different decision trees for retrieving intertidal flat habitats and sediment distributions

- *Tools*

SNAP and ENVI

- *Output product*

The output are classification results in raster format. They are overlaid for analysing the tidal creek changes. The products are used the assessment of erosion in the German Wadden Sea Test Sites (North Sea).

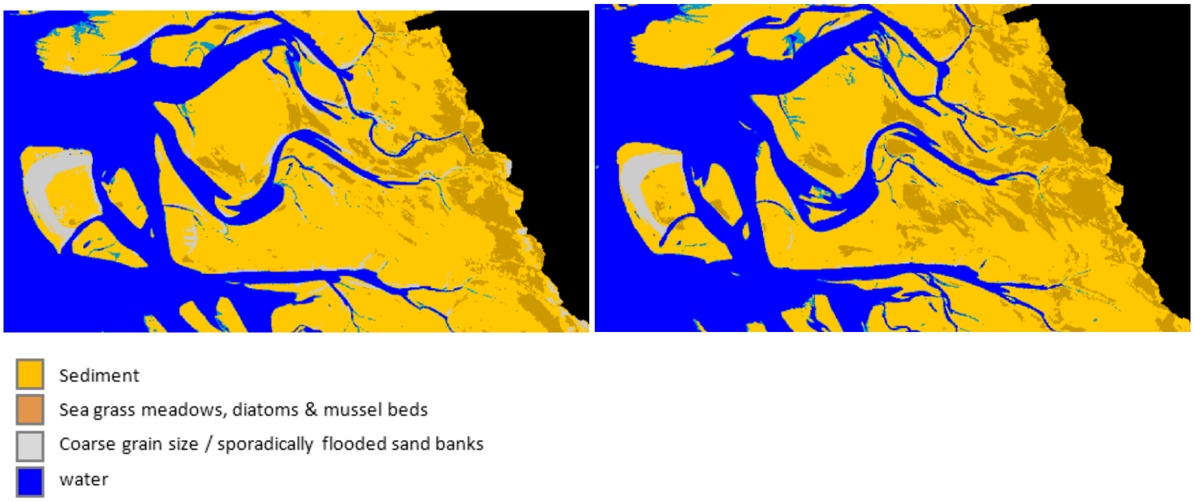

Figure 3-27 - Classification of sediment flats and tidal creeks in 2015 (left) and 2016 (right

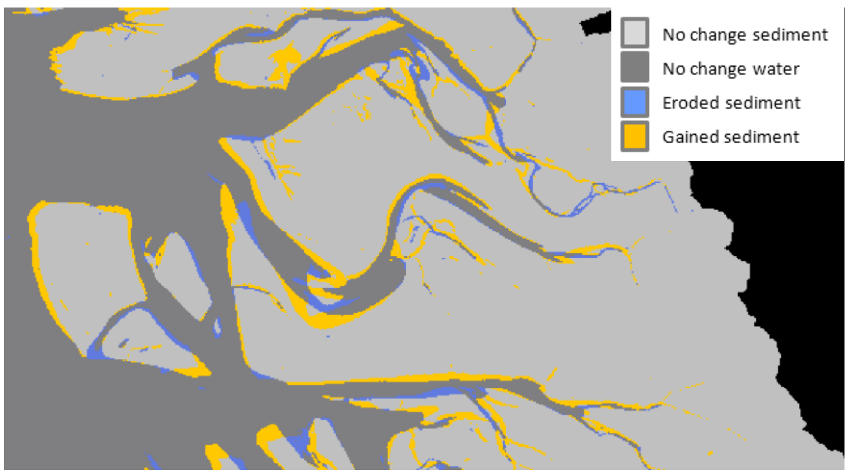

Figure 3-28: changes of tidal creek positions between 2015 and 2016

3.5.5.2 Validation

The classification of intertidal flat habitats, which is the basis of this application, has been validated in terms of sediment type and seagrass beds (Müller et al. 2016). However, the transition between water and land has only be validated against the original images, as the water level changes too fast due to tidal effects and cannot be evaluated in the field.

3.5.5.3 Application range and Maturity

The method is strongly depending on the tidal phase and weather conditions during the images acquisition. Therefore, several images need to be analysed per period in order to get a representative distribution of the tidal creeks. Cloud free conditions and low tide are pre-conditions for good images and reduce the availability of suitable images. The situation has been improved since the launch of Sentinel-2.

The outcome, which needs to be applied to a longer time series will be used to observe the direction morphology changes and if creeks are approaching coastal areas or if large tidal basins undergo main changes (e.g. connection of tidal basins by tidal creek changes or break throughs. The identification of the trend is in focus for assessing the influence on coastal erosion. The more images are included, the better the expected results. As the water level is very variable, it needs to be demonstrated that the trend is still detectable. The accuracy of the trend detection will be very much influenced by the availability of suitable low tide images.

3.5.6 References

Abdikan S., Sanli F.B., Ustuner M., Calo F. "Land cover mapping using Sentinel-1 data" The International Archives of the Photogrammetry, Remote Sensing and Spatial Information Sciences, Volume XLI-B7, 2016

Anys, H., A. Bannari, D. C. He, and D. Morin. "Texture analysis for the mapping of urban areas using airborne MEIS-II images." Proceedings of the First International Airborne Remote Sensing Conference and Exhibition 3 (1994): 231-245.

Baghdadi, N, Zribi, M, 2016. Land Surface Remote Sensing in Urban and Coastal Areas, 1st Edition, ISTE Press – Elsevier, 392 p.

Barillé L., Robin M., Harin N., Bargain A., Launeau P. (2010). Increase in seagrass distribution at Bourgneuf Bay (France) detected by spatial remote sensing, Aquatic Botany, 92, 185-194.

Beguet, B., Guyon, D., Boukir, S., Chehata, N., 2014, Classification of forest structure using Very High Resolution Pléiades image texture, IEE IGARSS, 13-18 July, Québec, Canada.

Boser, B.E., Guyon, I.M., Vapnik, V.N, 1992. A Training Algorithm for Optimal Margin Classifiers. In Fifth Annual Workshop on Computational Learning Theory, pages 144--152, Pittsburgh, ACM.

Brockmann, C., and K. Stelzer (2008). "Optical Remote Sensing of Intertidal Flats", in "Remote Sensing of the European Seas", V. Barale and M. Gade (Eds.), Springer, Heidelberg, pp. 117-128.

Chang, C.-C., Lin., C.-J., 2011. LIBSVM: a library for support vector machines. ACM Transactions on Intelligent Systems and Technology 2, 27:1-27:27. Software available at http://www.csie.ntu.edu.tw/~cjlin/libsvm.

Dehouck A., Lafon V., Baghdadi N., Marieu V. (2012). Use of optical and radar data in seanergy for mapping intertidal flats and coastal salt marshes (Arcachon lagoon, France), Geoscience and Remote Sensing Symposium (IGARSS), 2012 IEEE Internationa, 2853-2856.

Dekker A., Brando V.E., Anstee J.M. (2005). Retrospective seagrass change detection in a shallow coastal tidal Australian lake. Remote Sensing of Environment, 97, 415-433

Fonteh M.L., Theophile F., Cornelius M.L., Main R, Ramoelo A., Cho M.A. "Assessing the Utility of Sentinel-1 C Band Synthetic Aperture Radar Imagery for Land Use Land Cover Classification in a Tropical Coastal Systems When Compared with Landsat 8" JGIS Vol.8 No.4, August 2016

Gade M., Melchionna S., Stelzer K., Kohlus J. (2014). Multi-frequency SAR data helps the monitoring of intertidal flats on the German North Sea coast. Estuarine, Coastal and Shelf Science

Gapper, J.J., El-Askary, H., Linstead, E., Piechota, T., 2018. Evaluation of Spatial Generalization Characteristics of a Robust Classifier as Applied to Coral Reef Habitats in Remote Islands of the Pacific Ocean. Remote Sensing, 10, 1774; doi:10.3390/rs10111774.

Haralick, R., Shanmugan, K., and Dinstein, I. "Textural Features for Image Classification." IEEE Transactions on Systems, Man, and Cybernetics 3, no. 6 (1973): 610-621.

Hedley J., Roelfsema C., Koetz B., Phinn S. (2012). Capability of the Sentinel-2 mission for tropical coral reef mapping and coral bleaching detection. Remote Sensing of Environment, 120, 145-156.

Hsu, C.-W., C.-C. Chang, and C.-J. Lin. (2010). A practical guide to support vector classification. National Taiwan University. http://www.csie.ntu.edu.tw/~cjlin/papers/guide/guide.pdf. Lafon V., Hoareau A., Mallet C., Desprats J.-F., (2010). Suivi du trait de côte en Aquitaine par imagerie Formosat-2. Actes des 11èmes Journées Nationales Génie Côtier Génie Civil, 497-504 (in french)

Heumann, B. W. (2011) An Object-Based Classification of Mangroves Using a Hybrid Decision Tree—Support Vector Machine Approach. Remote Sens.2011, 3, 2440-2460; doi:10.3390/rs3112440

Lafon V., Dehouck A., Robinet A., Marieu V., Curti C., Durou N. (2014). Détection d'indicateurs géomorphologiques littoraux par télédétection à très haute résolution spatiale. Actes des 13èmes Journées Nationales Génie Côtier Génie Civil, 601-610 (in french).

Luo X, Lin F, Zhu S, Yu M, Zhang Z, Meng L, et al. (2019) Mine landslide susceptibility assessment using IVM, ANN and SVM models considering the contribution of affecting factors. PLoS ONE 14(4): e0215134. https://doi.org/10.1371/journal.pone.0215134

Müller, G, Stelzer, K., Smollich, S., Gade, M., Adolph, W., Melchionna, S., Kemme, L., Geissler, J., Millat, G., Reimers, G., Kohlus, J., Eskildsen, K. (2016): Remotely sensing the German Wadden Sea – a new approach to address national and international environmental legislation. Environmental Monitoring and Assessment, 188(10), 1-17; DOI 10.1007/s10661-016-5591-x

Pal, M., 2005. Random forest classifier for remote sensing classification. International Journal of Remote Sensing, 26(1), 217–222.

Palandro D.A., Andréfouet S., Hu C. Hallock P., Muller-Karger F., Callahan M.K., Kranenburg C., Beaver C.R. (2008). Quantification of two decades of coral reef habitat decline in the Florida Keys National Marine Sanctuary suing Ladnsat aata (1984-2002). Remote sensing of Environment, 112, 3388-3399.

Phinn S., Roelfsema C., Dekker A., Bando V., Anstee J. (2008). Mapping seagrass species, cover and biomass in shallow waters : an assessment of satellite multi-spectral and airborne hyperspectral imaging systems in Moreton Bay (Asutrsalia). Remote Sensing of Environment, 112, 3413-3425.

Proisy, C., Ghosh, S., Muthusankar, G., Helfer, V., Carle, J., Hassenrück, C., James, R.A., Lakshumanan, C., Narendran, R., Kathiresan, K., Usha, T., Madeswaran, P., 2019. Fine-scale assessment of changes in zonations of species for the management of imperiled mangroves, Pichavaram, India. Proceedings of Mangrove Macrobenthos & Management 2019, 1-5 july 2019, Joyden Hall, Singapore.

Richards, J. Remote Sensing Digital Image Analysis, Berlin: Springer-Verlag (1999), 240 pp.

Roche A., Bosc C., Chandelier L., Lagnous R. (2014). Apport de l'imagerie satellitaire pour le suivi du trait de côte, Actes des 13èmes Journées Nationales Génie Côtier Génie Civil, 621-628 (in french)

Rumelhart, D., and J. McClelland. "Learning Internal Representation by Error Propagation" in Parallel Distributed Processing, Vol. 1, edited by Rumelhart, Hinton, and Williams, MIT Press (1987).

Slatton K.C., Crawford M.M., Chang L-D. (2008). Modeling temporal variations in multipolarized radar scattering from intertidal coastal wetlands, ISPRS Journal of Photogrammetry and Remote Sensing, 63, 559-577.

Van Beijma S., Comber A., Lamb A. (2014). Random forest classification of salt marsh vegetation habitats using quad-polarimetric airborne SAR, elevation and optical RS data. Remote sensing of Environment 149, 118-129

Van der Wal D., Herman P.M.J (2007). Regression-based synergy of optical, shortwave infrared and microwave remote sensing for monitoring the grain-size of intertidal sediments, Remote Sensing of Environment, 111, 89-106.

Wu, T.-F., C.-J. Lin, and R. C. Weng. (2004). Probability estimates for multi-class classification by pairwise coupling. Journal of Machine Learning Research, 5:975-1005, http://www.csie.ntu.edu.tw/~cjlin/papers/svmprob/svmprob.pdf.

Zakeri H., Yamazaki F., Liu W. "Texture Analysis and Land Cover Classification of Tehran Using Polarimetric Synthetic Aperture Radar Imagery" Appl. Sci. 2017, 7, 452

3.6 Algorithm group 6: Extraction of submerged morphological structures and changes

3.6.1 Introduction

Coastal areas, especially beaches, are more and more threatened by the complex effects of climate change, which induces stresses such as increased storminess and overall more frequent extreme events. These can lead to pressures that can take the form of increased erosion or modification of the maximum run-up limit. Since nearshore sandbars represent a natural defence system against these phenomena, monitoring the dynamics and behaviour of such morphological features can help coastal managers better prepare for coastal protection actions.

3.6.2 State-of-the-art

Various methods were widely used for the quantification of sandbar crest positions, ranging from seasonal and annual echo-sounder data to LiDAR surveys, X-band radar images, photographic and satellite imagery and video techniques (Roman-Rivera and Ellis, 2019).

However, applications of satellite imagery to date have been mainly restricted to nearshore satellite-derived bathymetry, which can be further used to derive the locations of sandbars. Nevertheless, there are situations when a good quality bathymetry is not possible to be obtained (such as areas with moderate to high turbidity), but it is still possible to extract the positions of the sandbars. Therefore, dedicated approaches are required. A recent study of Athanasiou et al. (2018) discussed the suitability of using the Landsat 5, 7, 8 and Sentinel-2 satellite images for sandbar locations manual (visual) extraction in order to investigate decadal scale crescentic sandbar dynamics at Anmok beach in South Korea. To our knowledge, in exception to this work, there is no other study to date dealing with sandbar crest positions extraction (either manual or automatic) and analysis using high to moderate satellite images.

3.6.3 Algorithm 6a – Submerged sand banks

3.6.3.1 Algorithm description

The algorithm is used to extract each submerged sandbar position using perpendicular profiles along the shoreline, based on multispectral satellite imagery (Tatui and Constantin, in review). There are two distinct mechanisms (determined by the wave regime) that can be used to detect the position of a sandbar using a satellite image. The first one relies on a relative bathymetric estimation (not absolute values of water depth). This approach yields good results in case of low wave energy. In other situations, wave breaking occurs in the proximity of the shore, when the wave breaks on sandbars crest. It therefore creates a foam layer on the surface of the water, with very high reflectance response compared to the surrounding water. The maximum reflectance intensity of this foam region corresponds to the sandbar crest position (similar to video techniques). For these two scenarios, even if the observed object/phenomenon is different, it refers to the same morphometric features and the methodology relies on the same principle: reflectance spectrum is amplified over the areas where the sandbars are located.

- *Input data*

The input data is represented by high to medium resolution multispectral satellite imagery. Visible and infrared (NIR or SWIR) wavelengths are required. The algorithm was tested on Sentine-2 data. Higher resolution images are expected to yield same quality results and even better.

- *Algorithms*

Several imagery pre-processing steps are required before the sandbar extraction can be performed, such as: scene cropping, resampling, masking areas that are not covered by water or combining the spectral bands from the visible domain, as to augment the increases in spectral response over the sandbar.

The procedure for sandbars extraction follows several steps, which are detailed hereafter:

1. A network of profiles, perpendicular to the shoreline is created.
2. Along each profile, the satellite combined reflectance values are extracted.
3. An exponential model is fitted to the graph of each profile perpendicular to the shoreline.
4. A normalisation of the profile is performed, by subtracting the model from the original data vector.
5. Using a moving window with a dimension, the maximum value within that region is computed. If the centre of the moving window corresponds with the identified maximum value, the position is qualified as a possible crest sandbar position. Also, if all the values within that moving window have a low standard deviation, then the point is not taken into consideration. Next, a supplementary filtration is performed, by removing points below the mean value of the positive numbers of the profile.
6. The final step is to compute a distance matrix between all points. Only those that have a neighbour closer than a specific distance are kept. Since the features that we hunt for are linear ones, occasional presence of just one point in space is considered not enough as to represent a sandbar.

- *Tools*

In order to implement the methodology, the following software and libraries were used: Geospatial Data Abstraction Library (GDAL) for satellite data pre-processing; R for the sandbar extraction.

- *Output Products*

Figure below presents the sandbar position extracted from a Sentinel-2 image over different moments in time.

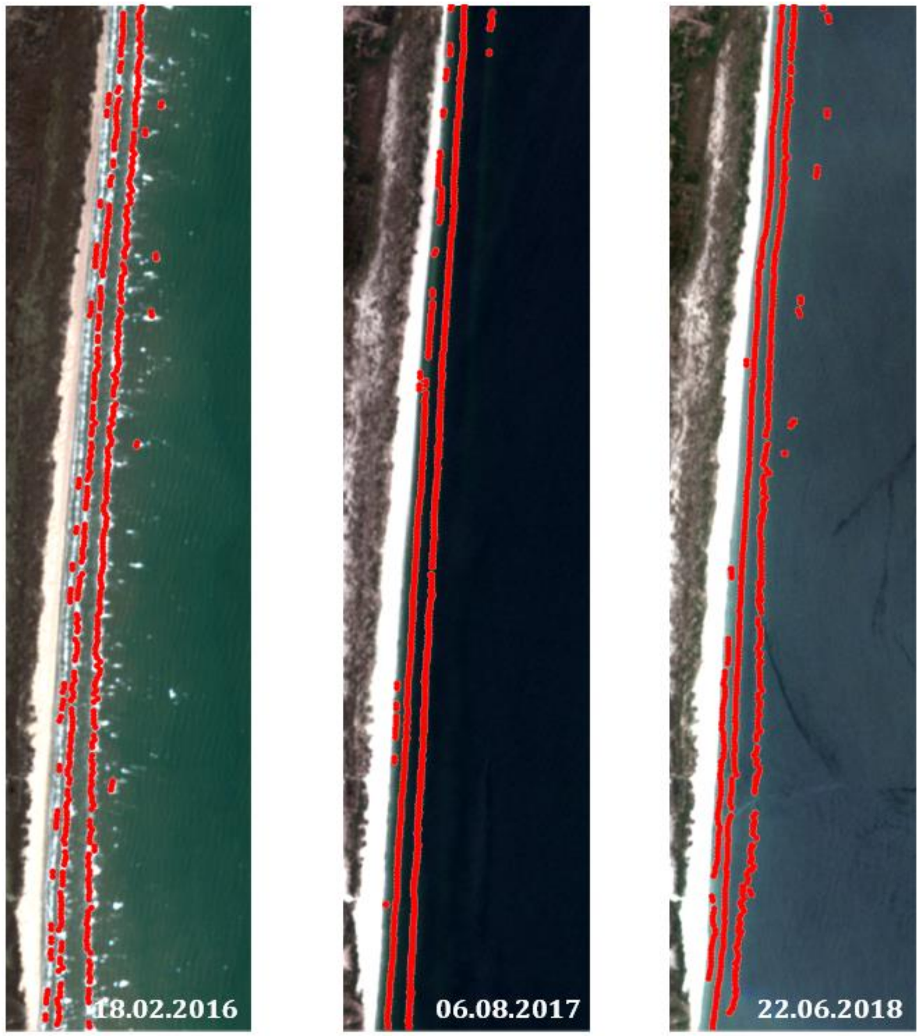

Figure 3-29 - Sandbar position extracted from a Sentinel-2 image over different moments in time

3.6.3.2 Validation

Validation activities consists of comparing the distance from shore (m) extracted from Sentinel-2 compared with distance from shore (m) determined from bathymetric measurements. The result of validation work performed for multiple match-up pairs are shown in the following figure. Using the Sentinel-2 images the mean error (bias) in the cross-shore distance from the shoreline is of 6.2 m with a median error decreasing to 5.4 m and a mean relative error of approximately 6%. However, the use of higher-resolution images such as those acquired by Pléaides 1 may results in lower detection errors (higher accuracy).

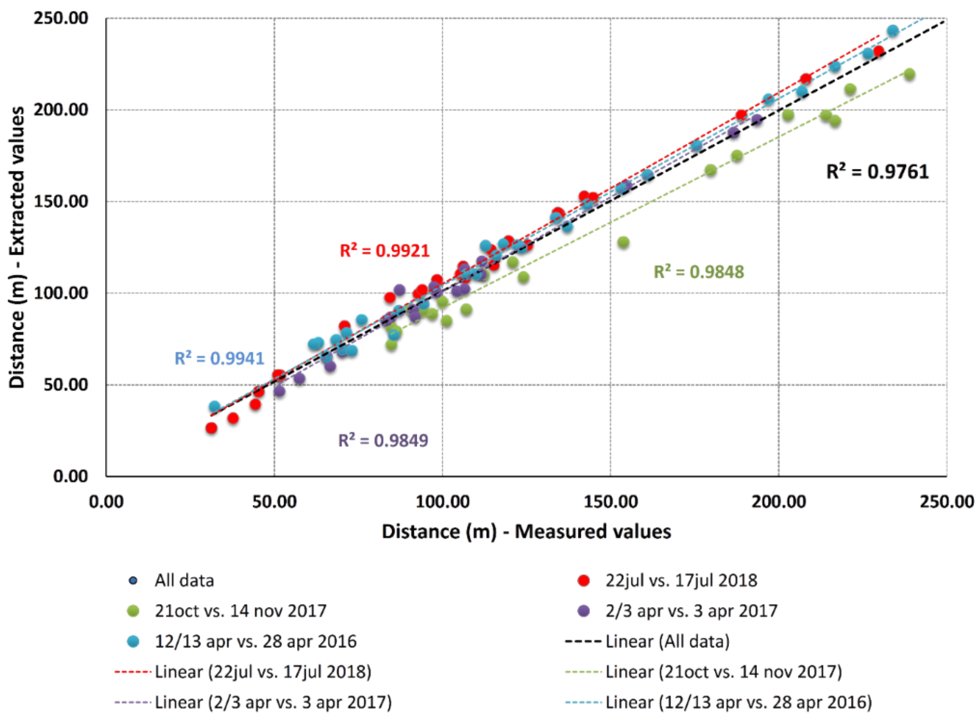

Figure 3-30 – Match-up Analysis for distance of shore between DEM and derived sand banks

3.6.3.3 Application range and Maturity

The algorithm is developed using the new and innovative approach based on the combined reflectance of the submerged sand bars in the visible spectrum. The method has been applied on cloud free Sentinel-2 images from all seasons, covering various wave conditions, offered solid results. The area of interest is represented by the coastal area of Danube Delta, between Sfantu Gheorghe and Sulina.

The algorithm was tested on more than 3 years of satellite data and was validated using consistent *in situ* measurements. The maturity of implementation allows replication in other areas and using other satellite data types.

3.6.4 Algorithm 6b – Mapping change of sandbars

3.6.4.1 Algorithm description

- *Input data*

Sentinel-2 10m visible bands

- *Algorithms*

This simple algorithm is based on the interpretation of RGB images and on the extraction of transects across the sand bank ripples. The transects are extracted either from one band or from indices of bands that highlight the difference in colour of sand bank ripples and sand bank valleys. Best suited band combination seems to be the peak height of B3 (green band).

The first step is to produce RGB images of cloudfree Sentinel-2 images for all available years and generate an animated GIF from them. This small movie shows if sand banks are stable in their position or if they change over time.

The second step is to define a suitable transect position that is perpendicular to the ripples and to extract the values of Band 2, 3 and 4 of cloudfree Sentinel-2 images. The peak height of B3 is calculated from the three visible 10m bands. The values are visualized in transect plots. The position of relative max and min show if the positions of ripples are changing across the different acquisitions.

$$Peak\ height\ B3 = (B3 - B2 - (B4 - B2) * (0.561\ -\ 0.482/0.654 - 0.482)) * 100$$

The absolute height of the maxima / minima is not of main interest, but their positions.

- *Tools*

SNAP (or any other EO image software) and excel/python for plotting

- *Output data*

Time series of RGB images and resulting animated GIFs and Transect plots.

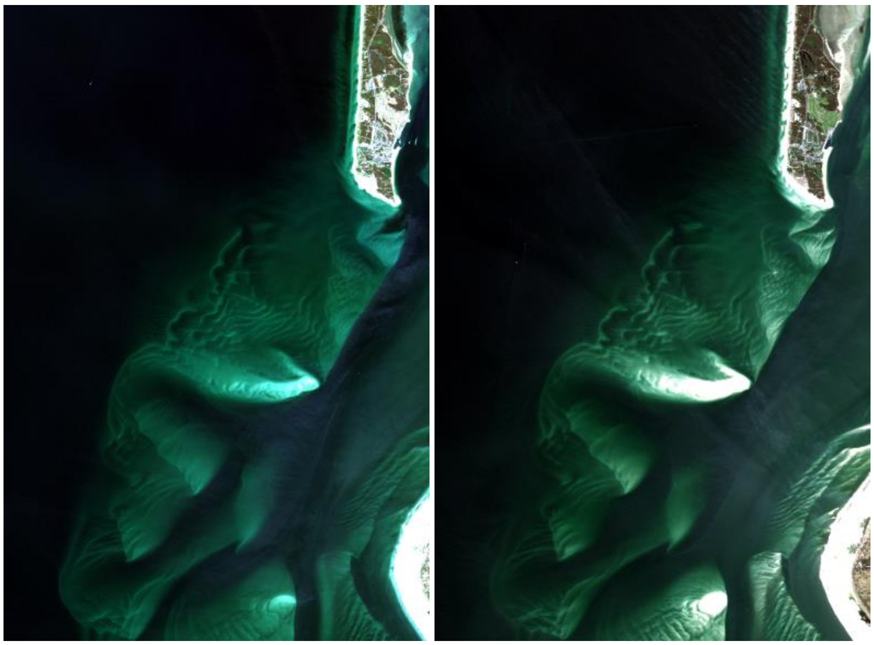

Figure 3-31 – RGB of underwater sand banks south of Sylt Odde from 2 different Sentinel-2 acquisitions

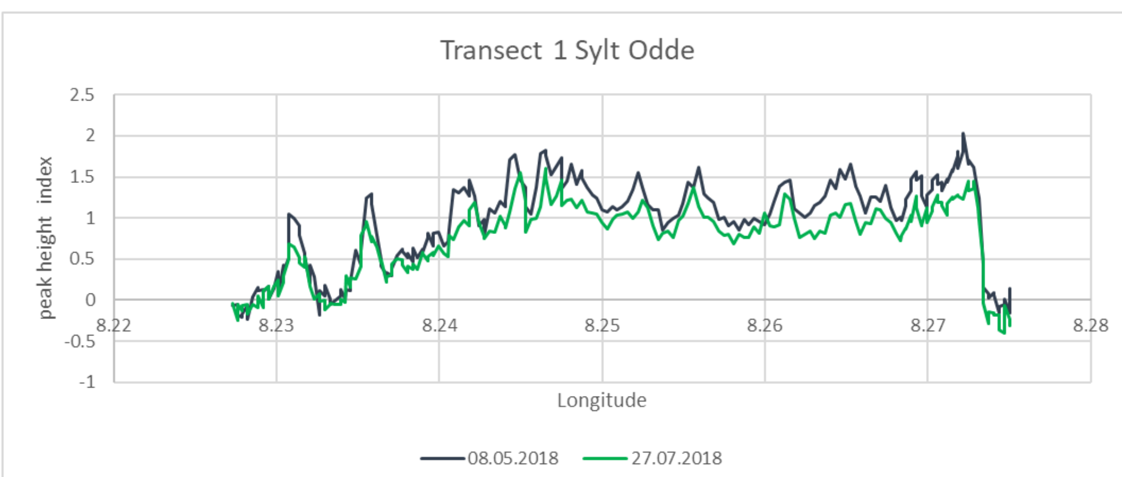

Figure 3-32: Transect plot of the peak height index for two different Sentinel-2 acquisitions

3.6.4.2 Validation

This method has not yet been validated. It will be compared with Laser bathymetry products provided by the user.

3.6.4.3 Application range and Maturity

This algorithm has not yet been applied but are requested by the users and will be tested during the POC. This algorithm is currently for local application. It can be applied to a long time series by automated extraction of the transects but in order to be sure that the images are suitable, a visual inspection is needed.

3.6.5 References

Athanasiou, P., de Boer, W., Yoo, J., Ranasinghe, R., Reniers, A. (2018). Analysing decadal-scale crescentic bar dynamics using satellite imagery: A case study at Anmok beach, South Korea. Mar. Geol. 405. https://doi.org/10.1016/j.margeo.2018.07.013

Roman-Rivera, M.A. & Ellis, J.T. (2019). A synthetic review of remote sensing applications to detect nearshore bars. Marine Geology, 408, p. 144-153

Tatui, F. & Constantin, S., in review. Nearshore sandbar crest position dynamics analysed based on Earth Observation data

4 ALIGNMENT WITH END-USER REQUIREMENTS AND ALGORITHM SELECTION

4.1 Introduction

Here we assess how the algorithms proposed in Chapter 3 fit with the requirements expressed by the end-user enrolled in the Space for Shore community. This chapter is made several sections; one section per indicator recalled in Table 2-1 in Chapter 2. For every indicator, the end-user requirements – summarized in the Requirements Baseline document – are here exhaustively listed (in one Table per indicator) and the corresponding algorithms proposed by the consortium partners in Chapter 3 are remined.

Finally, a short discussion about the capacity of the different algorithms to fulfil the requirements (mainly accuracy and production frequency) is engaged. This leads to the identification of the best combination of algorithms with EO data for every indicator and every POC site, except when it is impossible to fit the requirements.

Independent of individual algorithms or products, EO data come with certain constrains which are summarized in chapter 4.2. They apply to all EO-based products.

The tables given in Section 4.3 to Section 4.13 (one table per indicator) provide the compilation of requirements we have to address and proposed algorithm/data. When no requirement was provided by end-users for a parameter this is indicated by the symbol ng (= not given) and a suggestion for this parameter is made in parentheses following the symbol; suggestion is based on requirements from neighbouring sites or sites from other coastal region with similar environmental settings. The table also includes algorithm and EO data resolution that fulfil the end-user requirements. See Table 4-1 for the spatial resolution of optical sensors and Table 4-2 for SAR sensors corresponding to annotated EO data resolution.

Even if not requested by end-users, production of some coastal erosion indicator for long-term monitoring at some specific POC sites is envisaged. This will be done for sites where coastal erosion dynamics are large enough with respect to (i) the spatial resolution of the EO data from ESA and other open archives used in the algorithms and (ii) a targeted 25-yr period toward the past. The resolution of these EO data generally ranges from 10 to 30 m that makes almost impossible to detect any coastal change signal at sites where spatial change rate are approximately below 0.4 to 1.2 m/yr, respectively.

4.2 Common considerations

4.2.1 Geo-referencing accuracy and implication

Raw optical and SAR EO data acquired by satellite-borne sensors are usually automatically georeferenced by satellite image providers using complex processing chain. These processing chain ensure that at global scale the georeferencing is of very high quality. However, at local scale some discrepancies can be observed with georeferencing errors of the order of the pixel resolution (Gascon et al., 2017[2]; Yan et al., 2016[3]). The accuracy georeferencing of every image may be largely influenced by the number of ground control points (GCP) used in the procedure. It is expected that in coastal areas the georeferencing errors are maximized due to a lower number of GCP. It will be crucial to control these errors for every couple (sensor; POC site) as they will cumulate with detection errors inherent to the algorithms proposed by the consortium partners. Although some of those algorithms theoretically meet the end-user requirements, large georeferencing errors may prevent from generating coastal indicators with sufficient accuracy. During POC activities the georeferencing accuracy will be addressed and performing an additional georeferencing for specific couples (sensor; POC site) with GCP selected by consortium partners might appear as necessary.

4.2.2 General limitations

Production of coastal indicators using optical imagery will not be always possible due to the cloud coverage sometimes overlapping the POC sites. This might not be a major limitation for indicators that can also be produced using SAR-based algorithms, such as the waterline, the beach width, dune and cliff lines (extracted from SAR-derived DEM).

The seabed cover mapping and bathymetry (through water colour inversion) products needs clear water to be generated. This requirement is not always met in most coastal areas and even rarely in areas with high hydrodynamics (strong current, energetic waves) and/or under river influence with discharge of fine suspended particulate matter, which both decrease the water transparency. Although several non-cloudy images per year are acquired over the POC sites concerned by these coastal indicators, the production frequency production achievable might be limited to few products per year at some sites.

The tide effect can also represent a limitation as it drives large cross-shore fluctuations of the landward extension of the water body. This makes some image-extracted indicators irrelevant to monitor coastal erosion if not produced under specific constrains such as using only images acquired at high tide for the waterline indicator in macro- and mega-tidal coastal areas.

4.2.3 Image resolution

This section makes the inventory of the resolution of the optical (Table 4-1) and SAR (Table 4-2) images associated with the different satellite sensors and image production modes that were preliminary identified to conduct the POC activities. Additional sensors may be used according to the availability of images at specific sites for specific dates.

Table 4-1 – Resolution of multispectral image acquired from different optical sensor. (ps) indicates that panchromatic sharpening has been used to enhance the original image resolution.

Image resolution (m)	0.5	1.5	5	6	10	15	20
Optical image source	Pléiades 1A/1B	SPOT6 (ps) SPOT7 (ps)	SPOT5 (ps)	SPOT6 SPOT7	Sentinel-2, SPOT5, SPOT4 (ps)	Landsat 7 (ps) Landsat 8 (ps)	SPOT1-4

[2] *Gascon et al., 2017. Copernicus Sentinel-2A Calibration and Products Validation Status. Remote Sensing, 9, 584. doi:10.3390/rs9060584.*

[3] *Yan, L., Roy, D.P., Zhang, H., Li, J., Huan, H., 2016. An Automated Approach for Sub-Pixel Registration of Landsat-8 Operational Land Imager (OLI) and Sentinel-2 Multi Spectral Instrument (MSI) Imagery. Remote Sensing, 8, 520, doi:10.3390/rs8060520.*

Table 4-2 – Resolution of SAR image acquired from different SAR sensor.

Image resolution (m)	3	8 x 4 (rg x az)	15
SAR image source	TerraSAR-X, TanDEM-X Cosmo-SkyMed	ERS1-2 SAR, ENVISAT ASAR	Sentinel-1

4.3 Cliff lines

The analysis of collected end-user needs have shown that for the “shoreline” family of products, the most cited ones are the cliff foot and cliff apex. Indeed, both cliff foot and apex have received a high score (9 citations each) and that makes the provision of these products a necessity among coastal managers.

In particular, in the cases of rocky coasts end-users are asking for the monitoring of cliff foot and cliff apex, with a planimetric accuracy of 1-5 m in average, which indeed is enough to provide adequate quantification of cliff retreat. Meantime, for coastal rocky cliffs, some end-users requested products that allow the monitoring of cliffs’ morphological change. Specifically, for the French POCs, New Aquitaine region and South-west France, the requested products allow to track the morphological change of the cliff front, including erosion scar development cliff front area and slope change, and material volume displaced by past landslides. The knowledge of these changes provides a better understanding of the dynamics of eroding cliffs, in particular in the French and Greek POC areas, where several critical infrastructures are located nearby eroding cliffs. Such products are expected to be produced and delivered 2 times per year (before and after the winter) with a 2-m planimetric accuracy. The end-user also requested the products to be generated before and after every oceano-meteorological event (energetic aggressive waves, heavy rains), which may occur at least 6 times a year.

The consortium members address the previously specified indicators with the proposed algorithms: 1a/1b-3c/3d and 3i. In particular, 1a is constituted by a set of algorithms for DEM generation deployed on VHR optical imagery, validated during commercial projects for different morphologies with a relative horizontal accuracy of 1 meter and a relative vertical accuracy of 2-3 meters. Indeed, this is compliant with the need expressed by the end-users for horizontal accuracy of 1 meter and a vertical 1-5 meters.

Algorithm 1b proposes DEM generation from SAR data, also validated during commercial projects, with RMSE of 8.2 meters using TanDEM-X data. POC sites with end-users requesting DEM generation can make use both of 1a and 1b algorithms, where also a further investigation on firing users need will be made (mostly for 1b).

The “family” 3 of algorithms, include key indicators useful to assess the morphodynamics of different subaerial areas along the rocky coasts and to mitigate risks related to erosion processes. Algorithm 3c relies on the availability of a DEM that includes the cliff face and part of the subaerial domains seaward and landward the cliff face so as to have the cliff foot and apex within the DEM. The DEM can be using VHR optical images or from interferometry using VHR SAR images. The proposed algorithm for cliff foot extraction relies on a DEMs provided over a regular mesh and is expected to be able to detect automatically a reference line following locally the overall cliff face orientation. However, if this part of the algorithm lacks robustness, it may be necessary to provide the reference line or the transects for each POC site. We have to note that 3c algorithm has not yet been validated, while it will be further tested in the POC.

Algorithm 3d is relying on the manual linear feature extraction deriving from DEMs with the use of VHR optical data. Validation of algorithm has been performed during past projects with results of 2-3 times the pixel size accuracy, which for the case of Pleiades data (0.5m resolution) it could be around 1.5-2meters which is compliant with the end-users’ needs.

Algorithm 3i is based on supervised classification of the spectral signature of the different types of ground cover at sites where the transition between specific types of cover can actually locates the cliff foot or cliff top line. Algorithm 3i is quite experimental, relies on HR imagery and is expected to reach a maximal accuracy of the order of the image resolution. This usually does not match with end-user expectations.

Table 4-3 - Requirements for indicator "Cliff" for POC sites where interested end-users have been interviewed.

Country	Coastal region	POC sites	Accuracy (m)		Production frequency (yr^{-1}) *exact dates*	Suggested combination of algorithms and EO data		
			Horizontal	Vertical		Algorithm	Image reso. (m)	Comments
France	Normandy	Calvados	1	1-5	1/5-ems (2012, 2016)	1a/1b-3c/3d	1	Probably usage only of 1a(alg),3d
France	Normandy	Seine-Maritime	1	ng	1/5-ems (2012,2016)	1a/1b-3c/3d	1	Probably usage only of 1a(alg),3d
France	Nouvelle Aquitaine	Corniche Basque	1	ng	2(during spring water low tider,1 before&1 after winter)	1a/1b-3c/3d	1	
France	Nouvelle Aquitaine	Erretegia cliffs	1	ng	2 (11/2017,01/2018,3-4/03/2019)	1a/1b-3c/3d	1	
Greece	Eastern Macedonia & Thrace	Vistonis-Maroneia	1	1-5	1-10	1a/1b-3c/3d	1	
Greece	Eastern Macedonia & Thrace	Evros Delta	1	1-5	1-10	1a/1b-3c/3d	1	
Germany	Baltic Sea	Brothener Cliff	10	ng	1	1a/1b-3c/3d	10	Optical in case of high vegetation on cliff edges
Germany	Baltic Sea	Schönhagener Cliff	10	ng	1	1a-3d	10	
Portugal	From Porto to Peniche	Alcobaça coast	1	ng	2 post storms	1a/1b-3c/3d	1	
Portugal	From Porto to Peniche	Aveiro coast	1	ng	2 -post storms	1a/1b-3c/3d	1	

The methodology based on DEM and supervised classifications from VHR images cannot be used for investigating cliff changes over the last 25 year, as the development of regular acquisitions of VHR images essentially started these last 10 years. Although the end-users usually desire meter-scale accuracy for the detection of cliff lines and changes for recent and future periods, they may be still interested in obtaining the quantification of the overall cliff retreat over the last 25 years. Thus, algorithm 3i will also be used in combination with HR at sites where the conditions of application of this algorithm are met. This will include at least the extraction of the cliff foot at Erretegia and the cliff top at Seine-Maritime POC site. Long-term cliff foot changes at Erretegia will be investigated using images from SPOT1-5, Sentinel-2, ERS-1/2, ENVISAT and Sentinel-1 sensors. Long-term cliff top at Seine Maritime POC site will be investigated using images from SPOT1-5, Landsat 7/8 and Sentinel-2 sensors.

4.4 Dune foot

Four distinct algorithms (3a, 3b, 3d and 3h) have been proposed by the consortium members to address the end-user needs for production of the dune foot line, which represents one of the most relevant proxy of the shoreline position along sandy coasts on the interannual to longer timescales.

The requirements for this indicator collected during end-user interviews are exhaustively listed in Table 4-4 per POC sites. A metrical accuracy is requested by end-user for coastal areas experiencing regular and potentially large dune erosion events, such as observed in SW France and in NW Portugal. In the Mediterranean Sea sites where dune foot change rates are smaller due to lower energy wave conditions, such as for the Greek POC sites, an accuracy of 5 m is required. End-users from French and Portuguese POC sites are interested in a seasonal monitoring (before/after winter/summer and end of winter/summer, respectively) while Greek end-users will be satisfied with an annual monitoring. A post-storm monitoring mode is also asked by Portuguese end-users, which would represent 2-4 additional products to be derived per year.

While algorithm 3a and 3b are semi-automated approaches requiring a limited intervention from the operator (single calibration per sites + assisted removal of detection outliers), algorithm 3d is a fully manual digitizing process that requires a high level of expertise from the operator and time. Algorithm 3h also required a significant intervention from the operator to build the reference database used by the classifier. However, apart from this initial intervention the method remains almost automated. For coastal areas with well-developed and regular foredunes (alongshore homogeneous and pretty rectilinear) such as in SW France or NW Portugal, algorithms 3a, 3b and 3h represent efficient tools and should be used, while for coastal areas presenting low amplitude dunes and tortuous coastlines algorithm 3d should be preferred as (semi-) automated approach may lead to numerous detection outliers and would requires to handle a lot of specific cases.

As the transition between the upper beach and the dune system (where the dune foot is located) often extends horizontally over spatial scales of few meters to ten meters, only the use of VHR EO data (resolution ≥ 5 m) are envisaged when addressing changes on the event (storm), seasonal and annual scales. Algorithm 3i, which relies on HR data, appears as not really relevant with respect to the end-user expectations.

The use of the algorithm 3a in combination with VHR EO data such as Pléiades imagery led to a dune foot detection with an usual accuracy of 5 m. The use of the algorithm 3b with DEM derived from stereo or tri stereo Pléiades imagery is expected to lead to a similar accuracy or even better (2-5 m). Finally, the digitizing approach (algorithm 3d) used for cliff line detection have shown accuracy of 3-4 times the resolution of the VHR images used to compute the cliff DEM. In case ground control points were available to improve the DEM positioning, an accuracy of 2 m has been reached. But due to a lower number of patterns of recognition within dune systems, dune DEMs are expected to be of lower accuracy than cliff DEMs. Thus, the use of algorithm 3d for dune foot detection should lead to a maximal accuracy of 5 m. All in all, these three algorithms seem to offer similar accuracies.

The computation of DEM requires a pair or more of images with specific requirements that are not always fulfilled, which makes the algorithm 3b and 3d hardly relevant regarding a production frequency higher than one per year. In contrast, the algorithm 3a only requires a single image for every application, offering more potential for high production frequencies (several per years).

With the algorithms proposed by the consortium and current image availability, the end-user requirements may be satisfied only for the Greek POC site. For French and Portuguese POC sites, the requested production frequency should be fulfilled using algorithm 3a, whereas the expectation in terms of horizontal accuracy might not be reached with the proposed algorithms. However, within the POC activities validation works will be performed to assesses carefully the final product accuracy, which will then be presented to French and Portuguese end-users for possible compromises on their initial requirements. Note that, when possible algorithm 3b will be used in parallel to 3a to see if a possible improvement in accuracy is reached by using geometrical analyses on elevation profiles from DEM rather than textural analyses on single optical image.

Table 4-4 - Requirements for indicator "Dunes foot" for POC sites where interested end-users have been interviewed.

Country	Coastal region	POC sites	Accuracy (m)		Production frequency (yr^{-1}) *exact dates*	Suggested combination of algorithms and EO data		
			Horizontal	Vertical		Algorithm	Image reso. (m)	Comments
France	Aquitaine	Biscarrosse	1	-	4 *Feb.; Jun.; Aug.; Nov.*	3a	0.5/1.5	Use of 3b when DEM can be produced
Greece	Eastern Macedonia and Thrace	Vistonis-Maroneia	5	-	1	3d	0.5/1.5/3	Production frequency is not guaranteed due to possible low availability of (tri)stereo images
Portugal	Northwest coast	North of Aveiro lagoon and south of Aveiro lagoon	1	-	2 *End of summer and winter*	3a	0.5/1.5	Use of 3b when DEM can be produced
			1	-	ng (2-4) *Post-storm production*	3a	0.5/1.5	Use of 3b when DEM can be produced

The methodology based on DEM or supervised classification from VHR images cannot be used for investigating dune changes over the last 25 year, as the development of regular acquisitions of VHR images essentially started these last 10 year. Although the end-users usually desire meter-scale accuracy for the detection of dune change for recent and future periods, they may be still interested in obtaining a rough quantification of the dune retreat over the last 25 years. Thus, algorithm 3h will also be used in combination with HR at sites where the conditions of application are met. This will include at least the extraction of the dune foot at Biscarrosse and at South Aveiro Lagoon. Long-term / large-scale dune foot changes at Biscarrosse and at South Aveiro Lagoon will be investigated using images from SPOT1-5, LANDSAT 7/8 and Sentinel-2 sensors.

4.5 Water lines

Water lines represent an important indicator for stakeholders involved in coastal monitoring and prevention activities. In order to address user needs, the consortium proposes 4 algorithms for water line extraction (2a, 2b, 2c, 2d). There are three proposed methods for optic data (Water Line Detection using band ratios, Water Line Detection using NDWI, Water Line Detection using a supervised classification process) and one for SAR data (Water Line Detection using binary products from SAR amplitude data).

The user requirements for “water line” for every POC are presented in Table 4-5. Validation work performed for the algorithms that extract waterline from optical images does not fully match the accuracy requested by users, except the Vistonis-Maroneia POC site from Eastern Macedonia and Thrace. Apart from this POC site, the end-user requested an accuracy better than 5 m. Further adaptation of the methods on very high-resolution images could lead to improved results. Even so, it may not be possible to obtain accuracies of 1 m or higher, which is requested within 5 POC sites. Regarding the frequencies, in all POC sites except Romania, there are one or two requests per year. In Sulina- Sfantu Gheorghe POC users demand water line monthly, while in 2 Mai – Vama Veche the frequency is 4 per year. Revisiting time of satellite should successfully fulfill the end-user requirements regarding frequencies. For POCs in the Romanian coastline which requested monthly products, SAR data could be used in case no optical image will not be available due to cloud contamination.

Table 4-5 - Requirements for indicator "water line" for POC sites where interested end-users have been interviewed

Country	Coastal region	POC sites	Accuracy (m)		Production frequency (yr^{-1}) *exact dates*	Suggested combination of algorithms and EO data		
			Horizontal	Vertical		Algorithm	Image reso. (m)	Comments
Greece	Eastern Macedonia and Thrace	Evros Delta	1 (0.5)	-	0.5	2a, 2b, 2c, 2d	5/8/10	
		Vistonis-Maroneia	10	-	1	2a, 2b, 2c, 2d	5/8/10	
Germany	North Sea	Sylt Odde	1	-	1 (2011, 2012, 2013, 2014, 2015, 2016, 2017, 2018, 2019, 2020)	2a, 2d	1-10	Algorithm 2d may be used if no optic image is available. VHR data will be tested during POC.
	Baltic Sea	Kiel Probstei Sylt Odde						
Romania	All coastline	Sulina-Sfantu Gheorghe	3	-	12 (2017-2018)	2b, 2d	5/10	Algorithm 2d may be used if no optic image is available
			1	-	12			
			5	-	12 (from 2015 to present)	2b, 2d	5/10	Algorithm 2d may be used if no optic image is available
		2 Mai – Vama Veche	<1	-	4	2b, 2d	5/10	Algorithm 2d may be used if no optic image is available

4.6 Middle of swash zone

The swash zone is that part of the beach alternately covered and exposed by uprush (onshore flow) and backwash (offshore flow), respectively. The middle of the swash zone can be approximated by the average of the waterline position over a time period of the order of some minutes, that is, the typical time scale of a wave set driving this phenomenon. Along coasts experiencing large tidal ranges, this location of this virtual line can easily vary within a tidal cycle from tens to hundreds of meters. This indicator only make sense as a shoreline proxy if computed at high tides. It would then correspond to the Mean High-Water Level (MHWL) shoreline proxy commonly used at sites presenting large tidal ranges. For micro tidal coasts, the cross-shore variation of the middle of swash zone during a tidal cycle remains low (of the order of 10m) making this proxy relevant to address shoreline change.

Based on the end-user requirement compilation (Table 4.6), in PACA region (SE France) an accuracy of 1-5 m is requested along with production frequency for seasonal, bi-monthly (from October to June) and post-storm (before/after) monitoring. The bi-monthly production represents a total of 18 product per year. Because of the variability in yearly storm occurrence and different levels of coastal resilience to storms, the production associated with the post-storm monitoring can vary a lot from one year to another. Based on a minimal number of major storms of 2-4 per year, the post-storm monitoring represents a total of 4-8 products a year. In Romania, an accuracy of 3-5 m with a monthly production frequency is required by end-users.

No specific algorithm has been proposed for this indicator by consortium partners. For microtidal environments, averaging several waterlines extracted using algorithms (2a,2b,2c,2d) based on subsequent EO data may allow computing a composite water line that may certainly fit well with the middle of swash zone proxy measured on the field. The time period used to compute the composite waterline have to be short enough to ensure that no significant erosion or accretion events have occurred. The advantage of using algorithm 2c, which relies on SAR imagery, is that for every image available a waterline can be produced independently from the cloud coverage. The use of both optical- and SAR-based algorithms is required to reach the high production frequencies requested by the end-users. Regarding optical algorithms, the best algorithm candidate would be the algorithm 2b as soundful validation works have shown an overall sub-pixel accuracy. Using VHR EO data should allow fulfilling the end-user requirements in terms of accuracy.

Algorithm 3a may also be useful to retrieve the middle of the swash zone from VHR optical data for microtidal regions.

Table 4-6 - Requirements for indicator "Middle of swash zone" for POC sites where interested end-users have been interviewed.

Country	Coastal region	POC sites	Accuracy (m)		Production frequency (yr^{-1})	Suggested combination of algorithms and EO data		
			Horizontal	Vertical	*exact dates*	Algorithm	Image reso. (m)	Comments
France	PACA	Bays of Hyères, Saint-Raphaël and Nice, and Camargue	1-5	-	2-3 *Sept./Oct.; Jan.; May/Jun*	3a, 2b, 2d	0.5/1.5/3/5	-
			1-5	-	18 *Fortnightly from Oct. to Jun.*	3a, 2b, 2d	0.5/1.5/3/5	-
			1-5	-	4-8 *Before/after storm event*	3a, 2b, 2d	0.5/1.5/3/5	-
Romania	All coastline	Romanian/ Danube Delta Littoral	ng (3-5)	-	ng (12)	3a, 2b, 2d	0.5/1.5/3/5	-

As for dune foot and cliff line indicators, production of the middle of swash zone will also be tested using HR images from SPOT1-5, LANDSAT 7/8, Sentinel-2, ERS-1/2, ENVISAT and Sentinel-1 sensors to allow addressing changes of this indicator over the targeted period of 25 years.

4.7 Maximum swash excursion during major storms

Several strategies shall be envisaged to derive maximum run-up (or swash) excursion during storms. These strategies will depend on the proxy chosen to identify the indicator and also on the capacity to obtain relevant images during of within the days following the storms.

As shown in the Requirement Baseline, the position of the maximum run-up (or swash) excursion over the beach, as reached by water during storm events has been cited are cited 13 times in the collected requirement forms, in France and in Romania. End-users are requiring a metric planimetric accuracy in the range of 1-5 m. In Romania, they require the detection of the run-up limit after individual storms, and, in France, during or within the few days consecutively to severe storm events. The detection service would be activated upon request in case of emergency and/or major storm events. In France, the location of the "pied de l'escarpement » is chosen as the indicator of maximum storm excursion. This proxy could be extracted within the hours / days following the storm. During the storm another proxies must be envisaged: the waterline.

Finally, a few days / weeks after a storm, it may be interesting to use as a proxy the change in land cover before / after storm. However, this option has not been requested from the end-users.

The location of the "pied de l'escarpement » (rapid change in altitude) could be extract from DEM (algorithms 1a and 1b) or from optical image texture analysis (algorithms 3a). However, with regards to end-user requirements, and in particular with regards to the expected planimetric accuracy, very high-resolution optical imageries would be the only data acceptable to retrieve the maximum swash excursion in PACA region.

Various algorithms exit to retrieve the waterline, based on SAR and optical data. All VHR sensors should be used simultaneously to multiply the chance to get an exploitable image at the time of the storm maximum. This necessitates to order image a few hours before the storm (emergency mode). Eventually, in submerged regions, the acquisition of relevant data can be made even a few hours / days after the storm. The waterline will continue to indicate the maximum run-up excursion during the past storm. This option has not been cited by the focussed end-user but may be relevant in other regions.

Table 4-7 - Requirements for indicator "Maximum swash excursion " for POC sites where interested end-users have been interviewed.

Country	Coastal region	POC sites	Accuracy (m)		Production frequency (yr^{-1})	Suggested combination of algorithms and EO data		
			Horizontal	Vertical	*exact dates*	Algorithm	Image reso. (m)	Comments
France	PACA	Hyères, Saint-Raphaël and Nice, and Camargue	1 – 5 m		During storm events	1a, 3a	< 5 m	Proxy : "Pied de l'escarpement"
Romania	All coastline	Romanian/ Danube Delta Littoral	3 – 5 m		During storm events	1a, 3a 2a => 2e	< 5 m	Proxy : "Pied de l'escarpement" a few hours days after storm Waterline during the storm (image acquisition not guaranteed)

4.8 Submerged sandbars

Nearshore sandbars could represent a natural protection system against erosion and maximum run-up limit in case of an extreme event. Two algorithms are proposed (6a and 6b) by the consortium addressing this issue. They were both tested on two POC sites, 6a in Sulina-Sfantu Gheorghe sector and 6b in the south part Sylt Odde island. The validation work performed for 6a algorithm showed good results for water line extracted from Sentinel-2 data. The use of higher-resolution images may increase accuracy.

The user requirements for "submerged sandbars" for every POC are presented in Table 4-8. Results of the validation work are in line with the accuracy requested by end-users (10 m horizontal accuracy). As presented in Table 4-8 algorithm 6a will be used for Sulina-Sfantu Gheorghe POC and 6b for Kiel/Probstei, respectively. For the other POCs, none of the methods were tested yet, but both will be taken into consideration and the one with the most promising results will be chosen. The production frequency requested by end-users should be met for all POCs, except the Sulina-Sfantu Gheorghe, where it may be influenced by the availability of cloud free images or the occurrence of high turbidity values.

Table 4-8 - Requirements for indicator "Submerged sandbars" for POC sites where interested end-users have been interviewed.

Country	Coastal region	POC sites	Accuracy (m)		Production frequency (yr^{-1}) *exact dates*	Suggested combination of algorithms and EO data		
			Horizontal	Vertical		Algorithm	Image reso. (m)	Comments
France	New Aquitaine	Biscarrosse beach	ng (5-10)	-	2	6a, 6b	10	Not applied yet in this POC.
		Bidart central beach Erretegia cliffs	5-10	-	3	6a, 6b	10	Not applied yet in this POC.
Greece	Eastern Macedonia and Thrace	Vistonis-Maroneia	5-10	-	0.3	6a, 6b	10	Not applied yet in this POC.
Germany	Baltic Sea	Kiel/Probstei	10	-	1 (*2011, 2012, 2013, 2014, 2015, 2016, 2017, 2018, 2019, 2020*)	6b	10	-
Romania	All coastline	Sulina-Sfantu Gheorghe	10	-	12 (*since 2015*)	6a	10	-

4.9 Beach width

End-users from New Aquitaine region (SW France) requested the cross-shore distance between wet/dry sand interface to the dune foot (i.e. upper beach width), between wet/dry sand interface and the water line at the low tide (i.e. lower beach width) and between hide tide waterline and the dune foot (i.e. high tide beach width to get the usable beach width at high tide). The tidal level at the time of image acquisition is required to assess the type of beach width that is computed. Additionally, one end-user from Normandy region (N France) requested the width of shingle deposits (shingle bands) down the cliffs/dunes and lying either on sandy or rocky bottoms.

Based on the end-user requirement compilation (Table 4.9), an accuracy of 1-5 m is usually requested for seasonal monitoring of sandy beach width. One end-user (coastal expert) also requested production of this indicator for every usable HR image from Sentinel missions to monitor easily hotspots of erosion in coastal areas similar and adjacent to Biscarrosse beach. This represents more or less a weekly production frequency. Regarding the width of shingle bands, an ideal accuracy of 0.5 m is desired by the end-user, but an accuracy of 1-5 m could still bring relevant information. As for sandy beach, the width of shingle bands should be produced on a seasonal basis, though an annual production frequency remains acceptable for the end-user. Specific dates have also been requested for comparison with end-user validation data.

One algorithm (3e) has been proposed by the consortium members to address the end-user needs for estimation of beach width and analysis of date-to-date beach width changes. This algorithm is only destinated to compute the useable beach width, that is the cross-shore distance between the high tide waterline and the landward reference line. The other types of beach width are disregarded as to the author knowledge the wet/dry line is a visual pattern that rapidly evolve according to sun exposition and wind conditions and can be affect by the water table height. The algorithm 3e has not been validated yet but the implementation of the algorithm will be quite straightforward without many specific cases.

The horizontal accuracy of this algorithm depends on both the accuracy of the waterline and the reference line. If the reference line was provided by the end-user (no spatial error) and not derived from satellite imagery, the accuracy would reduce to the accuracy of the water line extraction algorithm, which usually is of the order of the image pixel resolution (sub-metric to pluri-metric). Using VHR EO data to extract waterline and subsequently to compute the width of sandy beaches should allow to fulfil the end-user requirements for the seasonal monitoring.

For the monitoring of hotspots of erosion, it may be difficult to achieve the weekly production along with the 1-5 m accuracy without tasking weekly acquisition from VHR satellite sensor, a costly operation which is also likely not possible due to choices in tasking priority made by the satellite owners. The use of HR EO data from Sentinel-1/2 would certainly match with the production frequency, but not with the accuracy expected. Anyway, this will be tested and presented to end-users.

Algorithm 3e does is not adequate to compute the width of shingle bands and an alternative algorithm should be applied. The shingle areas over the beach and rocky platforms need first to be extracted using classification algorithms (5a, 5b, 5c) including a shingle class among others. Then, the cross-shore distance from one boundary (landward boundary) to the other (seaward boundary) of the shingle patches could be computed alongshore. As shingle spectral signature can be close to sand and rocky platform signatures, large errors could arise and only a good knowledge of the ground reality can lead to accurate classification. This source of error could be still reduced for the sand/shingle ambiguity using SAR images since shingle has more rugosity than sand. An attempt of production of shingle band width will be made at the date for which validation data exists.

Table 4-9 - Requirements for indicator "Beach width" for POC sites where interested end-users have been interviewed.

Country	Coastal region	POC sites	Accuracy (m)		Production frequency (yr^{-1}) *exact dates*	Suggested combination of algorithms and EO data		
			Horizontal	Vertical		Algorithm	Image reso. (m)	Comments
France	New Aquitaine	Biscarrosse beach	ng (1-5)	-	*4 Nov.; Feb.; Jun.; Aug.*	3e	0.5/1.5/3/5	-

			5-10	-	*52* *weekly*	3e	10/15	For erosion hotspot monitoring. Cannot be guaranteed due to potential unavailability of EO data
		Bidart central beach	1-5	-	4 *Before/after winter/summer*	3e	0.5/1.5/3/5	-
	Normandy	Calvados POC site Seine-Maritime POC site	0.5-5	-	1 (*2006; 2009*)	5a, 5b, 5c	0.5/1.5/3/5	Width of shingle bands. Experimentation with classification algorithms will be made.
			0.5-5	-	1-4 (annually or seasonally)	-	-	Width of shingle bands. Limit: No guarantee of success with any of the proposed algorithms.

As for other indicators (dune foot, cliff lines, middle of swash zone) production of the beach width will also be tested using HR images from SPOT1-5, LANDSAT 7/8, Sentinel-2, ERS-1/2, ENVISAT and Sentinel-1 sensors to allow addressing changes of this indicator over the targeted period of 25 years. This will be done at sites where large variation of the beach width were observed to ensure the detection of a signal of beach width changes.

4.10 Tidal flat morphology: erosion at tidal creek edges and tidal creek characterization

Three algorithms are proposed to work on intertidal flat areas. Two of them are proposed for the detection of erosion at tidal creek edges, of which one is based on SAR data (2e), the other one on optical data (5c). Both algorithms might be combined in the end in order to retrieve the most reliable information from them. One algorithm is dedicated for the characterization of tidal creeks, such as number of creeks and creek endings (3g). All algorithms used in conjunction provide the information needed for the indicator for erosion in intertidal flats.

The morphological characterization has been asked by one user in Germany and the test sites that are concerned are located in the German part of the Wadden Sea at the Schleswig-Holstein North Sea Coast. The user was designing an own group of indicators that he called WASERI (Wadden Sea Erosion Indicator). The user requirements horizontal accuracy of the morphological intertidal products was specified with 10 meters, which requires the at least Sentinel-2 data, but also the application in VHR data are suggested. Especially for the creek headings, VHR data is needed. A vertical accuracy is not applicable as the focus is on lateral changes and no vertical information is provided by the products. The information shall be available once a year. The reference year shall e 2001, while the years for assessing the changes are requested to be 2011-2020 (yearly basis).

Algorithm 2e and 5c have been applied already to a number of images of dry-fallen intertidal flats, but the application for coastal erosion is a new aspect in the interpretation of the results. Therefore, some adjustments are expected for 2e and 5c. Validation was performed on the outcome of the algorithms with *in situ* data but not for coastal erosion, yet. The validation will be performed within the POC and the user will provide products derived from laser scan data as reference.

The algorithm 3g for the tidal creeks characterization (heads, endings) has not been applied yet and has an experimental character. As this algorithm is on its very beginning, it is not yet clear if it will fulfil the user requirements.

The user for the intertidal indicators has experiences with remote sensing products, and it is expected that the algorithm is developed in close cooperation with the user. This ensures a good balance between expectations and realistic assessment of the products.

Table 4-10 – Requirements for indicator "Tidal flat morphology" for POC sites where interested end-users have been interviewed.

Country	Coastal region	POC sites	Accuracy (m)		Production frequency (yr^{-1}) *exact dates*	Suggested combination of algorithms and EO data		
			Horizontal	Vertical		Algorithm	Image reso. (m)	Comments
Germany	North Sea Wadden Sea	Blauortsand	10m	na	1/yr *2011, 2012, 2013, 2014, 2015, 2016, 2017, 2018, 2019, 2020*	2e, 5c, 3g	10m or higher	A combination of all three algorithms is envisaged in order to address the user requirements.
		Nordstrand						
		Medemgrund						

4.11 Bathymetry

Three distinct algorithms (4a, 4b and 4c) have been proposed by the consortium members to address the end-user needs for production of bathymetry maps and analysis of date-to-date bathymetric changes. End-users essentially requested the bathymetry to cover shallow depths, that is from 0 to approximately 10-m deep.

Algorithm 4c (wavelength inversion) has been validated for depths ranging from 15 to 30-m deep. This does not really match the needs expressed explicitly by the end-user, although some might still be interested in knowing the bathymetry in deeper waters. Nevertheless, for algorithm 4c, an alternative approach based on wavelet transform (WT) instead of the Fourier transform may upgrade this algorithm to inverse depths in shallower waters (ex. 1 – 10 m depth). Since wave crest inversion is necessary where water is turbid or water surface is rough, algorithm 4c with WT may be considered for POC if validation data can demonstrate the accuracy of the results.

Apart from this potential experimental demonstration of algorithm 4c, the POC will principally focus on two other algorithms (4a, 4b) (water color inversion) to retrieve bathymetry in shallow waters. Their capability to fit the end-user requirements are here assessed.

The requirements for the indicator "Bathymetry" collected during end-user interviews are exhaustively listed in Table 4-11 per POC sites, providing the clear picture of the full range of requirements we have to address.

In short, a higher horizontal and vertical accuracy (2 m and 0.2- 0.5 m, respectively) is usually requested for sites with weak hydrodynamics and morphodynamics, while a lower accuracy remains (5-10 m and 0.5-1 m, respectively) acceptable for highly-dynamic sites where submerged sandbars are typically of larger characteristic length.

A great variability in the requested production frequencies is observed. For most sites production a typical seasonal motioning with 2-3 bathymetries per year is a common request: one at the end of the winter (March-April); one at the end of the summer (September-October); and eventually another one during the summer (July-August). An emergency/post-storm monitoring – production of a bathymetry after each major storm – has also been requested at some sites. Due to variability in yearly storm occurrence and different levels of coastal resilience to storms, the production efforts can vary a lot from one site to another and from one year to another. Nevertheless, it is assumed that this monitoring mode would represent at least the production of 2-4 additional bathymetries per year. At the other end of the spectrum, a monitoring for long-term monitoring analysis has also been requested. This consists in the production one bathymetry every 3-5 years. Because on these timescales the morphological change is expected to be larger than for the yearly/seasonal monitoring, end-users would readily accept the delivery of the bathymetry with lower horizontal and vertical accuracy.

The algorithms 4a and 4b show vertical accuracy in the range of 0.3-1 m and 0.6-1.3m, respectively. This indicates that both methods could fit most of the end-user requirements, except for high-frequency surveys of Bays of Hyères, Saint-Raphaël and Nice. However, for annual surveys, a lower accuracy range is acceptable for these end-users.

Concerning the horizontal accuracy, this is essentially related to the sensor resolution and image pixel georeferencing accuracy. Assuming a perfect georeferencing, the Table 4-1 gives the horizontal accuracy that could be obtained from the different optical sensors investigated during phase 1. Here the end-user requirements can be easily satisfied as long as the images are reachable.

In theory the revisiting time of satellite considered for phase 1 are short enough to fulfill production frequencies requested by end-user. Although a large number of those are useless due to the presence of clouds, turbid waters, breaking waves, several per year are of high quality for algorithm application. Thus, the seasonal, annual and long-term production frequencies seem achievable over most areas. Successful demonstration has been carried out in most regions; however, images shall be checked to show that algorithms 4a and 4b can be safely deployed at Bidart central beach Erretegia cliff, in Normandie and along the Portuguese coast, where turbid waters are recurrent.

In addition, the post-storm production cannot be guaranteed, as after storms clouds may be still present and turbid waters usually persist several days to some weeks, preventing from algorithm application. Finally, note that the algorithm 4a requires some input bathymetric data measured at the date of image acquisition (or close date) for calibration. Thus, it will be impossible to use this algorithm for sites where no any bathymetric measurement (with enough metadata) have been made, which potentially represent a large number of sites. For each POC sites where the indicator "Bathymetry" is requested a combination of algorithm with EO data type is proposed when it truly fits with end-user requirements.

Table 4-11 - Requirements for indicator "Bathymetry" for POC sites where interested end-users have been interviewed.

Country	Coastal region	POC sites	Accuracy (m)		Production frequency (yr^{-1}) *exact dates*	Suggested combination of algorithms and EO data		
			Horizontal	Vertical		Algorithm	Image reso. (m)	Comments
France	New Aquitaine	Biscarrosse beach	5 - 10	0.5 - 1	2	4b	5/6/10	Possible replacement of 4b by 4a at specific dates
		Bidart central beach and Erretegia cliff	5	1	3 *Sept./Oct.; Apr.; Jul./Agu.*	4b	5	Possible replacement of 4b by 4a at specific dates
	Normandy	Calvados POC site Seine-Maritime POC site	10	0.4 - 1	ng (2)	4b	5/6/10	Possible replacement of 4b by 4a at specific dates
	PACA	Bays of Hyères, Saint-Raphaël and Nice	2	0.5	1/3 - 1/5	4b	0.5/1.5	Possible replacement of 4b by 4a at specific dates
			2	0.1 - 0.2	2	-	-	Limit: vertical accuracy
		Camargue	2 - 10	0.5	1/3 - 1/5	4b	5/6/10	-
			2 - 10	1	2	4b	5/6/10	-

Greece	Eastern Macedonia and Thrace	Vistonis-Maroneia	ng (2 - 10)	1	ng (1/3 – 1/5)	4b	5/6/10	-
Portugal	Northwest coast	North of Aveiro lagoon and south of Aveiro lagoon	10	ng (1)	2 *End of summer and winter*	4b	10	Possible replacement of 4b by 4a at specific dates
			10	ng (1)	ng (2-4) *Post-storm production*	4b	10	Cannot be guaranteed
Romania	All coastline	2 Mai	10	1	2	4b	10	-
		Sulina	10	1	ng (2-4) *Emergency production*	4b	10	Cannot be guaranteed
		Sulina	10	ng (1)	12 *Monthly*	-	-	Limit: production frequency

Images from SPOT1-4 and Landsat 7/8 sensors will also be used in combination with algorithm 4b to address long-term changes of the bottom elevation in shallow water areas. This will be conducted at least at the following POC sites: Biscarrosse, Bay of Saint Raphaël, Camargue and Vistonis-Maroneia.

4.12 Underwater seabed type (sandy/rocky/vegetated)

Three different classification approaches (5a, 5b and 5c) have been identified by the consortium members to address the end-user needs for classification. Since seabed mapping implies a water penetrating signal, the approach 5b which relies on SAR data is not considered here. Usually, the interest in seabed maps has been expressed by end-users that are also interested by bathymetry.

During end-users interviews, requirements for the indicator “Underwater seabed type” were collected. These are listed in Table 4-12 per POC sites. In terms of horizontal accuracies, VHR sensors have to be targeted for most of the French sites (mainly Pléiades and/or SPOT6/7 satellites), whereas for the Northwest coast of Portugal and eventually Camargue can be mapped with coarser sensors such as Sentinel-2. Since no information has been provided in terms of updating frequency, the same production frequency and seasons of interest as bathymetry are assumed to be expected. The same limits as pointed out in the bathymetry section apply therefore also for this product. However, a frequency of 1 to 5 maps per year seems reasonable for all sites, with the exception of Bidart central beach and Erretegia cliff where frequent episodes of high turbidity levels have been observed.

The expected classes to be mapped are very similar among the POC sites and mainly focus on the differentiation between sandy and rocky bottoms. In the French PACA region, an additional interest has been expressed to detect posidonia seagrass as well as dead seagrass fields. The potential detection of such seabed types depends on water depth and bottom albedo. Since sandy bottoms are highly reflective, they can be distinguished through the water column until up to approximately 10 m. Rocky and algal bottoms are less reflective and can only be expected to be properly detected at lower depth (up to ~5 m).

The identified classification algorithms 5a and 5c can be applied independently of the targeted sensors for each POC sites. The use of 5a algorithm requires an expert a priori knowledge of the location of the different bottom types in order to create training polygons to feed the classification model. Also, *in situ* inventories with geolocation of the observed samples can be very useful either to drive the building of the training set or either to validate the produced seabed map. In case of 5c approach, an *in situ* measurements dataset containing radiometric spectra of the targeted bottom types can be valuable in order to identify which spectral bands to be used and thereby to build the decision tree. If these data are not available, a priori knowledge of the location of the different bottom types may be needed to define the decision rules by trial and error.

Table 4-12 - Requirements for indicator " Underwater seabed type " for POC sites where interested end-users have been interviewed.

Country	Coastal region	POC sites	Accuracy (m)		Production frequency (yr^{-1}) *exact dates*	Suggested combination of algorithms and EO data		
			Horizontal	Vertical		Algorithm	Image reso. (m)	Comments
France	Aquitaine	Bidart central beach and Erretegia	5	-	3 *Sept./Oct.; Apr.; Jul./Agu.*	5a,5c	6/10	Rocky/Sandy bottoms - Limited due to frequently high turbidity levels
	PACA	Bays of Hyères, Saint-Raphaël and Nice	2	-	1/3 - 1/5	5a,5c	2	Rocky, sandy bottoms and posidonia fields
			2	-	2	5a,5c	2	-
		Camargue	2 - 10	-	1/3 - 1/5	5a,5c	2/10	Rocky/Sandy bottoms
			2 - 10	-	2	5a,5c	2/10	Rocky/Sandy bottoms
Portugal	Northwest coast	North of Aveiro Lagoon and	10	-	2 *End of summer and winter*	5a,5c	10	Rocky/Sandy bottoms
		South of Aveiro Lagoon	10	-	ng (2-4) *Post-storm production*	5a,5c	10	Rocky/Sandy bottoms

4.13 Coastal and intertidal habitat and land cover mapping

Three algorithms have been described for the detection of coastal and intertidal habitats and land cover mapping (algorithm group 5). Two of the algorithms are based on optical data; one is based on a supervised classification (5a), the other on a decision tree classification (5c). The third algorithm proposes the classification of texture features base on SAR data which can be classified by supervised or machine learning techniques (5b). While 5a and 5b are focusing on coastal land cover classification, 5c is dedicated to intertidal flat habitats. A combination or integration of the textural features derived from SAR images could be integrated in the supervised classification of optical data for retrieving higher accuracy.

Classification products were requested by the users for detecting changes in the coastal land use in relation to coastal erosion (Portugal), for better protection measures and planning at the coast (Portugal, Greece), for assessment of vulnerability of the land affected by coastal erosion (France) and as indicator of habitat changes for intertidal erosion (Germany). The requirements for spatial resolution and accuracy range from 0.3m to 10m.

The requirements expressed by Greece cannot be fulfilled by the available data base and proposed algorithms. Especially the requirements for very high resolution of 0.3 m and also the accuracy for 0.3m is too ambitious for the proposed approaches products and data available. The requirement for mapping individual species in this resolution will also not be possible and for the requested baseline year 1970 no sufficient data expected.

The other users require a resolution of 10m which allows the usage of Senitnel-2 data. The requirements of accuracy for correct classification (overall accuracy, producer's accuracy etc.) is not provide by the users. However, the horizontal accuracy has been specified with 1 to 10m. The algorithms should be able to fulfil the requested coastal and intertidal surface types: urban areas, beaches, dunes, vegetated areas, coastal wetlands, intertidal seagrass meadows, intertidal mussel beds, intertidal sediment types.

Table 4-13 - Requirements for indicator "Coastal and intertidal habitat and land cover mapping" for POC sites where interested end-users have been interviewed.

Country	**Coastal region**	**POC sites**	**Accuracy (m)**		**Production frequency (yr^{-1})** ***exact dates***	**Suggested combination of algorithms and EO data**		
			Horizontal	**Vertical**		**Algorithm**	**Image reso. (m)**	**Comments**
France	Normandy	Littoral of Normandy	ng	-	Every 5yrs	5a, 5b (com-bined?)	10m	No information about the required resolution was given by the user. Sentinel-2 is proposed
Greece	Eastern Macedonia and Thrace	Delta of Evros River	0.3m	-	Every 10 yrs Baseline: 1970 1980, 1990, 2000, 2010, 2018	5a	1-10m	The requiremnts cannot be fully met. It should be discussed if lower resolution products would still be of interest
Germany	North Sea Wadden Sea	Blauortsand	10m	-	1/yr *2011, 2012, 2013, 2014, 2015, 2016, 2017, 2018, 2019, 2020*	5c	10m (1-5m)	VHR with higher spatial resolution will be tested in POC
		Nordstrand						
Portugal	North-west coastline	Municipality of Alcobaça	ng	-	1/yr Baseline: 1990	5a, 5b (com-bined?)	1-10m	
		Municipality of Ovar	1m	-	*1/yr.*	5a, 5b (com-bined?)	1-10m	

5 ALIGNING SPACE FOR SHORE PRODUCTS WITH EUGENIUS ONLINE PLATFORM

The EUGENIUS (EUropean Group of Entreprises for a Network of Information Using Space) infrastructure is based on a network of collaborative processing and archiving geospatial platforms. These platforms are based on existing processing facilities, available in Terra Spatium and also within EUGENIUS network partner premises built with Open Source software suites coping with OGC standards which guaranty the capabilities of the exchanges into the network (data, information, etc.) and allows several users to access data coming from different sources and with different formats online.

Moreover, end-users have the flexibility to manage or process datasets, create online processing tools (i.e. Web Processing Services, etc.), edit/download functionalities and in the end the platform is also a place for creation and delivery of EO services. For all the above reasons and taking into consideration the current trends for online fast access/visualization/post process and delivery of EO services, EUGENIUS online platform was selected as the most appropriate geospatial tool, not only for data exchange among partners but also for the dissemination of "Space for Shore" products to the end-users.

Hereunder the basic technical specifications in regards, to EUGENIUS platform are being illustrated. An elaborated documentation of these specifications, along with the specification needs for products to be in alignment with the platform will be further described during *"Task 1.3.4: Dissemination of products on EUGENIUS platform"*.

Table 5-1 - Acceptable data formats/sources for EUGENIUS online platform, Vector Data source/type.

Data Formats/Source	Description
Directory of spatial files (shapefiles)	Takes a directory of shapefiles and exposes it as a data store
H2	H2 Embedded Database
H2 (JNDI)	H2 Embedded Database (JNDI)
PostGIS	PostGIS Database
PostGIS (JNDI)	PostGIS Database (JNDI)
Properties	Allows access to Java Property files containing Feature information
Shapefile	ESRI (tm) Shapefiles (*.shp)
Web Feature Server (NG)	Provides access to the Features published a Web Feature Service, and the ability to perform transactions on the server (when supported / allowed)
<u>**Vector data specs**</u> • **Projection: All registered EPSG's plus custom projections** • **Size: No limitation** • **Metadata: INSPIRE compliant metadata/XML** <u>**Other Data Sources**</u> **WMS -> Remote Web Map Service**	

Table 5-2 - Acceptable data formats/sources for EUGENIUS online platform, Raster Data source/type.

Data Formats/Source	Description
ArcGrid	ARC/INFO ASCII GRID Coverage Format
GRIB	GRIB store plugin
GeoTIFF	Tagged Image File Format with Geographic information
Gtopo30	Gtopo30 Coverage Format

<table>
<tr><td>ImageMosaic</td><td>Image mosaicking plugin (The ImageMosaic data store allows the creation of a mosaic from a number of georeferenced rasters)</td></tr>
<tr><td>NetCDF</td><td>NetCDF store plugin</td></tr>
<tr><td>WorldImage</td><td>A raster file accompanied by a spatial data file</td></tr>
<tr><td colspan="2"><u>Raster data specs</u>
• Projection: All registered EPSG's plus custom projections
• Size: Only for .tiff datasets, up to 2gb size
• Metadata: INSPIRE compliant metadata/XML
<u>Other Data Sources</u>
WMS -> Remote Web Map Service</td></tr>
</table>

The first level of compatibility check in regards to the alignment of "Space for Shore" products' format with EUGENIUS platform, led to the fact that in most cases -if not in all-, the commonly used formats are tiff-GeoTiff (raster) and shapefiles (vector). Nevertheless, a second level of compatibility check will be performed that will take into consideration an extensive list of parameters beyond the "typical" file formatting (e.g. coordination systems, file capacity/volume, etc.). In any case during this task all possible restrictions in aspect of formats, file sizing, etc. will be tackled in as per indicator/algorithm.

6 CONCLUSION AND OUTLOOK

This document provides an overview of all algorithms available for producing indicators and finally the services to the users. The mapping of the algorithms to the user requirements provide a good assessment on which algorithms will be used for which coastal type and POC test site. It also gives the overall picture of the possible combinations of algorithm and EO data type (HR vs VHR) that can be used to address coastal erosion on the short-term (event to annual timescales) with a maximal accuracy or on the long term (interannual to decadal scales) usually coming with a poorer accuracy.

The algorithms differ in their level of maturity and while some are already mature, well validated and applied to many different locations, others are on an experimental stage and will be further tested during the POC. For the latter category, validation results could only partly be provided, and the algorithms will be further tested during the POC. This document will be updated accordingly, providing further input for validation and application range of the single algorithms. This should allow us to identify which algorithm performs best for each couple indicator / POC site, if not already done. These conclusions could then be extended at a larger scale to other coastal European regions.

– End –